Influence of oxygen and water adsorption on the surface chemistry and contact forces of defect rich metal-oxide and -nitride surfaces

Dissertation

zur Erlangung des Grades

Doktor der Naturwissenschaften Dr. rer. nat.

vorgelegt von

M.Sc. Christian Kunze

geboren in Herford

Universität Paderborn

Fakultät für Naturwissenschaften

Department Chemie

Lehrstuhl für Technische und Makromolekulare Chemie

im Mai 2014

Erstgutachter:	Prof. Dr.-Ing. Guido Grundmeier
Zweitgutachter:	Prof. Jochen M. Schneider, Ph.D.
Tag der Einreichung:	28. Mai 2014
Tag der mündlichen Prüfung:	27. August 2014

Hiermit bestätige ich, Christian Kunze, dass ich die vorliegende Arbeit *„Influence of oxygen and water adsorption on the surface chemistry and contact forces of defect rich metal-oxide and -nitride surfaces“* persönlich und nur unter Verwendung der angegebenen Quellen und Hilfsmittel angefertigt habe, sowie zur Hilfeleistung herangezogene Personen und Institutionen vollständig genannt sind.

Christian Kunze

Paderborn, den 28.05.14

Danksagung

Diese Arbeit wäre ohne die Hilfe einer Vielzahl von Menschen nicht zustande gekommen.

Ich bedanke mich bei meinem Doktorvater Prof. Dr.-Ing. Guido Grundmeier für die Überlassung der interessanten und herausfordernden Aufgabenstellung, die mir die Mitarbeit in zwei Projekten der Deutschen Forschungsgemeinschaft ermöglichte und eine eigenverantwortliche Bearbeitung erlaubte. Er trug durch seine zahlreichen Vorschläge und Ideen maßgeblich zum Fortschritt der Arbeit und zur Interpretation der Ergebnisse bei und ermöglichtes es mir, meine Ergebnisse auf zahlreichen nationalen und internationalen Konferenzen vorzustellen.

Herrn Prof. Jochen Schneider, Ph.D. danke ich nicht nur für die Übernahme des Ko-Referats, sondern auch für seinen wissenschaftlichen Input und seine Begeisterung für die gemeinsame Arbeit der letzten Jahre.

Weiterhin gilt mein Dank allen Kollegen und Kolleginnen des Arbeitskreises Grundmeier, die mir bei allen Problemen und Fragen stets mit Rat und Tat zur Seite standen. Zu fast jedem fiele mir sicherlich hier eine kleine Anekdote aus den vergangenen Jahren ein, aber das würde diesen Rahmen sprengen. In guter Erinnerung geblieben ist mir meine erste Konferenz, die mich im Spätsommer 2010 nach Arcachon in Frankreich führte und ich mit Hendrik, Stefan, Özlem und Berkem in einem Ferienhaus mit besonderem Charme unterkam: „What happens in Arcachon, stays in Arcachon…“

Meinem Bürokollegen Boray danke ich nicht nur für unsere gemeinsamen Jahre am Schreibtisch und seine Unterstützung in sämtlichen wissenschaftlichen Fragen und Experimenten, sondern auch dafür, dass er stets mit einem neuen Nerd-Spielzeug oder Gadget zu erheitern wusste.

Vielen Dank Ignacio, dass du durch (fast) nichts aus der Ruhe zu bringen bist und immer dann eingesprungen bist, wenn es mal wieder knapp wurde…

Der „UHV-Crew“ (Boray, Ignacio, Markus und Berkem) danke ich für ihr Engagement an der PIA sowohl beim Schrauben als auch beim Messen, ohne sie wäre solch eine Maschine nicht zu betreiben. Besonderer Dank gilt auch Thomas, für die zahllosen Beschaffungen und das Managen der Infrastruktur; ohne ihn wäre es kaum möglich gewesen, die Geräte und Labore aufzubauen.

Ein großer Dank gilt allen Mitgliedern des SFB-TR 87, es war toll in diesem Projekt mitarbeiten zu dürfen. Hier sind vor allem Moritz, Ricardo und Sebastian zu nennen, die stets für Proben-Nachschub aus Aachen sorgten und somit aktiv an den hier vorgestellten

Publikationen mitwirkten. Besonders meinen ehemaligen Master-Studenten Christian und Stefan möchte ich für ihre Mitarbeit in diesem Projekt danken.

Meinem Kollegen Rolf aus der physikalischen Chemie danke ich für die entspannten Gespräche in der Mittagspause vor allem während der heißen Phase dieser Arbeit.

Jasmin danke ich für das finale Korrekturlesen dieser Arbeit.

Zu guter Letzt gilt mein größter Dank selbstverständlich meinen Eltern, die mich in den vergangenen Jahren in allen Belangen bedingungslos unterstützt haben und mir das Studium erst ermöglicht haben.

"Imagination is more important than knowledge.

For knowledge is limited [...]."

— Albert Einstein, 1929

Abstract

In this work interfacial interactions of *M*AlN(O) (with *M* = Ti, Cr) and TiO_2 with small adsorbate-molecules such as water, oxygen or carboxylic acids were studied. Here, especially the chemical surface composition of the substrates and its impact on physicochemical interactions, taking place at the surface or within the surface near near region, were of interest.

*M*AlN(O) phases deposited by means of high power pulsed magnetron sputtering (HPPMS) are of valuable interest as hard coatings for tool steels that are employed e.g. in polymer processing. The *M*AlN(O) materials investigated in this work showed a significant enrichment of oxygen in the surface near region due to an oxidation reaction with environmental atmosphere. As these reaction layers determine the interaction with the polymer, a deeper knowledge of the chemical composition of the surface near region is of crucial interest. All investigated *M*AlN(O) coatings exhibited an excess of anions in the surface near region that points to a metastable material phase that is stabilized by the formation of metal vacancy defects. Furthermore the impact of the HPPMS parameters during the deposition of the coatings was investigated. It could be shown that the tendency of surface oxidation of CrAlN can be decreased by a forced incorporation of nitrogen into the material by setting short HPPMS pulse-on-times, which is an approach towards tailored surface compositions of CrAlN.

The initial chemisorption of oxygen has been studied on TiAlN. Via experimental and simulation work, it could be shown, that the reaction is determined by the formation of titanium oxide species and not by aluminum oxide which would be favored for thermodynamic reasons.

To study the adsorbate formation and interaction with water and carboxylic acids, atmospherically prepared TiO_2 single crystalline surfaces were employed as a model system. The interaction of OH-terminated TiO_2 substrates with nonadecanoic acid as a model adsorbate is weak and determined by physical interactions only.

The adhesive interaction at TiO_2 – TiO_2 crystalline surfaces was investigated as a function of the surface defect density. The measured contact force correlates with the observed surface defect density and can be discussed based on the effective Hamaker constant resulting from the change in electronic structure of the surface near region of the TiO_2 substrate.

Zusammenfassung

In dieser Arbeit wurden Grenzflächen-Reaktionen von *M*AlN(O) (mit *M* = Ti, Cr) und TiO_2 mit kleinen Adsorbat-Molekülen wie Wasser, Sauerstoff oder Carbonsäuren untersucht. Hierbei waren besonders die chemische Oberflächenzusammensetzung und deren Einfluss auf physikochemische Wechselwirkungen an der Oberfläche oder innerhalb des oberflächennahen Bereichs von Interesse.

*M*AlN(O)-Phasen, die durch High Power Pulsed Magnetron Sputtering (HPPMS) abgeschieden werden, sind von besonderem Interesse als Hartstoffschichten für Werkzeugestähle, die beispielsweise in der Kunststoff-Verarbeitung eingesetzt werden. Die in dieser Arbeit untersuchten *M*AlN(O)-Materialien zeigten durch eine Oxidationsreaktion mit Umgebungsatmosphäre eine signifikante Anreicherung von Sauerstoff im oberflächennahen Bereich. Da diese Reaktionsschichten die Wechselwirkung mit dem Polymer bestimmen, ist ein tieferer Einblick in die chemische Zusammensetzung des oberflächennahen Bereichs von entscheidender Bedeutung. Alle untersuchten *M*AlN(O)-Schichten wiesen einen Anionen-Überschuss im oberflächennahen Bereich auf, was auf eine metastabile Phase hindeutet, die durch Metall-Leerstellen-Defekte stabilisiert wird. Des Weiteren wurde der Einfluss der HPPMS-Parameter während der Schichtabscheidung untersucht. Hier konnte gezeigt werden, dass durch die Wahl kurzer HPPMS-Pulszeiten die Tendenz zur Oberflächenoxidation von CrAlN durch eine forcierte Einlagerung von Stickstoff in das Material verringert werden kann, was einen Ansatz hin zu maßgeschneiderten Oberflächenzusammensetzungen von CrAlN darstellt.

Die initiale Chemisorption von Sauerstoff wurde auf TiAlN untersucht. Es konnte durch experimentelle und simulative Arbeiten gezeigt werden, dass die Reaktion durch die Bildung von Titanoxid und nicht durch Aluminiumoxid, das thermodynamisch begünstigt wäre, bestimmt wird.

Um die Bildung von Adsorbaten und die Wechselwirkung mit Wasser und organischen Säuren zu untersuchen, wurden atmosphärisch präparierte TiO_2-Einkristall-Oberflächen als ein Modellsystem eingesetzt. Die Wechselwirkung von OH-terminierten TiO_2 Substraten mit Nonadecansäure als ein Modelladsorbat ist gering und wird nur durch physikalische Wechselwirkungen bestimmt.

Die adhäsive Wechselwirkung an kristallinen TiO_2 – TiO_2 Grenzflächen wurde als Funktion der Oberflächen-Defektdichte untersucht. Die gemessene Kontaktkraft korreliert mit der beobachteten Defektdichte und kann basierend auf der effektiven Hamaker-Konstante, die aus der Änderung der elektronischen Struktur im oberflächennahen Bereich des TiO_2-Substrates resultiert, diskutiert werden.

Table of Contents

Preamble

This dissertation is organized as a thesis by publication and divided into three main parts. In the first chapter the introduction gives an overview of the motivation and the scientific approach of this work. This is followed by a review of relevant literature and the current state of research. Advanced experimental approaches that were employed within this work are highlighted in the following chapter. In the third chapter six scientifically relevant publications, which were prepared based on the scientific work covered by this thesis, are presented. For each publication the author's contributions are specified. In the last chapter the most important results of this work are summarized, followed by an overall-conclusion and a scientific outlook.

The work presented here was performed in the background of two research projects funded by the *Deutsche Forschungsgemeinschaft* (DFG):

(i) SFB-TR 87 *Gepulste Hochleistungsplasmen zur Synthese nanostrukturierter Funktionsschichten; Teilprojekt "Verständnis der molekularen Adhäsion an der Grenzfläche zwischen polymerer Schmelze und Plasmaschicht"*

(ii) SPP 1486 *Partikel im Kontakt; Teilprojekt „Molekulare UHV-AFM und FTIR Untersuchungen von Adsorbat belegten TiO_2-Mikropartikel-Oberflächen"*

Chapter 1

1 Introduction

1.1 Motivation and scientific approach

The aim of this work is to investigate the interaction of small molecules, such as water and oxygen, with metal-oxide and -nitride surfaces. Especially the surface chemistry and correlated surface phenomena, such as adhesion and the formation of defects within the surface near region, are of important interest in this context. An understanding of these

phenomena not only gives an insight into processes on an atomistic scale, but is also relevant for technical applications.

The field of surface science is a wide spread, interdisciplinary research topic covering chemistry, physics and also engineering. A large variety of technical applications and processes, such as catalysis [1], corrosion [2], energy conversion [3], adhesives [4], semiconductors [5], medical applications [6], data storage [7] and many more, are driven by interfacial processes. Only a few of these processes and correlated structures are yet well understood, although they are present in our everyday life.

Within this work two demonstrators with relevance for technical applications were investigated: (i) Metal (oxy)nitrides with the composition *M*AlN(O) with *M* = Ti, Cr and (ii) single crystalline TiO_2 surfaces.

The here presented approach focuses on the investigation of interfacial processes on the earlier mentioned substrates. Therefore, ultrahigh vacuum (UHV) as well as environmental techniques were employed, which allows for bridging between an understanding of the observed processes and reactions on a fundamental level – as obtained from UHV experiments – towards a macroscopic understanding at environmental conditions. Furthermore complementary *ab initio* molecular dynamics (MD) simulations were performed within a cooperation in the workgroup of Prof. Jochen M. Schneider, Chair for *Materials Chemistry (MCh)* at the RWTH Aachen University.

The *M*AlN(O) samples investigated within this work were deposited in a physical vapor deposition (PVD) process by means of high power pulsed magnetron sputtering (HPPMS) within a cooperation at the *MCh* and at the workgroup of Prof. Dr. Kirsten Bobzin, *Surface Engineering Institute (IOT)*, RWTH Aachen University. Especially the interaction of oxygen with *M*AlN(O) surfaces has been studied within this work. For TiAlN the initial chemisorption of oxygen was studied by means of computational simulations at the *MCh* and correlated to experimental results presented within this work.

Single crystalline rutile TiO_2 surfaces, prepared under ambient conditions, were employed as a model system for more complex TiO_2 surfaces (e.g. TiO_2 particles) to study interactions at TiO_2 surfaces on a fundamental level. Within the here presented approach, surface adsorbates were simulated by the adsorption of nonadecanoic acid (NDCA) onto TiO_2(100) surfaces, which allows a fundamental understanding of particle-wall interactions under ambient conditions in the presence of organic adsorbates.

Consequently, this approach was followed by the investigation of contact forces by means of atomic force microscopy (AFM) under UHV conditions. The contact forces between a TiO_2 coated conical AFM tip and a rutile TiO_2(110) surface were investigated under UHV-

conditions to simulate a particle – wall contact. The analyzed interactions under different experimental conditions enabled the correlation of the observed adhesion forces and the chemical composition of the TiO_2 surface as reflected by a variation of the defect density, the presence of water and the role of organic surface layers.

1.2 Metal nitride and oxide materials

1.2.1 *M*AlN(O) phases for hard coatings

Hard coatings of the chemical composition *M*AlN(O) with *M* = Ti, Cr were investigated within this work, as these materials are a promising approach to decrease wear and friction in polymer processing such as extrusion or injection molding. All investigated coatings were deposited at the RWTH Aachen University using an industrial coating unit CC-800/9 (CemeCon AG, Germany) at the institute for *Materials Chemistry (MCh)* in case of TiAlN(O) and at the *Surface Engineering Institute (IOT)* in case of CrAlN.

TiAlN tool steel coatings are widely used as protective coatings for tools within mechanical processing, such as cutting or forming, due to their hardness as they offer a good wear and oxidation resistance [8, 9]. Recent theoretical studies showed that the work of separation between polypropylene and ideal $M_{0.5}Al_{0.5}N$ could be lowered by additional incorporation of oxygen leading to the oxynitride $M_{0.5}Al_{0.5}N_xO_y$ phase [10]. It is also reported that TiAlNO coatings show an increased performance in contact with molten JIS ADC 12 aluminum alloy [11] and for the processing of transparent polymers [12]. In the injection molding process of polyolefins, the number of low quality products that showed an inhomogeneous surface quality could be significantly reduced by the deposition of CrAlNO coatings on the extruder unit [13].

Often the deposition of such coatings is a non-equilibrium process that is governed by an interplay of thermodynamics and kinetics [14]. A common synthesis method is a plasma enhanced physical vapour deposition (PVD) process by means of high power pulsed magnetron sputtering (HPPMS) which is schematically presented in Figure 1.1. A detailed review of the HPPMS technology is given by Sarakinos et al. [15] and Lundin et al. [16]. Due to high-energy pulses a plasma density can be achieved which is higher by three orders of magnitude in comparison to conventional direct current (DC-MS) sputtering [17], leading to highly ionized plasmas with an increased ion/atom ratio in comparison to DC-MS [18, 19]. For CrAlN hard coatings deposited by HPPMS improved mechanical properties for

aluminium contents below 30 at.-% could be shown. An increased hardness of 27 GPa for coatings deposited by HPPMS in comparison to 22 GPa for coatings deposited in the DC-MS process was found [20]. Furthermore, a significantly different phase texturing that preferentially shows a (200) orientation in case of HPPMS and (111) for DC-MS deposited coatings has been observed [21].

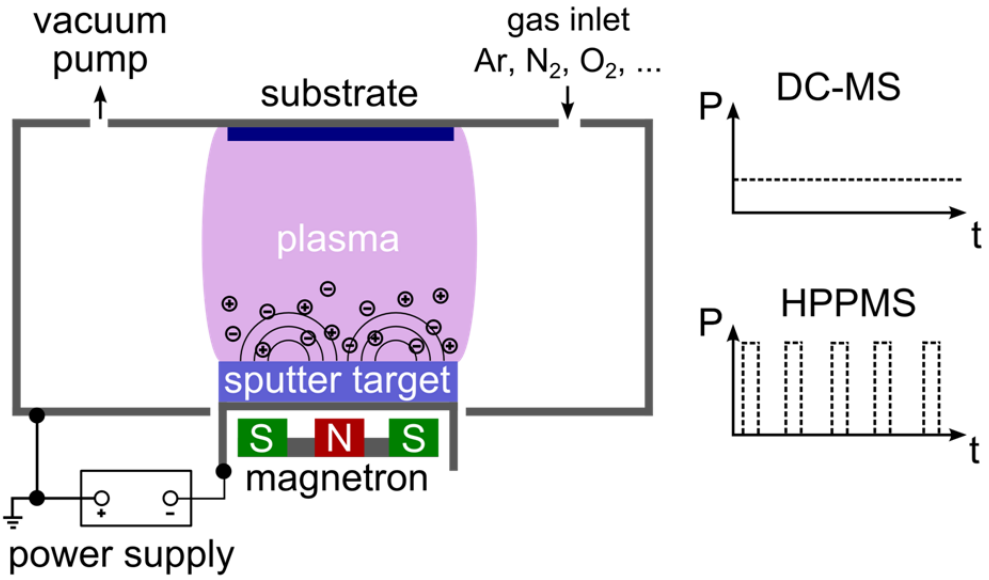

Figure 1.1: Schematics of the plasma enhanced PVD process including the qualitative power/time curves for DC-MS and HPPMS processes.

The surface near region of CrAlN and TiAlN is enriched with oxygen after the deposition process which is most likely due to a reaction with atmospheric oxygen upon venting the deposition chamber [22-24]. As the characteristics of the surface near region determine the interaction of the hard coating with the polymer melt, an exact knowledge of the chemical composition of the surface near region is of crucial interest. However, the exact mechanism of oxygen incorporation is still under discussion as referred in chapter 1.3.3.

In order to predict and optimize the interaction between the polymer and the hard coating, an exact knowledge of the oxide formation within the surface near region of *M*AlN(O) materials is of high importance, especially when a targeted surface composition is desired for tailored materials that show optimized properties in terms of their application, e.g. a minimized interaction with the polymer in technical applications.

1.2.2 Surface chemistry of titanium dioxide

Due to its interesting properties titanium dioxide (TiO_2) has been extensively studied within the last decades. Titanium dioxide offers an interesting potential for photocatalytic applications [25], as biomaterials [26] or in dye sensitized solar cells [27] which is mostly attributed to its optical properties offering a high refractive index and its electrical properties of semiconducting characteristics.

Three modifications of TiO_2 are naturally occurring: Rutile (as shown in Figure 1.2) and anatase show a tetragonal crystal structure, while brookite exhibits an orthorhombic lattice. The following Table 1.1 gives an overview on the optical and electrical properties of titanium dioxide. Based on its optical characteristics, a main application of TiO_2 in the modifications of rutile or anatase is as a white pigment [28], or as a compound in food and cosmetics [29].

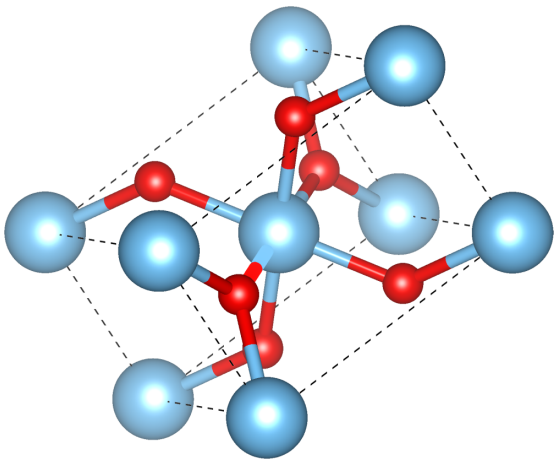

Figure 1.2: Bulk structure unit cell of the rutile modification of TiO_2, consisting of O anions (red) and Ti cations (blue). The lattice parameters are a=b=4.584 Å, and c=2.953 Å [30].

Table 1.1: Optical and electrical properties of TiO_2

modification	refractive index at 589 nm [31]	band gap [32]
rutile	n = 2.90	3.02 eV
anatase	n = 2.48	3.23 eV
brookite	n = 2.59	3.14 eV

The surface structure of TiO_2 has been mostly studied under UHV conditions, e.g. by Diebold et al. [30, 33] and Henderson et al. [34], which is reflected by extensive studies

mainly of the TiO_2(110) and TiO_2(100) surface orientations and their most common (1×1) and (1×2) reconstructions. Therefore, at this point only very few examples shall be discussed. Bennett et al studied the formation of the (1×2) reconstruction on TiO_2(110) at elevated temperatures by means of scanning tunneling microscopy (STM) [35]. They found two differently ordered surface reconstructions depending on the stoichiometry of the bulk crystal. On stoichiometric surfaces the (1×2) reconstruction goes along with the formation of a Ti_2O_3 type surface termination. For heavily reduced crystals a cross-linked (1×2) reconstruction is formed in the type of TiO_2.

The interaction of small molecules such as water, alcohols or organic acids at the TiO_2 surface has been intensively studied under UHV conditions within the last years [36-39]. In contrast, only few authors studied the adsorption of larger molecules on TiO_2 surfaces under ambient conditions [40, 41].

Henderson reported a different behavior of water adsorption for different TiO_2 surface orientations, which is discussed based on temperature-programmed desorption studies (TPD) [34]. They observed monolayer desorption states for the (100) surface orientation at 205 K, 250 K, and 305 K, while only one desorption state was observed for the (110) surface at 270 K. This behavior of water ad- and desorption is discussed based on the different mechanisms of water dissociation on the (100) and the (110) surface involving different surface sites for hydroxide formation of terminal and bridging surface hydroxyl groups as shown in Figure 1.3

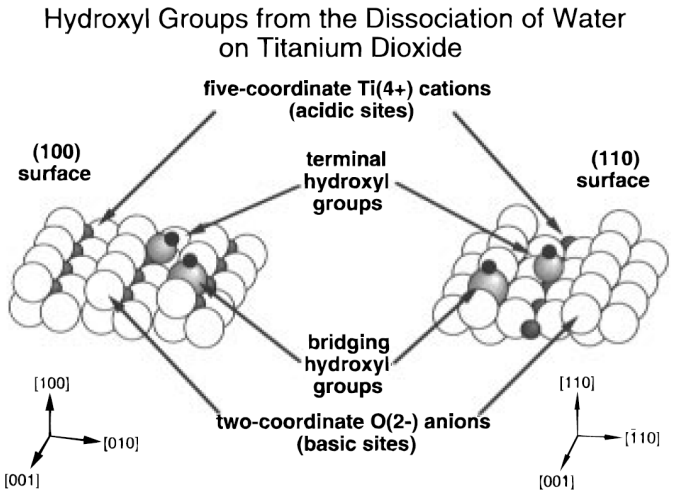

Figure 1.3: Schematics of terminal and bridging hydroxyl groups on TiO_2(110) and TiO_2(100) surfaces. Figure taken from [34].

TiO_2 single crystalline substrates that were prepared under ambient conditions, can be employed as a model system to bridge towards more complex TiO_2 particle interfaces, which are much more complicated to understand regarding their morphology and chemical composition. Nakamura et al. and Yamamoto et al. showed the preparation of well-defined, stepped TiO_2 single crystalline surfaces via a procedure of wet chemical etching followed by an annealing step in air [42-44], which was slightly modified in this work [45].

Considering relevant processes in technical applications such as fluidization, agglomeration and sintering [46], adhesion forces between micro- and nanoparticles play an important role. Such processes are utilized in a wide range of tasks, including the production of pharmaceutical powders, paints and solar cells [47, 48]. As the interactions between small particles are mostly driven by van der Waals forces, hydrogen bonding and capillary forces, the physical and chemical structure of the particle surface is of crucial importance. Hence, the well-defined surface composition with atomically flat terraces of TiO_2 single crystalline substrates is most suitable to study those interactions on a fundamental level. As mentioned above, capillarity forces also have to be considered when discussing force interactions between particles under ambient conditions [49, 50]. Farshchi-Tabrizi et al. investigated capillarity forces between particle modified AFM tips and surfaces of different roughness as a function of the relative humidity and reported that an influence on the adhesion force was only detectable for hydrophilic surfaces [51]. Considering photocatalytic effects, Wang et al. studied the influence of UV light irradiation on the wetting properties of TiO_2 single crystalline surfaces and observed a reversible surface wettability based on a photo induced transition between Ti^{4+} and Ti^{3+} [52].

For surface interactions and contact forces under ambient conditions, native surface contaminations, which originate from the atmosphere, have to be taken into account as they also have a significant impact on the surface chemistry. Such adsorbates mainly consist of water, carbon dioxide and low weight (hydro)carbon species, such as carboxylic acids, esters and ethers. These side effects of uncontrolled adsorbate formation can be avoided by very controlled experimental conditions such as UHV-based setups. Up to now only few AFM contact force experiments under UHV conditions have been reported in the literature, e.g. by Tadepalli et al., who studied the bond formation at Cu – Cu interfaces [53] and Meine et al., who investigated the influence of the surface roughness on the interaction force based on the JKR (Johnson, Kendall and Roberts) contact model [54].

When discussing force interactions on a nanoscopic level, as measured by AFM, specific interactions directly located in the contact area as well as the sub-surface composition and electronic properties have to be considered [55]. The presence of local

dipoles and gradients in electron density of the interacting materials are crucial for contact behavior of the TiO_2 – TiO_2 system, as they contribute to the van der Waals interactions [56, 57]. Furthermore, interfacial forces of oxides can be influenced by the adsorption of self-assembled monolayers such as organophosphonic acids which form 2-dimensional crystalline aliphatic films [58]. This approach offers to create a model system based on a known adsorbate chemistry as already discussed above.

1.3 Chemisorption of oxygen and oxide film growth

Within this section the basic mechanisms leading to oxide film growth shall be reviewed. The word "oxide film" is found in literature to mean layers of oxide thickness from a single monolayer to several hundred micrometers. Here the formation of thin oxide films up to a few ten nanometers will be discussed.

Generally, the formation of an oxide film is preceded by the adsorption of small molecules from the gas phase such as oxygen or water, followed by their dissociation, ionization and surface diffusion. These processes lead to the formation of oxide nuclei and finally the lateral growth of the nuclei until a complete layer of oxide is formed. Since the exact mechanisms of oxygen chemisorption are complex and vary for each material, the mechanism of oxygen chemisorption on titanium, chromium and aluminum shall be discussed briefly here, as examples. However, it is accepted that for most surfaces the initial physisorption of small molecules such as oxygen is followed by the dissociation of the molecule as the first step of the chemisorption process [59-62].

1.3.1 Oxygen chemisorption on reactive metals: Ti, Cr, Al

1.3.1.1 Titanium

The chemisorption of oxygen on Ti(0001) has been investigated by Jonker et al. by means of appearance potential spectroscopy (APS), Auger electron spectroscopy (AES), low-energy electron diffraction (LEED), and work-function measurements obtained by the field-emission retarding potential technique [63]. They found an impact of adsorbed oxygen on the local density of states which increases the work function from 4.58 eV (clean surface) to 5.3 eV (oxygen saturated surface). On the bare Ti(0001) surface a strong band of states just above the Fermi level is located close to the surface which is suppressed upon exposure to oxygen. The authors identified two states of oxygen chemisorption: (i) A tightly bound "α state" for a low oxygen coverage of 0.25 monolayers (ML) that can be identified by a well

ordered $p(2\times2)$ LEED pattern, and (ii) a "β state" that is characterized by a disordered structure and an increased work function.

Complementary *ab initio* studies on the oxygen adsorption on the Ti(0001) surface were published by Liu et al. [59]. They could show that the top-surface face centered cubic Ti(0001) sites are most favorable for the adsorption of oxygen up to a coverage of 0.25 ML. For a system with a higher coverage of 0.50 ML additional occupation of the octahedral sites between the second and the third Ti layer leads to the most stable configuration. At even higher coverage of 1.0 ML the remaining octahedral sites are also occupied, which leads to a further stabilization and a change in work function and density of states as discussed above.

1.3.1.2 Chromium

The adsorption of oxygen on Cr(110) surfaces was studied by Shinn et al. [64]. According to their work, dissociative chemisorption leads to an ordered p(4×2) oxygen overlayer, which gives a model with atomic oxygen located in the two-fold symmetric hollow sites as presented in Figure 1.4.

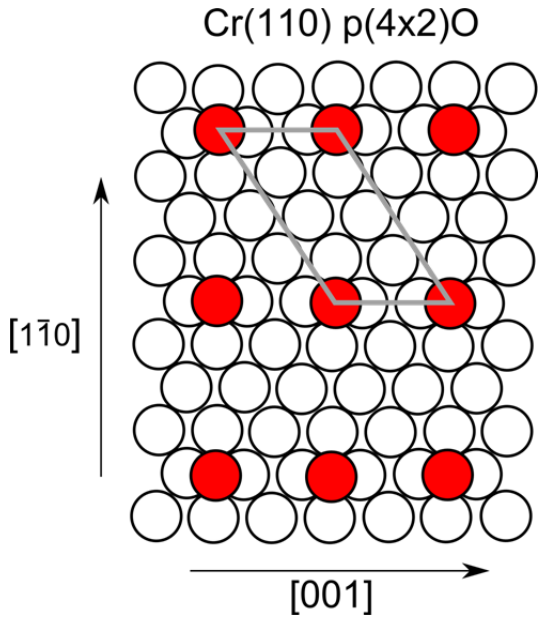

Figure 1.4: Model of the p(4x2)O overlayer on Cr(110). The ideal coverage corresponds to 1/8 monolayer. Red circles represent O atoms, the parallelogram shows the c(4x2) lattice. Schematics according to [64].

A detailed work of Sakisaka et al. [65] studied the oxygen chemisorption on Cr(110) and its impact on the band structure and work function. As investigated by electron loss spectroscopy (ELS) at low oxygen exposures up to 2 L (1 L = 1 Torr · 1 µs) the interaction is

dominated by the O 2p → Cr 3d orbital transition which is accompanied by an increase in work function of +0.19 eV. In the region of 2 – 6 L the electronic interaction has to be described by various additional transitions such as d → d ligand field, O 2p → Cr 4s, Cr 3d → 4p and Cr 3d → 4f transitions. Above 10 L the oxidized surface is dominated by Cr_2O_3. In summary they propose an oxidation reaction in four stages: (i) dissociative chemisorption below a coverage of 2 L, (ii) incorporation of oxygen adatoms into the Cr selvedge between 2 – 6 L, (iii) between 6 – 15 L rapid oxidation leading to the formation of a thin Cr_2O_3 film and finally (iv) slow thickening of Cr_2O_3.

Foord et al. compared the behavior of oxygen chemisorption on the Cr(100) and the Cr(110) orientation [66]: At temperatures of 300 K on both surface orientations metastable oxygen overlayers, that were slowly incorporated into the underlying metal, were observed. At higher oxygen exposures of 10 – 100 L the formation of Cr_2O_3 films takes place leading to an oxide film thickness of 0.4 to 1.3 nm after dosing 100 L. On the Cr(100) orientation the oxide formed a well ordered *c*(2×2) LEED structure whereas Cr(110) exhibited oxygen-induced faceting.

1.3.1.3 Aluminum

Gartland studied the chemisorption of oxygen on Al(100) and Al(111) by Auger electron spectroscopy (AES) and work function measurements [67]. He reported significantly different results for the two surface orientations. The sticking coefficient of the Al(111) surface orientation drops significantly with the surface coverage, along with an slightly increasing work function by 0.1 eV at 200 L. In contrast, the sticking coefficient on the Al(100) surface orientation exhibits a maximum, whereas the work function decreases almost linearly with coverage up to a total decrease of 0.5 – 0.8 eV at 200 L. A different adsorption mechanism could be observed for the Al(111) and the Al(100) orientation. While adsorbing randomly on the (111) surface, the oxygen atoms form clustered islands of thin oxide on the (100) surface which is discussed based on a different surface mobility of the oxygen atoms. This finding has been confirmed by Brune et al. who could show via scanning tunneling microscopy (STM), that oxygen adatoms are practically immobile on the Al(111) surface at 300 K and low coverage [68].

Flodstöm et al. observed an ordered chemisorption of oxygen on Al(111) in the initial formation of surface oxide and suggested a threefold, centered bonding site [69]. At high oxygen exposure or high temperature, this phase transforms irreversibly to a bulklike aluminum oxide film. The interaction is discussed based on the resonance of the O 2p orbital

with the valence band of the Al surface which leads to a decrease in the distance between the oxygen adatom and the metal surface followed by Al–O bond formation which goes along with a surface reconstruction that allows the formation of Al_2O_3.

1.3.2 Principal mechanisms of oxide film growth a high and low temperature

Followed by the initial oxygen chemisorption as discussed above, the thickness of the oxide films grows, which can be described up to a thickness of less than 1 µm by the theory of Cabrera and Mott [70], that has been reviewed by Atkinson [71] amongst others. For such thin films the concept of electrical neutrality – leading to an equilibrium growth process – is unreliable, especially for a thickness of less than 20 nm in which case the Nernst-Einstein relation is no longer applicable. The Nernst-Einstein relation (1) can be understood in terms of the Brownian motion and gives a relation between the diffusion coefficient D and the mobility μ of the charged particles:

$$D = \frac{\mu k_B T}{q} \tag{1}$$

D: diffusion coefficient in $\frac{m^2}{s}$

k_B: Boltzmann constant in $\frac{J}{K}$

T: temperature in K

q: electrical charge in $A \cdot s$

μ: electrical mobility in $\frac{m^2}{V \cdot s}$

Theories of thin film growth rather have to consider ion jumps in the presence of large electric fields and the possibility of large space charges. Cabrera and Mott assumed that the electrons can freely pass from the metal to ionize the adsorbed oxygen species so that the Fermi level is equal for the metal and the adsorbed layer. Thus a uniform electric field is created by the O^{2-} ions and the positive interface charge of the metal. Hence, this electric field created by the electron transfer drives the transport of ions across the oxide film and causes it to thicken. The easiest surface reaction regarding the dissociation of oxygen can be written as:

$$½\ O_{2\,(gas)} + 2\ e_{\,(metal)} \rightarrow O^{2-}{}_{(surface)} \tag{2}$$

Reaction (2) is assumed to be in equilibrium. Hence, we can write the equilibrium constant *K* as a function of the chemical activities *a*:

$$K = \frac{a(O^{2-})}{a(O_2)^{1/2}\, a(e)^2} \tag{3}$$

Where *K* is related to the change in standard free-energy ΔG^0 of equation (3) and can be described by the Arrhenius equation:

$$K = \exp\left(\frac{-\Delta G^0}{k_B T}\right) \tag{4}$$

If the surface coverage of excess O^{2-} ions is low, it can be assumed that $a(O^{2-}) = n_0 / N_S$ where n_0 is the number of excess O^{2-} ions and N_S is the number of O^{2-} ions per unit area of the surface. The activity of an electron with respect to the Fermi level is equal to $\exp(-e\Delta\varphi / k_B T)$, where the difference in potential $\Delta\varphi$ is a positive value. Combining this with equations (3) and (4) gives:

$$n_0 = N_S a(O_2)^{1/2} \exp\left(-\frac{\Delta G^0 + 2e\Delta\varphi}{k_B T}\right) \tag{5}$$

The surface charges can be regarded as a plate capacitor which leads to another expression for n_0, where *X* is the thickness of the oxide film:

$$n_0 = \frac{\varepsilon\varepsilon_0 \Delta\varphi}{2eX} \tag{6}$$

Solving equations (5) and (6) for $\Delta\varphi$ gives:

$$\frac{2e\Delta\varphi}{k_B T} + \ln\left(\frac{2e\Delta\varphi}{k_B T}\right) = -\frac{\Delta G^0}{k_B T} + \ln\left(\frac{4e^2 N_s a(O_2)^{1/2} X}{k_B T \varepsilon\varepsilon_0}\right) \tag{7}$$

As usually $e\Delta\varphi / k_B T >> 1$, the second term on the left side of equation (7) can be neglected which leads to:

$$\Delta\varphi = -\frac{\Delta G^0}{2e} + \frac{k_B T}{2e}\ln\left(\frac{4e^2 N_s a(O_2)^{1/2} X}{k_B T \varepsilon\varepsilon_0}\right) \tag{8}$$

Thus according to equation (8) $\Delta\varphi$ is mainly related to the change in free energy of the reaction but also dependent on *T* and, more weakly, on $a(O_2)$ and *X*.

To calculate the oxidation rate, it has been assumed that the rate controlling step is either (i) the formation of a defect in the oxide film at the oxide/metal interface as presented in Figure 1.5 a) or (ii) the formation of a defect at the oxide/gas interface shown in Figure 1.5 b).

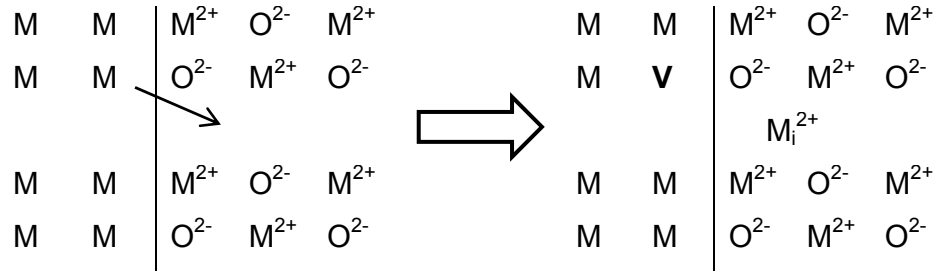

Figure 1.5 a) Formation of a defect at the metal/oxide interface. The symbol *V* is correlated to a vacancy, M_i^{2+} stands for an interstitial metal ion (schematics according to [71]).

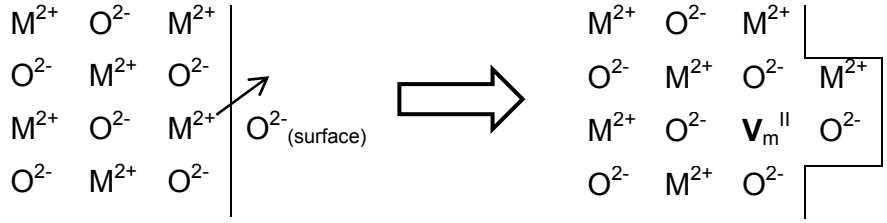

Figure 1.5 b) Formation of a defect at the oxide/gas interface (schematics according to [71]).

According to Figure 1.5 a) for the chemical reaction in case of (i) we can write the following equation:

$$M_{(metal)} \rightarrow M_i^{2+}{}_{(oxide)} + 2e_{(metal)} + V_{(metal)} \tag{9}$$

Assuming that the activation energy *W* for the jump from the metal into the oxide film is larger than the activation energy for its subsequent jumps within the oxide film, ΔH_m means that $W - \Delta H_m$ is the energy of the incorporation of the defect. Under influence of an electric field the activation energies are reduced by $qa\Delta\varphi / 2X$. The interface is considered

to be far from equilibrium because the electric field does not allow the reaction to take place in the reverse direction. Within this so called "high-field limit" the growth rate is given by

$$\frac{dX}{dt} = a\nu \exp\left(-\frac{W}{k_B T}\right)\exp\left(\frac{qa\Delta\varphi}{2k_B TX}\right) \tag{10}$$

where ν is the vibrational frequency of the atoms in the interface. Writing $X_1 = qa\Delta\varphi / 2k_B T$ and $D_i = a^2\nu \exp(-W / k_B T)$ equation (10) can be simplified to:

$$\frac{dX}{dt} = \frac{D_i}{a}\exp\left(\frac{X_1}{X}\right) \tag{11}$$

According to equation (11) the oxidation rate decreases exponentially with increasing film thickness. When $X << X_1$ (X_1 can be considered as the limit for which the assumptions made above are valid) equation (11) can be integrated to give the inverse logarithmic law

$$\frac{X_1}{X} = -\ln\left(\frac{D_i X_1 t}{a X_L{}^2}\right) \tag{12}$$

where X_L is the limiting thickness above which further growth can be neglected. According to the criterion of Cabrera and Mott who give a negligible rate of 10^{-15} ms^{-1}, X_L is given by:

$$X_L = X_1 / \left(\frac{W}{k_B T} - 39\right) \tag{13}$$

For the chemical reaction in case (ii) (defect formation at the oxide/gas interface according to Figure 1.5 b) we can write the equation:

$$M^{2+}_{(oxide)} + O^{2-}_{(surface)} \rightarrow V_m^{II} + MO \tag{14}$$

Basically the calculation of the growth rate is analog to the considerations presented above with the difference that only those metal ions that can reach a surface O^{2-} directly from the metal/oxide interface can undergo reaction (14). Thus the number of surface O^{2-} ions will depend on the geometrical arrangement of the surrounding atoms which will give

an average coordination number of 5 for a surface ion, which means that the growth rate depends on the concentration of surface O^{2-} ions. This results in an equation analog to (10):

$$\frac{dX}{dt} = 5a\nu\frac{n_0}{N_S}\exp\left(-\frac{W}{k_BT}\right)\exp\left(\frac{qa\Delta\varphi}{2k_BTX}\right) \tag{15}$$

With equation (6) for n_0 the growth rate is analog to equation (11)

$$\frac{dX}{dt} = \left(\frac{5\varepsilon\varepsilon_0\Delta\varphi}{2eN_SX}\right)\frac{D_i}{a}\exp\left(\frac{X_1}{X}\right) \tag{16}$$

giving a slightly different kinetics compared to equation (11) because of the appearance of X in the denominator which leads to a smaller limiting thickness X_L than predicted for the defect formation at the oxide/metal interface. Analog to (13) the limiting thickness is:

$$X_L = X_1 / \left(\frac{W}{k_BT} - 39 + \ln X_L\right) \tag{17}$$

A slight modification to the model discussed above has to be made for low-temperature oxidation (LTO). LTO defines an oxidation reaction that takes place at temperatures near 25 °C or below in which an oxide layer forms with a very small or even zero activation energy. Due to the assumptions made there, the Cabrera-Mott theory as shown above has to be modified for some instances as discussed by Fehlner and Mott [72].

An important difference is the fact that LTO is controlled by the morphology of the oxide itself where, for example, the migration of anions through the oxide film also has to be considered in contrast to solely cation movement as described by Cabrera and Mott. The initial chemisorption is followed by a fast oxidation process in which anions and cations interchange positions. This happens when the energy, due to the electrostatic image force of an oxygen ion, is greater than the binding energy that holds the ion in place. Vice versa a stable film is formed when the binding energy is larger than the image force, which leads to the formation of oxygen ions on the surface that build up a potential across the film. This potential provides the driving force for the ongoing reaction of a slow, logarithmic oxide growth according to Cabrera-Mott. Here the rate of the ion transfer is limiting as described by the Cabrera-Mott mechanism for the cation movement. In contrast, for anion movement

the assumption that the structure changes with film thickness as proposed by Eley and Wilkinson [73] is necessary. If the oxide film re-orders to form microcrystals, the logarithmic reaction rate can increase as in networks ions can easily migrate along grain boundaries to form domains. Furthermore the logarithmic growth rate can be increased by the presence of water vapor if the water induces dangling bonds into the oxide network structure.

To summarize, the process of low temperature oxidation can be divided into three parts that smoothly transform into the following:

(i) Fast incorporation of oxygen into the metal surface by place exchange;

(ii) continued, slow logarithmic growth of the oxide film caused by the electric field built up across the oxide and

(iii) accelerated logarithmic growth that results from the re-ordering of the film with crystallization and domain growth.

1.3.3 Oxygen chemisorption on metal nitride surfaces

The TiAlN and CrAlN phases, which are discussed within this work, exhibit a face centered cubic (fcc) NaCl structure (as presented in Figure 1.6) with a transition to an amorphous phase for TiAlNO at high contents of oxygen [23].

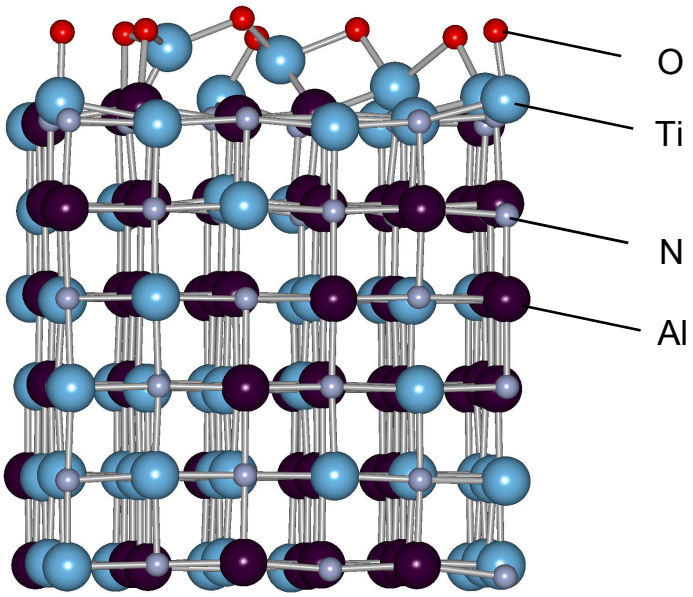

Figure 1.6: Structure of $Ti_{0.5}Al_{0.5}N(001)$ interacting with four oxygen molecules. In the bulk structure Ti and Al are statistically distributed in the fcc lattice on the cation positions. The chemisorption of oxygen goes along with the displacement of Ti atoms from the surface plane. Figure taken from [74].

Shaha et al. performed *ab inito* molecular dymanics simulations and proposed a mechanism oxygen incorporation into the bulk structure of $V_{0.5}Al_{0.5}N_{1-x}O_x$ by replacement of nitrogen lattice positions by oxygen along with the formation metal vacancies [75]; where the mechanism of oxygen incorporation of TiAlN phases is a topic of ongoing research.

Music et al. studied the interaction of the $Ti_{0.5}Al_{0.5}N(001)$ surface with small gas phase molecules such as O_2, H_2O and CO_2 by means of *ab inito* molecular dynamics (MD) simulations [76]. They could show that the dissociative adsorption of O_2 occurs at Ti surface sites and suggested that an increased Ti–O bond strength in comparison to Al–O is the electronic origin of the early stages of TiO_2 formation on $Ti_{0.5}Al_{0.5}N(001)$. They also observed the displacement of Ti from the $Ti_{0.5}Al_{0.5}N(001)/O$ interface layer which generates vacancies and enables the mobility at the interface.

However, the exact mechanism of oxygen adsorption and following dissociation on TiAlN has not been investigated in detail, yet. The initial oxidation stages TiN(100) were investigated by means of *ab initio* MD by Zimmermann et al. in [77]. As presented in Figure 1.7, they propose a mechanism of dissociative oxygen adsorption in which the oxygen

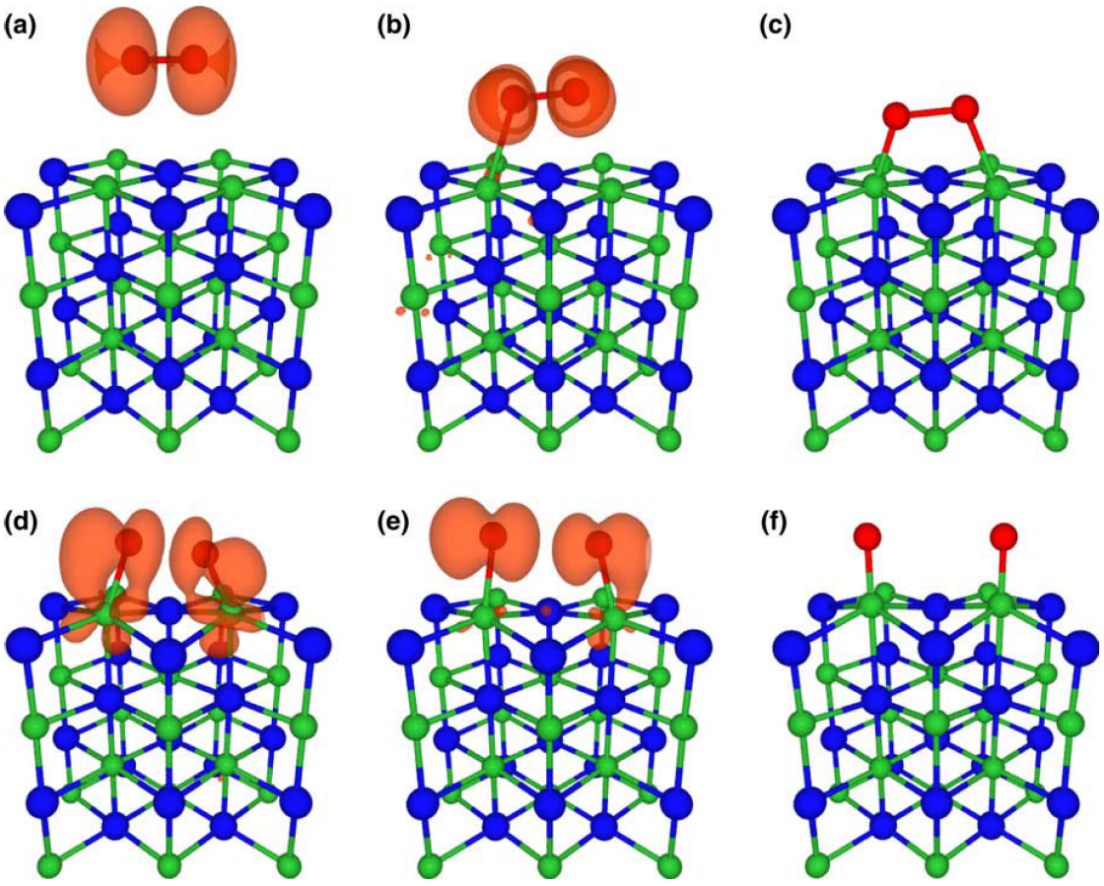

Figure 1.7: Snapshots from a MD simulation of the dissociative adsorption of an oxygen molecule on the TiN(100) surface. Green: Ti; blue: N. (a) initial configuration; (b) after 94 fs; (c) after 109 fs; (d) after 131 fs; (e) after 145 fs; (f) final configuration. Figure taken from [78].

molecule hits the surface and initially binds to a Ti atom, as described more detailed in [78]. Subsequently, the oxygen molecule moves to a bridge position connecting two surface Ti atoms followed by the dissociation step in a so called “hot atom” mechanism [79]. The electron donation occurs from the metal atoms into the antibonding orbitals of O_2. However, at this point it is not clear whether this mechanism of oxygen adsorption can be directly transferred to Tail. In both cases at least the reaction of oxygen with titanium is the dominating process.

For technical processes further oxidation processes especially at elevated temperatures are of high relevance. McIntyre et al. studied the oxidation of TiAlN at elevated temperatures up to 1173 K in pure oxygen at ambient pressure and identified aluminum and oxygen as the mobile species leading to the formation of an about 100 nm thick aluminum oxide layer with an underlying titanium oxide layer of comparable thickness [9]. Tempez et at. studied the oxidation of TiAlN at temperatures of 460 °C and an oxygen pressure of 10^{-6} Torr [79]. By means of mass spectrometry and X-ray photoelectron spectroscopy (XPS) they could identify the preferential formation of TiO_2 on the surface.

1.4 Surface and interface analysis

In this section two important surface analysis techniques that were applied within this work, shall be illustrated briefly: (i) Atomic force microscopy (AFM) and (ii) X-ray photoelectron spectroscopy (XPS). As both techniques are well established and available in numerous commercial setups only the aspects that are important for this work shall be summarized here.

1.4.1 X-ray photoelectron spectroscopy (XPS)

X-ray photoelectron spectroscopy (XPS) is a surface sensitive analysis technique that not only offers the elemental composition, but also gives information about the oxidation state or the type of bonds of the observed elements [80]. Usually, the information depth is limited to about 5 - 10 nm which makes XPS an outstanding tool to investigate the surface near region of a material.

Photoelectrons are excited via an X-ray source typically with the energy of $h\nu = 1486.7$ eV (corresponding to Al-k_α originating from an aluminum anode) or $h\nu = 1253.7$ eV in case of Mg-k_α. In the photoelectron process the incident X-ray photon

ejects an electron from a core level; the kinetic energy *KE* of the photoelectron is measured by an electron spectrometer. One is usually interested in the binding energy *BE* of the orbital, the photoelectrons originate from, as this energy is characteristic for a certain element with a certain core level transition. The binding energy can be determined by

$$BE = h\nu - KE - \Phi \tag{18}$$

where Φ is the work function of the spectrometer. Hence, all electrons with a lower binding energy than the incident photon energy *hν* can be ejected from their orbitals. Each core level can be identified by the following quantum numbers as shown in Figure 1.8.

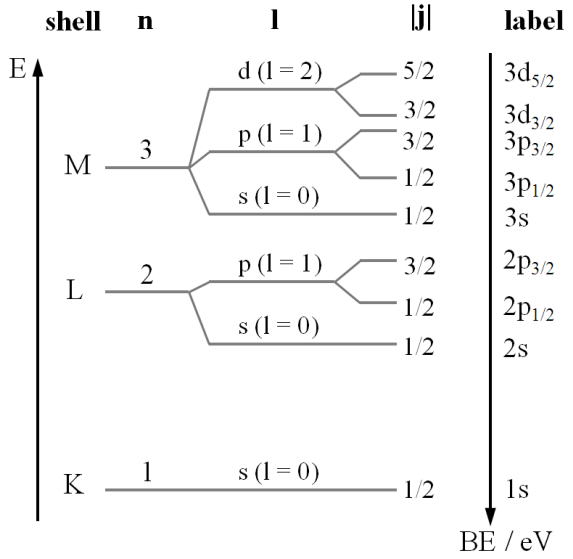

Figure 1.8: Schematics of different core levels and their corresponding quantum numbers and labeling.

n: principal quantum numbers (n = 1, 2, 3, ...) corresponding to the electron shells K, L, M, ...

l: azimuthal quantum number ($0 \le l \le n-1$), additionally referred as

s	for	l = 0
p	for	l = 1
d	for	l = 2
f	for	l = 3

j: total angular momentum quantum number |j| = l + s, where the spin quantum number *s* = ±1/2

For all core levels with l ≥ 1 the spectrum will split into a doublet due to the spin-orbit coupling. The relative population of the occupied states is given by (2j + 1). For example, this results for a 2p orbital where j = 1/2 and j = 3/2 in a population ratio of 2 : 4 which is directly reflected by the area of the measured 2p doublet peaks.

The information depth in XPS can be varied by the take-off angle of the photoelectrons, which is referred as angle resolved XPS (AR-XPS). Here the constraint should be kept in mind that the roughness of the sample should be not significantly higher than the information depth of XPS.

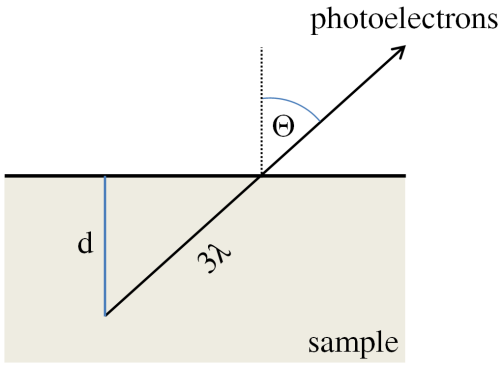

Figure 1.9: Scheme of the geometrics giving the information depth *d* as a function of the take-off angle *Θ*

Figure 1.9 shows some simple geometric considerations, where d is the information depth, λ is the attenuation length of the photoelectrons and Θ is the take-off angle of the photoelectrons with respect to the sample's surface normal. The typical attenuation length λ of the photo electrons in a solid can be estimated based on a square root law as a function of the kinetic energy [81]. Usually, λ is between λ = 1.5 to 3.0 nm in the energy range that is typically observed in a XPS spectrum excited with an Al-K_α X-Ray source at 1486.7 eV. The escape depth of the electrons is usually referred to 3λ; as 95 % of the photoelectrons originate from a depth of 3λ. As illustrated in Figure 1.9 the information depth d can be calculated as a cosine-dependent function of the take-off angle Θ [80]:

$$d = 3\lambda \cos\Theta \tag{19}$$

These considerations lead to specific information depths for each element and take-off angle of the photoelectrons and are only valid under the assumption of a homogeneous distribution of the elements within the probed surface layer. As an example, the probing

depths for some selected elements are given for different take-off angles of the photoelectrons in Table 1.2.

Table 1.2: Probing depth as a function of the XPS take-off angle [81, 82]

take-off angle to surface normal Θ / degrees	d /nm			
	Cr 2p	**O 1s**	**N 1s**	**Al 2s**
30	4.2	4.3	4.6	5.2
60	2.4	2.5	2.7	3.0
80	0.8	0.9	0.9	1.0

1.4.2 UHV and ambient pressure atomic force microscopy

The invention of the Scanning Tunneling Microscope (STM) by Rohrer and Binnig in the early 1980s opened a new door to ultrahigh resolution microscopy and was the first member of the scanning probe microscope (SPM) family [83]. In 1986 Binning, Quate and Gerber designed the Atomic Force Microscope (AFM) [84], which offers various powerful techniques for surface and interface analysis based on surface imaging techniques, surface manipulation in the nanometer scale and measuring of forces in the pN regime [85]. A huge advantage of the AFM technique is its high versatility providing various measuring modes for different applications and environmental conditions such as air, liquid or ultrahigh vacuum. Since these techniques are well established and available in numerous commercial setups today, place only a very short overview shall be given.

AFM is based on the principle that a sharp probe with a tip diameter of typically 5 – 10 nm usually made of Si or Si_3N_4, is attached to a microfabricated cantilever beam. The AFM cantilever can be positioned via a piezo system in all three room axis (x, y in sample plane, z perpendicular to the sample plane) with accurateness in the sub-nanometer-range. The AFM probe interacts with the sample surface, which causes the cantilever beam to bend due to the occurring interaction force between AFM tip and the substrate. The cantilever displacement is measured by a laser-optical detection system and represents the input-value for the measurement electronics.

1.4.2.1 AFM imaging

AFM imaging can be performed in various modes e.g. *contact mode*, *intermittent contact mode* or *non-contact mode* just to mention the most common ones. In all imaging modes the AFM tip is scanned line-wise across the sample surface to acquire an image. Dependent on the construction type of the AFM scanner, the imaging area is mostly limited to typically 100 x 100 μm^2 or even smaller. In *contact mode* the AFM tip is "dragged" along the sample surface, simultaneously the topography of the sample is reproduced by a feedback control that keeps the cantilever displacement – and thus the force applied to the surface – constant by moving the z-piezo perpendicular to the sample surface. Although the applied force is quite small (usually in the range of 1 – 10 nN), as a limitation of this imaging mode, rigid samples are required to avoid damage of the sample surface.

When "soft" samples such as polymers or even living cells shall be investigated, often the so called *intermittent contact mode* is used [86, 87]. In this mode the AFM cantilever is oscillated at an amplitude of a few tens of nanometers slightly below its resonance frequency. The resonance frequency of the cantilever is usually in the range of 20 - 300 kHz dependent on the mechanical characteristics of the cantilever and the medium (liquid or air environment) in which it is operated. An advantage of this mode is that the force applied to the sample can be controlled very carefully, as the oscillation amplitude of the cantilever is used as the lock-in value for the z-piezo feedback control. Typically the free oscillation amplitude is damped to values between 98 % (low force) and 40 % (high force) during imaging in contact with the sample.

Contact mode and *intermittent contact mode* are usually applied in air or liquid environments. However, ambient AFM experiments come along with the limitation that the interaction between the tip and the sample is also influenced by the environment, like capillary condensation in humid atmosphere [88]. Under UHV conditions these side-effects can be avoided which offers advanced imaging techniques to achieve ultimate resolution. Those experiments are usually performed in *noncontact mode*. Here the cantilever is also driven at its resonance frequency and the measurement is solely performed in the regime of attractive forces. As a lock-in signal the frequency shift of the cantilever – caused by the force interaction with the sample surface – is analyzed, which makes this method extremely sensitive for smallest interactions between the tip and the sample. By means of noncontact AFM Gross et al. studied the electronic structure of pentacene by using a single CO molecule adsorbed on an AFM tip as a probe [89]. Giessibl et al. observed subatomic features in the Si(111)-(7×7) structure [90], the chemical identification of single surface atoms is also possible as shown by Sugimoto et al. [91].

1.4.2.2 AFM force distance spectroscopy

As mentioned above, the AFM is also a powerful tool for measuring forces in the pN range. A common method of AFM force measurements is the technique of *force distance spectroscopy,* that has also been extensively applied and reviewed within the last years [85, 92]. Via the chemical modification of the AFM tip and/or the substrate, the interaction between single molecules or within biological systems can also be probed [93]. Within this work, the contact force between an AFM tip and a sample has been studied under UHV conditions, which has rarely been reported in the literature up to now, e.g. by Tadepalli et al. [53], Meine et al. [54] and Ozkaya et al. [94].

The interactions between cantilever and sample can basically be described by the interplay of attractive van der Waals forces and the repulsive forces caused by the Pauli exclusion principle which forbids orbitals with identical electron spin to overlap between AFM tip and sample. The overall potential between the AFM tip and the substrate can be basically be described by the well-known Lennard-Jones potential [95] that is shown in Figure 1.10 and gives the potential *W* as a function of the distance *r*

$$W \sim \frac{1}{r^n} - \frac{1}{r^6} \qquad \text{with n >> 6} \tag{20}$$

where the $-\frac{1}{r^6}$ term represents the longer range attractive van der Waals interactions and the $\frac{1}{r^n}$ term the very short range repulsive forces as caused by the Pauli repulsion. In many cases *n* is set to 12 to allow easy mathematical handling which leads to the so called Lennard-Jones-(12,6)-Potential.

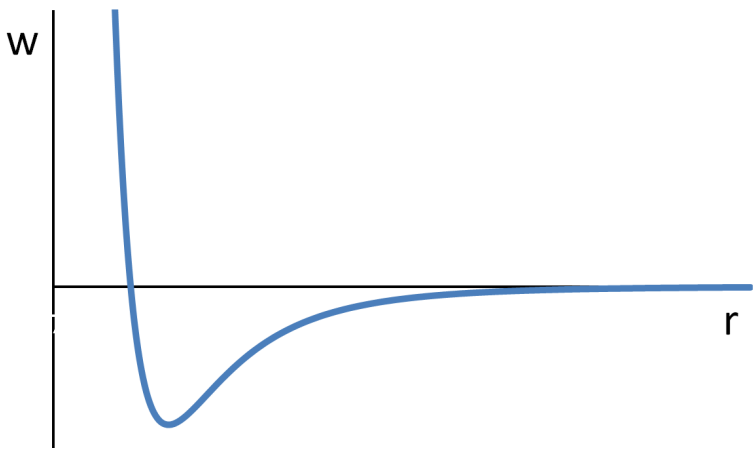

Figure 1.10: Lennard Jones potential, which described the overall interaction based on longer range attractive forces and short range repulsion

In AFM force-distance experiments the AFM tip is approached from a certain distance (e.g. in the range of 0.1 to 1 µm) to the surface. The attractive and repulsive interactions as discussed above lead to an ideal AFM force curve as presented in Figure 1.11 which shows the force *F* that is applied to the cantilever as a function of the z-piezo displacement *x*.

For large distances between the AFM tip and the sample the resulting force is close to zero. At low distances of several nanometers the attractive van der Waals forces cause the cantilever to jump to the surface which is called "snap in".

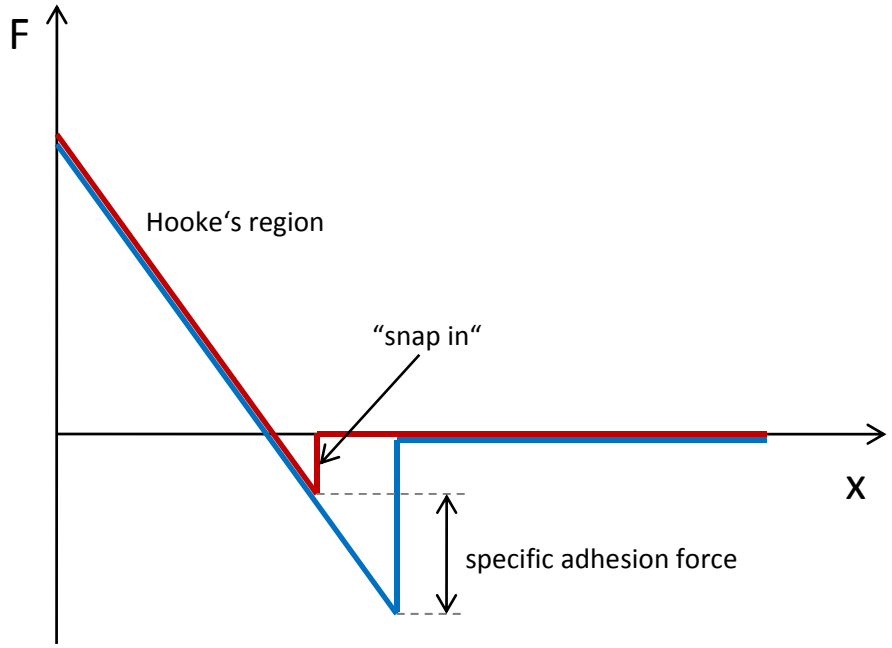

Figure 1.11: Idealized force-displacement plot for approach (red) and retraction (blue). When the cantilever is retracted from the surface, the adhesion force between tip and surface is observed.

Hooke's law can be applied for small deflections of the cantilever

$$F = k \cdot \Delta x_c \tag{21}$$

with F: applied force [nN]
k: spring constant [nN/nm]
Δx_c: displacement of the cantilever [nm]

When the cantilever is retracted from the surface usually a hysteresis between snap in and snap off is detected, that is caused by the specific adhesion between the AFM tip and

the sample in contact. This force can be correlated to adhesion phenomena which are determined by specific chemical binding such as hydrogen bonding, coordinative bonds or ligand – receptor interactions.

1.4.2.3 AFM force calibration

To measure a force accurately in an AFM experiment, the force constant k of the cantilever has to be known as referred in equation (21). The force calibration is usually performed in a two-step procedure:

(i) Determination of the sensitivity of the cantilever

At first the so called sensitivity Ω of the cantilever is determined from the slope of the Hookian part of the force-displacement curve in which the photodetector signal I is given as a function of the z-piezo displacement x:

$$\Omega = \frac{\Delta x}{\Delta I} \tag{22}$$

The sensitivity Ω is normally discussed in nm/V, which makes it possible to obtain the deflection of the cantilever directly in nanometers from the photodetector signal given in volts.

(ii) Determination of the force constant of the cantilever

The force constant can be determined by the so called “thermal-K method”, which uses thermally induced vibrations of the cantilever to calculate the force constant. The procedure is described in detail in the literature [96]. The thermally induced vibrational noise is recorded and Fourier-transformed in the time domain which leads to a power spectral density plot as a function of the frequency. This plot can be fitted and correlated to the thermal energy k_BT, which allows the calculation of the spring constant k in N/m. Within this calibration step it has to be kept in mind that significant errors up to 30 % may occur due to the mathematical modelling of the oscillating cantilever. Thus the obtained values for the force constant have to be discussed carefully.

Together with the sensitivity as discussed in equation (22) and Hooke's law (21), now the applied force *F* can be calculated directly from the deflection signal *I*:

$$F = I \cdot \Omega \cdot k \quad \text{and} \quad \left[nN = V \cdot \frac{nm}{V} \cdot \frac{nN}{nm} \right] \tag{23}$$

Although the force curve discussed in Figure 1.11 is strongly idealized, the force curves that were observed under UHV conditions within this work did not show significant differences. An example of a force curve obtained for a TiO_2 – TiO_2 nanocontact in UHV is presented in Figure 1.12.

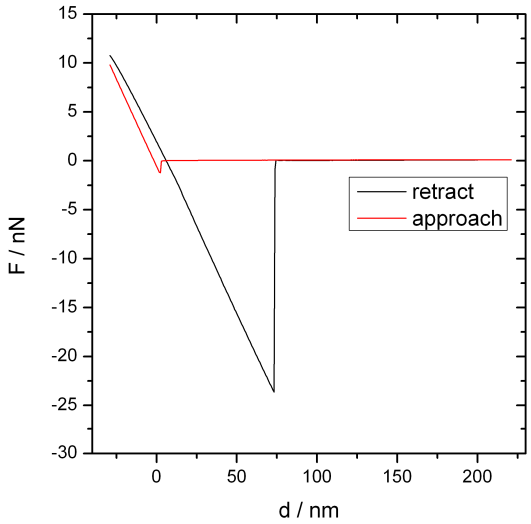

Figure 1.12: Exemplary AFM force curve obtained for a TiO_2 – TiO_2 nanocontact. The figure is also found in the supplementary material of [97].

The shown force curve is characterized solely by short range van der Waals interactions in the approach regime and a strong specific interaction in the retract part. It has to be noticed, that in the contact regime the approach and retract curve are not fitting which is a common problem of piezo nonlinearities such as creep or hysteresis. However these side effects can be neglected as they do not affect the measurement.

Chapter 2

2 Advanced experimental approaches

2.1 Time resolved XPS studies of oxygen chemisorption

Within this work the temporal evolution of the oxygen chemisorption was studied by means of time resolved XPS spectroscopy which is a highly interesting tool to study dynamic processes in the time range from a few seconds to several minutes. In contrast to classical XPS experiments, in which the observed energy has to be scanned over the energy range of interest (e.g. from 468 eV to 452 eV binding energy for Ti 2p), within these experiments each core level spectrum could observed within a single snapshot.

During the XPS measurement at each moment electrons of all kinetic energies are excited by the photoelectron process and are able to enter the spectrometer. Dependent on the settings of the electron optics and the setup of the analyzer/detector unit, only electrons of a small energy range (typically a few eV) can reach the detector generating the measured signal. Within the analyzer, the electrons are forced to a circular path. Hence, the exact location where the electrons exit the analyzer sphere (and reach the detector) gives information on the energy dispersion of the measured signal. Conventional electron detectors that are equipped with e.g. seven (or nine) channels would offer seven (or nine) reading points, corresponding to the number of channeltrons available. If the used electron detector offers a high spatial resolution, a whole core level peak can be acquired with a satisfying energy resolution as shown in Figure 2.1, at once. Within this work a 128 channel detector (*Argus*, Oxford Instruments) has been used.

The width of the energy region that is observed by the electron spectrometer is dependent on the pass energy of the photoelectrons that is set for the experiment. The pass energy correlates linearly with the width of the photoelectron energy range that is observed by the spectrometer. For the spectrometer used in this work, the observed energy range is ΔE = 14.3 eV at 100 eV pass energy and ΔE = 7.2 eV at 50 eV pass energy.

For the time resolved XPS experiments performed within this work, the pass energy was set to 100 eV to cover the whole Ti 2p core level peak. XPS spectra of the O 1s, Ti 2p, N 1s and Al 2p core level peaks were successively measured in the so called “snapshot mode”. The acquisition time per element spectrum was set to four seconds to achieve a satisfying signal to noise ratio. Hence, the time resolution of the experiment was 26 s per loop cycle, that resulted from 4 s each per core level spectrum and about 2.5 s for switching

the analyzer energy after each measurement. When using this mode it is important to calibrate the sensitivity of the 128 channels according to the proceedings given by the manufacturer to achieve reliable results.

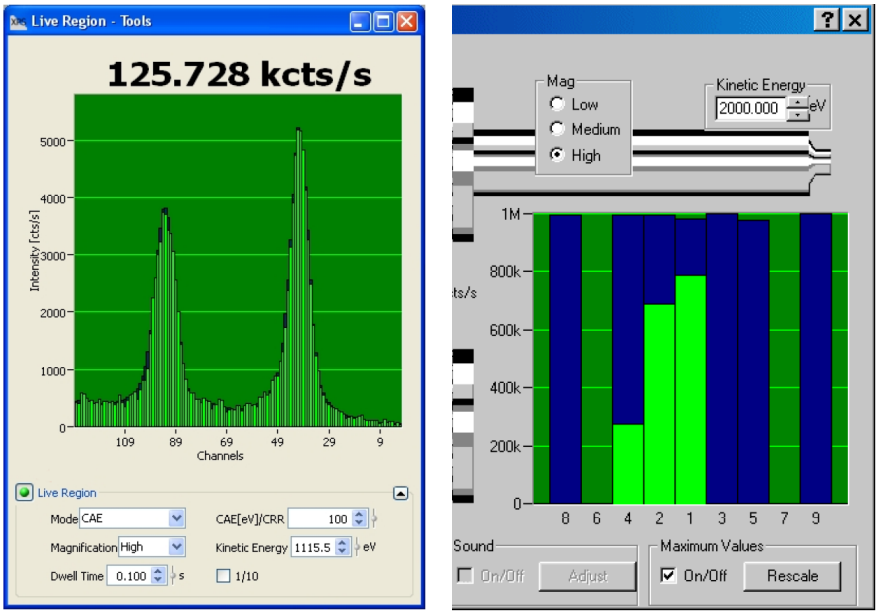

Figure 2.1: Comparison of a 128 channel detector (left) and a 9 channel detector (right). Due to the high number of channels die whole doublet peak can be resolved sufficiently (left) which is not possible for the conventional detector (right). The screenshots were taken from the *Omicron Oxford* photoelectron spectroscopy control software.

In order to create a bare TiAlN surface the native oxide layer of the sample was removed by Ar^+ sputtering with 2 keV for 300 s. Afterwards the re-oxidation of the TiAlN surface was triggered by introducing oxygen into the XPS chamber via the leak valve of the Ar^+ sputter source. During oxygen dosing the pressure in the XPS chamber was increased from the base pressure of $p_{base} = 1 \cdot 10^{-9}$ mbar to $p_{dosing} = 1 \cdot 10^{-8}$ mbar, which resulted in an oxygen partial pressure of $p_{O2} = 0.9 \cdot 10^{-8}$ mbar with simultaneous acquisition of snapshot mode XPS spectra as discussed above.

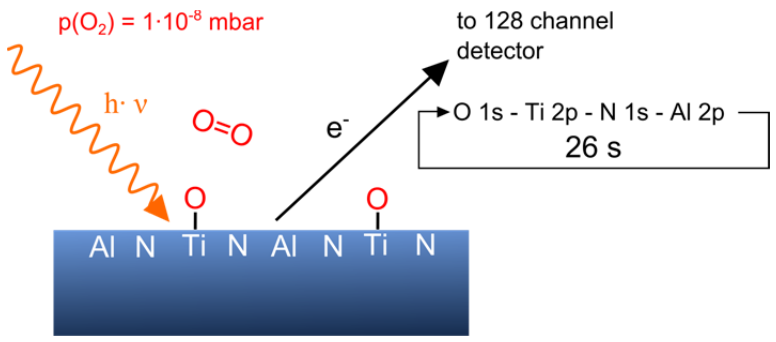

Figure 2.2: Schematics of time resolved XPS experiments

2.2 UHV-AFM force distance measurements and combined surface analysis on single crystal oxides

Within this work subsequent surface preparation, analysis by means of XPS and UPS (UV photoelectron spectroscopy) and UHV-AFM contact force experiments were performed within the same UHV analytical setup as presented in Figure 2.3.

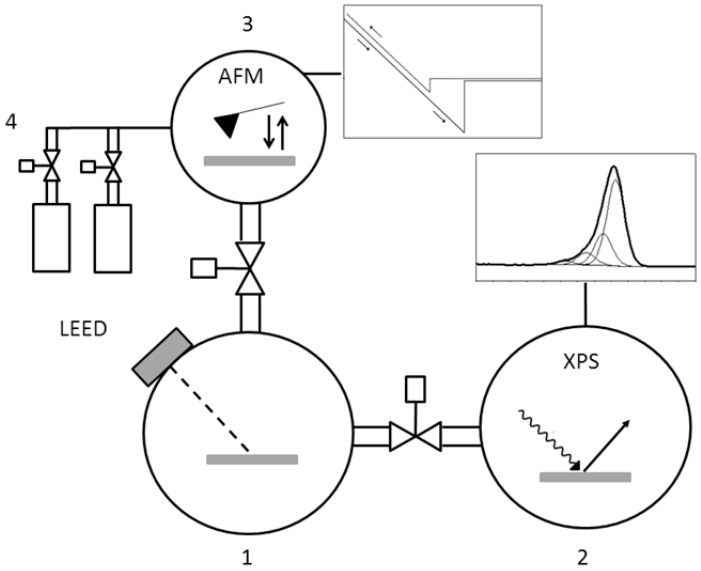

Figure 2.3: Illustration of the UHV analytical setup allowing the measurement of surface chemistry and contact forces. 1) preparation chamber; 2) analysis chamber; 3) AFM chamber; 4) gas and water dosing system

Prior to these experiments, both TiO_2 surfaces – the TiO_2(110) substrate and the TiO_2 coated AFM tip – were cleaned by gentle Ar^+ sputtering with an ion-energy of 200 eV, which resulted in the complete removal of carbon contaminations after 12 minutes for the TiO_2(110) single crystalline substrate and 15 minutes for the TiO_2 modified AFM tip. Here it has to be checked carefully that the AFM tip is mounted upside-down on the sample manipulator so that the tip apex is located within the sputter area of the Ar^+ source.

UHV-AFM force distance curves were obtained from an overlying 16 x 16 point grid on a 2 x 2 μm^2 probing area. The approach and retract speed of the AFM tip was set to 1 µm/s, the overall distance of each force curve was 250 nm. The measured forces were calibrated based on the sensitivity of the AFM setup derived from the force curve and the nominal spring constant of the AFM cantilever.

The obtained force curves were analyzed for the lowest value of the retraction curve which represents the contact force as shown in Figure 1.12. To allow data analysis on a

statistical basis, at least 330 force values were evaluated for each set of experiments. The obtained contact force values were displayed in histograms (as exemplary shown in Figure 2.4) giving the number of observed force curves as a function of the contact force. The width of the histogram bins showing the number of the observed contact force events was set to 1 nN.

For water dosing within the AFM chamber a reservoir with ultrapure water was attached to a gas dosing system that featured a capillary with a distance to the sample of about 10 mm to allow targeted water dosing. Via a leak valve system water was dosed until the pressure of within the AFM chamber was increased from $p_{base} = 1 \cdot 10^{-9}$ mbar to $p_{dosing} = 3 \cdot 10^{-8}$ mbar for 30 minutes. After the contact force mapping the sample was transferred to the analysis chamber for XPS and UPS studies. In the following step the TiO_2(110) sample was transferred back to the SPM chamber, annealed at 473 K for 30 minutes followed again by AFM force mapping and electron spectroscopy within the analysis chamber.

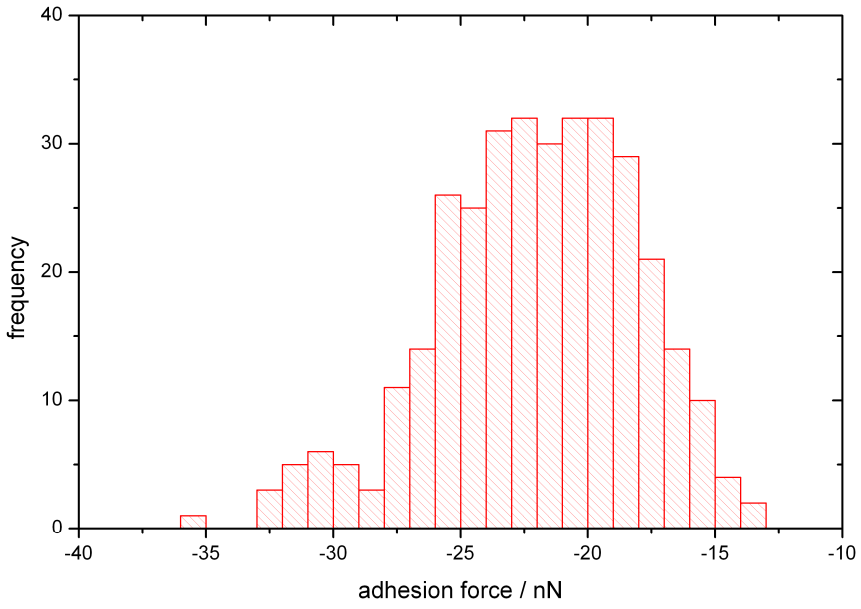

Figure 2.4: Example of a histogram giving the event frequency as a function of the observed adhesion force. The overall number of data points is 330.

Chapter 3

3 Publications

In this chapter the publications that were generated within this work are presented. Overall six publications, where four publications are main author contributions (*) and two publications are second author contributions (**), are relevant for the here presented thesis and are located in a coherent context. The following publications will be discussed:

I** C. Gnoth, **C. Kunze**, M. Hans, M. to Baben, J. Emmerlich, J.M. Schneider, G. Grundmeier
Surface chemistry of TiAlN and TiAlNO coatings deposited by means of high power pulsed magnetron sputtering
Journal of Physics D-Applied Physics, 46 (2013), 084003.

II* **C. Kunze**, R. H. Brugnara, N. Bagcivan, K. Bobzin, G. Grundmeier
Surface Chemistry of PVD (Cr,Al)N coatings deposited by means of Direct Current and High Power Pulsed Magnetron Sputtering
Surface and Interface Analysis, 45 (2013), 1884-1892.

III** N. Bagcivan, K. Bobzin, G. Grundmeier, M. Wiesing, Ö. Özcan, **C. Kunze**, R. H. Brugnara
Influence of HPPMS Pulse Length and Inert Gas mixture on the Properties of (Cr,Al)N Coatings
Thin Solid Films, 549 (2013), 192-198.

IV* **C. Kunze**, D. Music, M. to Baben, J.M. Schneider, G. Grundmeier
Temporal evolution of oxygen chemisorption on TiAlN
Applied Surface Science, 290 (2013), 504-508.

V* **C. Kunze**, B. Torun, I. Giner, G. Grundmeier
Surface chemistry and nonadecanoic acid adsorbate layers on TiO_2(100) surfaces prepared at ambient conditions
Surface Science, 606 (2012), 1527-1533.

VI* **C. Kunze**, I. Giner, B. Torun, G. Grundmeier
Influence of the surface chemistry on TiO_2 - TiO_2 nanocontact forces as measured by an UHV-AFM
Chemical Physics Letters, 597 (2014), 134-138.

Within publication **I** the chemical composition of the surface near region of TiAlN(O) surfaces was investigated in detail for the first time by means of angle resolved XPS experiments. It could be shown that the composition of the surface near region significantly differs from the bulk composition of the coatings which had not been taken into account yet when discussing the interaction of such a coating with a polymer(melt).

These results have been transferred to the related materials of the composition CrAlN as discussed in publication **II**. Within this work – based on the previous publication – the influence of the HPPMS sputter process parameters have also been investigated more detailed. It could be shown that the tendency of the surface near region to incorporate oxygen can be influenced by the choice of adequate process parameters.

The influence of the process parameters during the deposition of CrAlN not only on the surface composition but also on bulk properties (such as hardness and morphology) have been investigated in **III**. These results can be nicely correlated to the previous work.

As the question of oxygen chemisorption and further incorporation into the surface near region of *M*AlN(O) is of crucial interest towards designing tailored materials, the initial chemisorption of oxygen on TiAlN was investigated in **IV.** Interestingly the oxygen chemisorption is determined by the reaction of titanium with oxygen along with the formation of titanium vacancies – not by the reaction of aluminum with oxygen which would the favored because of thermodynamic reasons.

The interaction of titanium oxide surfaces with organic molecules was studied in **V**. Here, atmospherically prepared TiO_2 single crystalline surfaces were evolved as a model system to study the interactions on a fundamental level.

Based on the employment of atmospherically prepared single crystalline surfaces as discussed previously the interaction forces in TiO_2 – TiO_2 nanocontacts were studied under UHV conditions in **VI**. It could be shown that the state of the surface in terms of defect density is of crucial importance for the observed contact force. As the formation of defects is also important for the interactions at TiAlN surfaces as discussed in **IV**, such experiments might offer interesting studies for future work.

3.1 Surface chemistry of TiAlN and TiAlNO coatings deposited by means of high power pulsed magnetron sputtering

Christian Gnoth, Christian Kunze, Marcus Hans, Moritz to Baben, Jens Emmerlich, Jochen M. Schneider, Guido Grundmeier
Journal of Physics D - Applied Physics, 46, **2013**, 084003.

The scientific work and discussion was coordinated and consolidated by CK under supervision of GG.
The manuscript was prepared by CK based on preliminary work of CG; MtB contributed to the introduction of the manuscript.
Hard coatings were deposited by MH and MtB.
EDX measurements and data evaluation were performed by MtB and JE.
XRD measurements and data evaluation were performed by JE.
XPS measurements and data evaluation were performed by CK and CG.
The manuscript was revised by GG and JMS.

This publication is in context of the master thesis of C. Gnoth ("Surface chemistry and wetting properties of TiAlON and CrAlON plasma layers", January 2012) under supervision of C. Kunze at the chair of Technical and Macromolecular Chemistry of Prof. Dr.-Ing. G. Grundmeier. The work of the master thesis has been performed on a different set of TiAlNO coatings that have been deposited with varying parameters as discussed in the publication below.

Within this paper the chemistry of the surface chemistry of TiAlN and TiAlNO hard coatings has been investigated. It could be shown that the surface near region of the investigated coatings is enriched with oxygen in comparison to the bulk composition. As this coating system is used during cutting and polymer forming operations, the here established difference between the bulk composition of the coating and the composition of the surface near region of the coating is of great relevance for understanding interfacial dominated interactions.

IOP Publishing Journal of Physics D: Applied Physics
J. Phys. D: Appl. Phys. **46** (2013) 084003 (7pp) doi:10.1088/0022-3727/46/8/084003

Surface chemistry of TiAlN and TiAlNO coatings deposited by means of high power pulsed magnetron sputtering

C Gnoth[1], C Kunze[1], M Hans[2], M to Baben[2], J Emmerlich[2], J M Schneider[2] and G Grundmeier[1]

[1] Technical and Macromolecular Chemistry, University of Paderborn, Paderborn, Germany
[2] Materials Chemistry, RWTH Aachen University, Aachen, Germany

E-mail: g.grundmeier@tc.uni-paderborn.de

Received 10 August 2012, in final form 17 October 2012
Published 1 February 2013
Online at stacks.iop.org/JPhysD/46/084003

Abstract
It is shown that the investigated TiAlN and TiAlNO protective coatings show an enrichment of oxygen in the surface near region with concurrently higher oxidation states of titanium. We suggest that surface oxidation is caused by reaction with atmospheric oxygen at room temperature and/or with residual gas immediately after deposition during cooling in the chamber. As this coating system is used during cutting and forming operations, the here-established difference between the coatings composition and the composition of the surface near region of the coating is of great relevance for understanding the interactions thereof with the materials to be cut or formed.

(Some figures may appear in colour only in the online journal)

1. Introduction

TiAlN is widely used as protective coating for cutting and forming tools due to the high hardness combined with good oxidation and wear resistance [1, 2]. It has been proposed that by incorporation of oxygen TiAlNO can be used as protective coating in contact with molten JIS ADC 12 aluminum alloy [3] and for processing of transparent polymers [4]. By deposition of CrAlNO coatings on a steel extruder, the number of low-quality components formed could be decreased nearly by a factor of three [5]. In order to investigate the basic mechanisms leading to the low adhesion between polymers and *M*AlNO (*M* = Ti, Cr) coatings, the interface between polypropylene and *M*AlN and *M*AlNO was recently studied by *ab initio* calculations [6]. It was shown that the work of separation between polypropylene and defect-free $M_{0.5}Al_{0.5}N$ and $M_{0.5}Al_{0.5}N_{0.5}O_{0.5}$ surfaces is very small and in the same order of magnitude as decohesion energies for V_2O_5 [7]. Radicals, which may be formed by e.g. shearing of the polypropylene melt [8, 9], increase the work of separation by two orders of magnitude [6]. In the *ab initio* calculations $M_{0.5}Al_{0.5}N$ or $M_{0.5}Al_{0.5}N_{0.5}O_{0.5}$ surfaces as well as $Ti_{0.5}Al_{0.5}N$ surfaces with agglomerated surface vacancies were considered [6]. Under technical conditions, after deposition, a coated tool surface will be exposed to ambient atmosphere which can lead to a change in the chemical composition of the surface near region.

However, reactions may also occur during deposition between the surface near region of the coating and residual gases present in the deposition chamber. In high vacuum the residual gas is mainly H_2O [10]. Hence, oxygen and hydrogen stemming from residual gas may be incorporated during growth [10]. High plasma density pulse discharges [11] and the presence of magnetic fields [12] were shown to result in efficient ionization of residual gases. Furthermore, it has been reported that ion bombardment reduces the amount of incorporated H [13], as hydrogen is desorbed from the surface near region of the coating during growth [14]. However, oxygen stemming from H_2O is expected to be incorporated during ion-assisted growth as the oxide bond energies are significantly larger than for hydroxyls or hydrides. The surface near region of an as-deposited TiAlN or TiAlNO coating may be further oxidized in the deposition chamber immediately after deposition during the cool down sequence by residual gas. It is also reasonable to assume that upon exposure to air at room temperature and ambient pressure oxidation of the surface near region and surface adsorption may occur as the partial pressures of water and oxygen as well as small organic

Table 1. Deposition parameters.

Sample no.	Ar-flow (sccm)	N_2-flow (sccm)	O_2-flow (sccm)	p(Ar) (mPa)	p(N_2) (mPa)	p(O_2) (mPa)	Thickness (μm)
1	200	75	0	347	137	0	1.4
2	200	75	5	347	137	6	1.4
3	200	75	8	347	137	10	1.1
4	200	75	12	347	137	15	0.7

molecules are significantly higher than under high vacuum conditions.

Angle resolved x-ray photoelectron spectroscopy (AR-XPS) measurements were reported for amorphous TiAlN coatings showing that the surface near region was partly oxidized and enriched with Al due to air exposure [15]. To the best of the authors' knowledge, no data on the composition of the surface near region and gradients therein were reported to date for crystalline TiAlN and TiAlNO. Therefore, the goal of this work is to identify the surface near composition of TiAlN and TiAlNO in order to contribute towards understanding surface phenomena, such as the mechanisms leading to low adhesion between polymers and MAlNO coatings. Furthermore, surface near composition data are instrumental for compiling realistic models describing the interaction between the coating and material to be formed or cut.

TiAlN and TiAlNO coatings were deposited by high power pulsed magnetron sputtering (HPPMS) [16, 17] and the resulting structure, composition and thickness were analysed by x-ray diffraction (XRD), energy-dispersive x-ray spectroscopy (EDX) and scanning electron microscopy (SEM), respectively. To study the composition of the surface near region and gradients therein, AR-XPS was used. AR-XPS is highly surface sensitive and allows the determination of the chemical composition and chemical states. Experiments at varying take-off angles allow obtaining chemical composition gradients on the nm scale.

2. Experimental

2.1. Materials and chemicals

All chemicals were used without further purification. Isopropanol, tetrahydrofuran and ethanol for cleaning purposes were purchased in p.a. grade from VWR International, Germany. Silicon wafers of orientation Si(1 0 0), (p-doped with boron, single-side polished) were purchased from Si-Mat, Kaufering, Germany.

All surfaces were cleaned with organic solvents before analysis. The samples were sonicated in tetrahydrofuran, isopropanol and ethanol for 15 min each and rinsed with clean solvent before the next cleaning step. After rinsing with pure ethanol the samples were dried in a flow of pure nitrogen gas.

2.2. Deposition parameters

The coatings were deposited on electrically floating Si(1 0 0) substrates by HPPMS in a CC-800/9 CemeCon deposition chamber using a 500 × 88 mm^2 TiAl sputter target consisting of a Ti plate with inlays of Al leading to a Ti/Al ratio close to 1. The target voltage was set to 700 V at 450 Hz and the pulse-on-time was 200 μs, leading to a time average power density around 10.5 W cm^{-2}. The pulse shape was similar to the one reported in [18] (figure 2). The target-to-substrate distance was 155 mm and the base pressure was 0.15 mPa. $Ti_{0.5}Al_{0.5}N_{1-x}O_y$ coatings were synthesized in an Ar/N_2/O_2 atmosphere at 420 °C substrate temperature for 100 min. The Ar and N_2 flows were kept constant at 200 sccm and 75 sccm, respectively. The O_2 flow was set to 0 sccm, 5 sccm, 8 sccm and 12 sccm in four deposition runs, respectively. The resulting partial pressures are shown in table 1. Throughout the deposition experiments the target was kept in the metallic sputter mode.

Table 2. Probing depth as a function of the XPS take-off angle [19].

Take-off angle Θ (°)	Probing depth (nm)
30	2.60
60	1.50
80	0.52

2.3. Analytical methods

AR-XPS measurements were performed by means of an Omicron ESCA+ System (Omicron NanoTechnology GmbH, Germany) with a base pressure of $<3 \times 10^{-11}$ mPa. The system is equipped with a hemispherical energy analyser, the element spectra were recorded at pass energies of 25 eV. For photoelectron excitation a monochromated Al-Kα (1486.3 eV) x-ray source with a spot diameter of 600 μm was used. The take-off angle of the detected photoelectrons was varied from 30° to 80° with respect to the surface normal. The calibration of the spectra was performed using the C 1s peak (binding energy, BE = 285.0 eV) as an internal reference. For data evaluation the CasaXPS software was used. All quantification of the XPS data was done by integration of the peaks with regard to the relative sensitivities of the elements.

Estimating the typical attenuation length of the photoelectrons in a solid to $\lambda =\sim 3$ nm (for an Al-K_α X-Ray source at 1486.3 eV), the probing depth d can be calculated from geometric considerations as a cosine-dependent function of the take-off angle Θ [19] and the attenuation length λ according to table 2:

$$d = \lambda \cos \Theta. \quad (1)$$

Chemical composition analysis of the bulk coating was carried out in a JEOL JSM-6480 SEM with an EDAX Genesis 2000 EDX detector at 12 kV acceleration voltage.

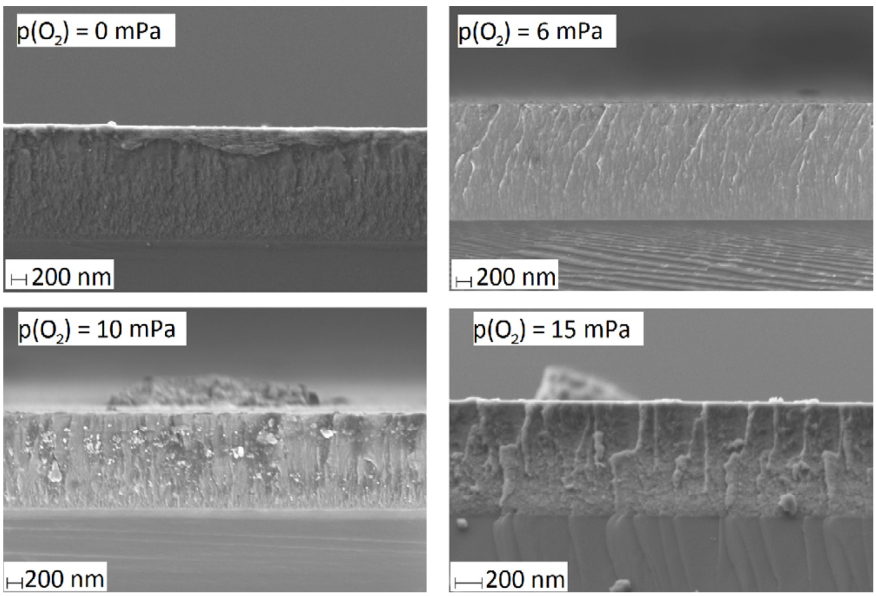

Figure 1. SEM cross-sectional images of the investigated TiAlNO coatings. The Si wafer substrate (bottom) can be clearly distinguished from the TiAlNO coating (middle).

XRD was performed by means of a Siemens D5000 XRD system with a Cu-K_α radiation source in the Θ–2Θ configuration.

For the analysis of TiAlNO cross sections a Zeiss Neon 40 SEM was used. The applied electron acceleration voltage was 2.00 kV at a working distance of 4.1–5.5 mm. The aperture size was 30.00 μm. The pressure in the analysis chamber was below 0.002 mPa. Cross section samples were prepared by scratching the backside of the Si wafer substrate with a diamond cutter followed by breaking the sample.

3. Results and discussion

3.1. Coating morphology

The investigated TiAlNO coatings had a thickness between 0.7 and 1.4 μm. The coating thickness was determined by SEM from cross section samples, as shown in figure 1. As the information depth from the AR-XPS experiments is limited to about 3 nm, only the surface near region of the TiAlNO coatings is measured and no effects of the underlying silicon wafer substrates are expected. According to the SEM analysis the surface shows a roughness of less than a few nanometres.

3.2. EDX analysis

The coating composition as measured by EDX is shown in figure 2 as a function of the oxygen partial pressure. While quantitative analysis is not possible with EDX for light elements and due to peak overlap between the Ti–L line and O–K and N–K lines, the results can be discussed only qualitatively. For the coating without intentional oxygen addition, a small amount of oxygen in the range of 1 at% is detected. With increasing oxygen partial pressure the oxygen

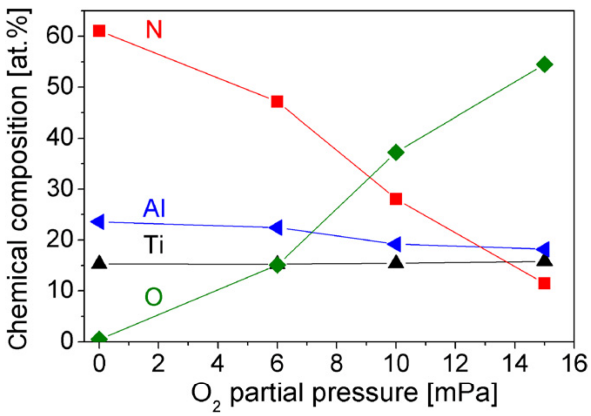

Figure 2. Composition of the coatings as determined by EDX measurements.

content in the coating increases at the expense of nitrogen. A crossover from a nitrogen rich to an oxygen rich coating is observed based on the EDX data for the coating deposited at an oxygen partial pressure of 10 mPa.

When comparing the composition of the coating to the composition of the gas phase it is found that even though the $N_2 : O_2$ partial pressure ratio is 14 : 1, the coating is more oxygen rich. This can be understood based on the higher affinity of titanium and aluminum to oxygen compared with nitrogen. Additionally, it can be observed that the aluminum content in the coating is slightly decreased with increasing oxygen content. This could be due to target poisoning as the sputter yield of the oxide is smaller compared with the nitride [20, 21]. This assumption is also consistent with the lower deposition rate measured with increasing oxygen partial pressure. Without intentional oxygen incorporation, i.e. in

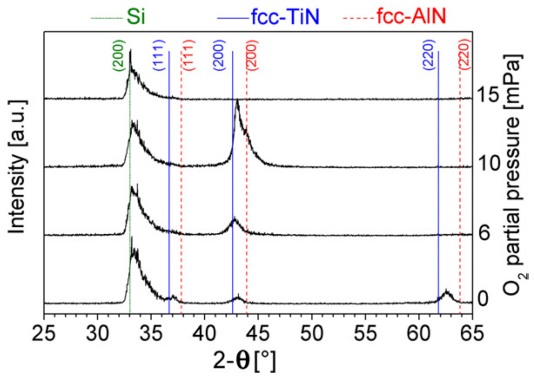

Figure 3. Diffractograms of the investigated samples. Note that the Si(2 0 0) peak at 33° is caused by the underlying Si substrate.

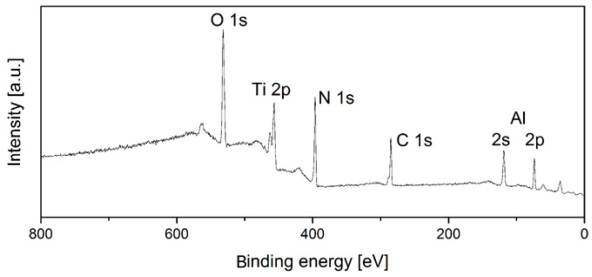

Figure 4. Typical XPS survey spectrum of the surface near region of a TiAlON coating. The shown spectrum was measured for sample 1 ($p(O_2) = 0$ mPa) at a take-off angle of 60° with respect to the surface normal.

the nitridic mode, the deposition rate is 15 nm min^{-1}, which is decreased to 9 nm min^{-1} for an oxygen partial pressure of 15 mPa.

3.3. XRD analysis

The results of the XRD analysis are shown in figure 3 as a function of the oxygen partial pressure during deposition. Coatings deposited at an oxygen partial pressure up to 10 mPa exhibit an fcc-nitride structure. The coating deposited without intentional oxygen addition is randomly textured. With increasing oxygen content, (2 0 0) fibre texture is observed, which points to different mobility and/or surface energies due to oxygen incorporation. A (2 0 0) peak splitting is observed for the oxygen partial pressure of 10 mPa. This is similar to previously reported diffractograms indicating spinodal decomposition into TiN and AlN rich domains during growth of TiAlN [22, 23]. Clustering into TiN and AlN rich regions in the as-deposited state has been reported for TiAlN coatings recently [24, 25].

The sample deposited at the highest oxygen partial pressure was *x*-ray amorphous. The formation of an amorphous phase has been observed for TiAlNO coatings for higher oxygen contents and was argued to be due to a chemical driving force for decomposition as well as decreased energy of the ion bombardment due to increase in resistivity of the growing film [26].

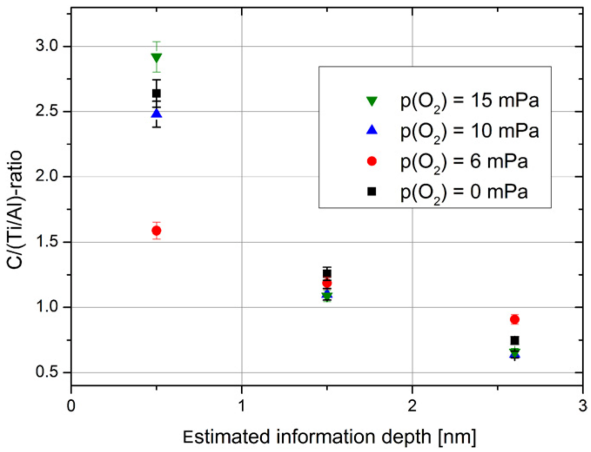

Figure 5. C/(Al+Ti)-ratios in the TiAlNO coatings as a function of the oxygen partial pressure and estimated information depth.

3.4. XPS analysis

The chemical composition of the surface near region was analysed to compare the chemistry of the surface near region to the bulk composition of the coatings deposited at different oxygen partial pressures.

A survey XPS spectrum, qualitatively representative for all samples, is shown in figure 4. The XPS analysis section is organized as follows: first, the origin of the C 1s peak is discussed, then the chemical composition in the surface near region is analysed from peak areas in AR-XPS spectra and last the oxidation state is studied from the change in binding energy.

The C/(Ti+Al) ratio for all samples is plotted in figure 5 as a function of the estimated information depth. Since the C 1s peak is used for energy calibration, no peak shifting can be observed for different samples or different sample depths. A uniform peak shape was observed for all samples and probing depths (not shown for brevity). Thus, the chemical properties of the carbon signal do not change with the composition of the TiAlNO coating. Carbon contents of 18 at% and 48 at% were observed for probing depths of 2.6 nm and 0.5 nm, respectively, showing that the carbon signal originates at the surface. Within our data no correlation between the carbon contamination and the surface chemistry of the coating was found. It can be concluded that the observed carbon peak does not originate from the coating and is a consequence of adsorption upon contact with the environmental atmosphere. Thus, no impact of carbon on the surface chemistry of the TiAlNO coating is expected and the carbon data are excluded from further discussion.

The chemical compositions of the investigated coatings are shown in figure 6 in at%. The XPS results show that increasing O_2/N_2-ratios in the plasma lead to increasing oxygen concentrations in the surface near region, which is in good agreement with the EDX results. Again a small partial pressure of oxygen leads to high O/N-ratios in the coating. In addition, an enrichment of oxygen in the surface near region can be derived from the XPS data.

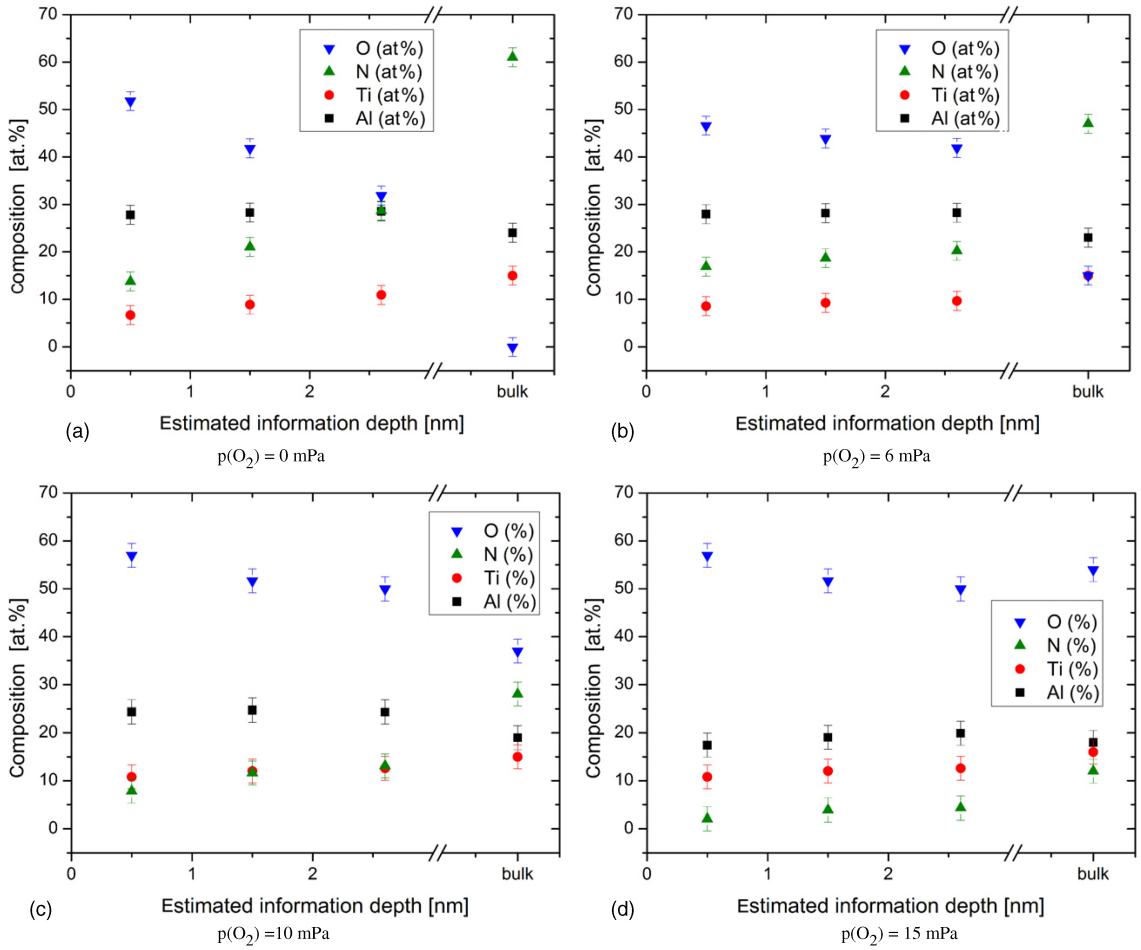

Figure 6. Compositions of the surface near region as measured by AR-XPS and of the coating as measured by EDX for samples deposited at different O_2 partial pressures.

Table 3. Atomic ratios calculated from AR-XPS composition data. The calculated element ratios include an estimated error of 4%.

AR-XPS	30°	60°	80°	30°	60°	80°
	$p(O_2) = 0$ mPa			$p(O_2) = 6$ mPa		
O_2/N_2 gas flow	0	0	0	0.07	0.07	0.07
O/N	1.1	2.0	3.8	2.0	2.4	2.8
Al/Ti	2.6	3.2	4.2	2.9	3.0	3.3
O/(Al+Ti)	0.81	1.13	1.50	1.11	1.17	1.28
N/(Al+Ti)	0.73	0.57	0.40	0.53	0.50	0.46
	$p(O_2) = 10$ mPa			$p(O_2) = 15$ mPa		
O_2/N_2 gas flow	0.11	0.11	0.11	0.16	0.16	0.16
O/N	3.8	4.5	7.3	13.8	15.6	31.3
Al/Ti	1.9	2.1	2.3	1.2	1.2	1.1
O/(Al+Ti)	1.35	1.41	1.62	1.65	1.73	1.96
N/(Al+Ti)	0.36	0.32	0.22	0.12	0.11	0.06

A comparison of some important ratios of elements as derived from the quantification of the XPS spectra is shown in table 3. For the coatings deposited at oxygen partial pressures up to 10 mPa a similar trend is observed. The O/N ratio increases close to the surface as the incorporation of

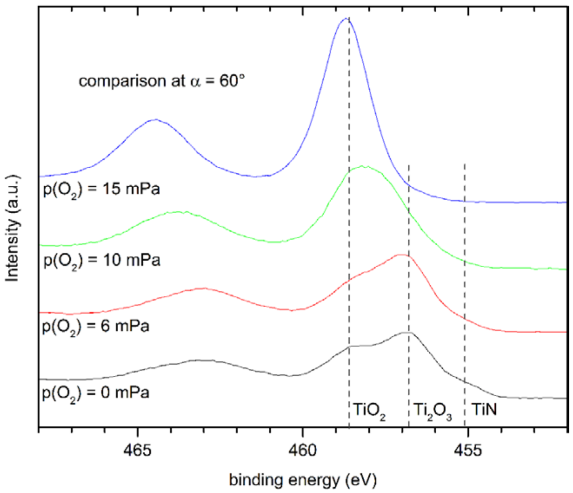

Figure 7. Ti 2p detail spectra of the TiAlON coatings. A shift to higher binding energies shows a higher state of oxidation of titanium in the coating.

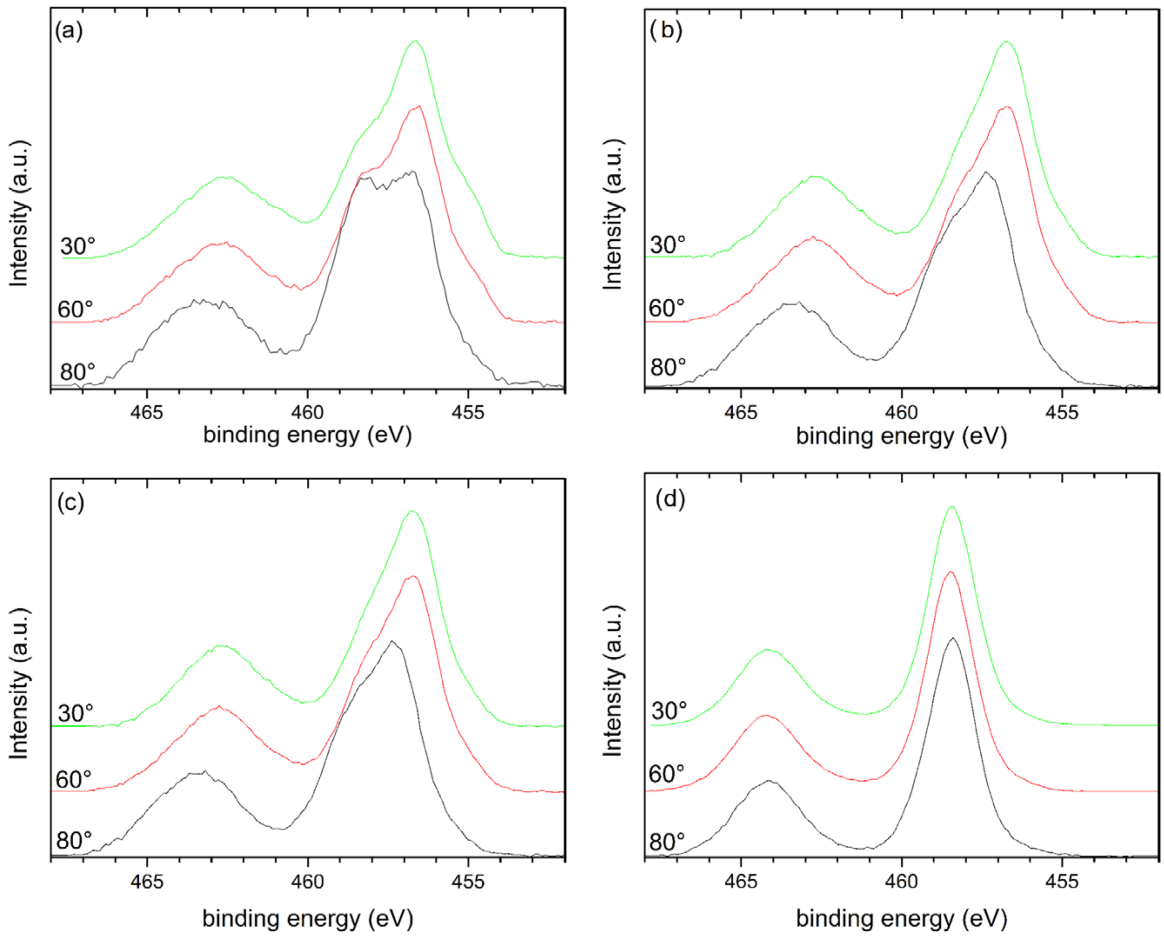

Figure 8. Comparison of spectra of samples deposited at different oxygen partial pressures. (*a*) p(O_2) = 0 mPa, (*b*) $p(O_2) = 6$ mPa, (*c*) $p(O_2) = 10$ mPa, (*d*) $p(O_2) = 15$ mPa.

oxygen along with surface oxidation is thermodynamically favoured. Moreover, the Al/Ti ratio is also increased towards a higher concentration of aluminum close to the surface.

The increase of the amount of oxygen towards the surface indicates that an oxidation process of the TiAlNO coating occurs after the end of the deposition process. Oxygen chemisorption within the deposition chamber after the deposition process and during atmospheric exposure cannot be separated based on the *ex situ* analysis.

The fact that long term exposure, over several months, of the coating deposited at $p(O_2) = 0$ mPa to ambient atmosphere did not show any significant increase in oxygen concentration indicates fast kinetics of the oxidation reaction immediately after coating deposition.

The element spectra of titanium (Ti 2p) show peaks of two different species which are shifted to higher binding energies in comparison with elemental titanium, as shown in figures 7 and 8.

A comparison with data from the literature [15] suggests the existence of titanium nitrogen compounds (TiN with BE(Ti^{III}) = 455.1 eV) and two titanium oxide species (Ti_2O_3 with BE(Ti^{III}) = 456.8 eV, TiO_2 with BE(Ti^{IV}) = 458.6 eV). The corresponding spectra are shown in figure 8. Since a higher take-off angle (α) leads to strongly decreased integral intensities, the intensities were normalized for a better comparison of the angle-resolved spectra of a sample.

At a higher take-off angle with respect to the surface normal a shift towards an increased concentration of TiO_2 can be observed, as shown in figure 8. This proves the assumption of a higher oxidation of the surface compared with the bulk and a gradient in the surface-near region of the coatings.

When increasing the oxygen partial pressure during deposition from 0 to 10 mPa and when increasing the take-off angle towards higher surface sensitivity the contribution of Ti^{IV} in comparison with Ti^{III} increases. For the coating deposited at $p(O_2) = 15$ mPa a single contribution of Ti^{IV} in the Ti 2p core level signal is visible which correlates well with the extremely low nitrogen content in the surface near region.

In the Al 2s spectra, no significant peak shift could be observed as the Al–O and Al–N bonds are very similar in energy [26]. However, due to the concurrently increasing intensity of Al and O when decreasing the probing depth and the enthalpies of formation, it is reasonable to assume that aluminum preferably bonds to oxygen.

4. Conclusions

In this work TiAlN and TiAlNO coatings were deposited and analysed with XRD, EDX and AR-XPS to investigate structure, composition and composition gradients within the surface near region, respectively. All crystalline coatings exhibit a several nm thick oxidized surface near region including the TiAlN coatings deposited under high vacuum conditions without the addition of oxygen as a process gas. Using AR-XPS it could be shown that the oxygen content increases in the surface near region. Surface concentrations of oxygen ranged from 40 to 60 at%.

Surface oxidation may be due to reaction with atmospheric oxygen at room temperature and/or with residual gas immediately after deposition during cooling in the chamber.

These results are significant for understanding the performance of TiAlN and TiAlNO coatings on forming tools e.g. of polymer melts as well as for modelling physical and chemical interactions of these coatings during cutting and forming applications. The overall coating composition is hence not representative to describe coating-polymer melt interactions. Instead of the overall coating composition the surface near region composition is relevant. These findings underline the importance of surface-sensitive analysis methods when designing protective coatings for application.

Acknowledgments

The authors gratefully acknowledge the financial support of the German Research Foundation (DFG) within the transregional collaborative research centre TRR 87/1-2010 'Pulsed high power plasmas for the synthesis of nanostructured functional layers' (SFB-TR 87). Furthermore, the authors thank Daniel Briesenick from the Coating Materials & Polymers department (Professor Dr W Bremser) at University of Paderborn for SEM measurements.

References

[1] Münz W D 1986 Titanium aluminum nitride films—a new alternative to tin coatings *J. Vac. Sci. Techno.* A **4** 2717–25
[2] McIntyre D *et al* 1990 Oxidation of metastable single-phase polycrystalline $Ti_{0.5}Al_{0.5}N$ films—kinetics and mechanisms *J. Appl. Phys.* **67** 1542–53
[3] Kawata K, Sugimura H and Takai O 2001 Characterization of multilayer films of Ti–Al–O–C–N system prepared by pulsed d.c. plasma-enhanced chemical vapor deposition *Thin Solid Films* **390** 64–9
[4] Bobzin K *et al* 2007 PVD—coatings in injection molding machines for processing optical polymers *Plasma Process. Polym.* **4** S144–9
[5] Michaeli W *et al* 2006 PVD-coated plastification screws *Kunststoffe* **8** 66–8
[6] Music D *et al* 2012 Polypropylene-MAlN (M = Ti, Cr) interface interactions *Surf. Sci.* **606** 986–9
[7] Reeswinkel T, Music D and Schneider J M 2009 *Ab initio* calculations of the structure and mechanical properties of vanadium oxides *J. Phys.: Condens. Matter* **21** 145404
[8] Ratzsch M *et al* 2002 Radical reactions on polypropylene in the solid state *Prog. Polym. Sci.* **27** 1195–282
[9] Sohma J 1992 Mechanoradical formation in polypropylene by an extruder action and its after-effects *Colloid Polym. Sci.* **270** 1060–5
[10] Schneider J M *et al* 1999 Hydrogen uptake in alumina thin films synthesized from an aluminum plasma stream in an oxygen ambient *Appl. Phys. Lett.* **74** 200–2
[11] Schneider J M, Anders A and Yushkov G Y 2001 Magnetic-field-dependent plasma composition of a pulsed aluminum arc in an oxygen ambient *Appl. Phys. Lett.* **78** 150–2
[12] Schneider J M *et al* 2000 Magnetic-field-dependent plasma composition of a pulsed arc in a high-vacuum ambient *Appl. Phys. Lett.* **76** 1531–3
[13] Rosén J *et al* 2006 Reducing the impurity incorporation from residual gas by ion bombardment during high vacuum magnetron sputtering *Appl. Phys. Lett.* **88** 191905
[14] Rosen J, Larsson K and Schneider J M 2005 *Ab initio* molecular dynamics study of hydrogen removal by ion–surface interactions *J. Phys.: Condens. Matter* **17** L137–42
[15] Tempez A, Bensaoula A and Schultz A 2002 Characterization of TiAlN thin film annealed under O-2 by *in situ* time of flight direct recoil spectroscopy/mass spectroscopy of recoiled ions and *ex situ* *x*-ray photoelectron spectroscopy *J. Vac. Sci. Technol.* A **20** 1320–6
[16] Kouznetsov V *et al* 1999 A novel pulsed magnetron sputter technique utilizing very high target power densities *Surf. Coat. Technol.* **122** 290–3
[17] Sarakinos K, Alami J and Konstantinidis S 2010 High power pulsed magnetron sputtering: a review on scientific and engineering state of the art *Surf. Coat. Technol.* **204** 1661–84
[18] Reeswinkel T *et al* 2011 Structure and mechanical properties of TiAlN-WN*I*x thin films *Surf. Coat. Technol.* **205** 4821–7
[19] Seah M P and Dench W A 1979 Quantitative electron spectroscopy of surfaces: a standard data base for electron inelastic mean free paths in solids *Surf. Interface Anal.* **1** 2–11
[20] Drüsedau T P, Neubert T and Panckow A N 2003 The properties of aluminum oxide and nitride films prepared by d.c. sputter-deposition from metallic targets *Surf. Coat. Technol.* **163–164** 164–8
[21] Wuttig M *et al* 2006 Towards understanding the superior properties of transition metal oxynitrides prepared by reactive DC magnetron sputtering *Thin Solid Films* **502** 228–34
[22] Adibi F *et al* 1991 Defect structure and phase-transitions in epitaxial metastable cubic $Ti_{0.5}Al_{0.5}N$ alloys grown on MGO(001) by ultra-high-vacuum magnetron sputter deposition *J. Appl. Phys.* **69** 6437–50
[23] Mayrhofer P H *et al* 2003 Self-organized nanostructures in the Ti–Al–N system *Appl. Phys. Lett.* **83** 2049–51
[24] Johnson L J S *et al* 2012 Spinodal decomposition of Ti0.33Al0.67N thin films studied by atom probe tomography *Thin Solid Films* **520** 4362–8
[25] Rachbauer R *et al* 2009 Three-dimensional atom probe investigations of Ti–Al–N thin films *Scr. Mater.* **61** 725–8
[26] Sjölen J *et al* 2007 Structure and mechanical properties of arc evaporated Ti–Al–O–N thin films *Surf. Coat. Technol.* **201** 6392–403

3.2 Surface Chemistry of PVD (Cr,Al)N coatings deposited by means of Direct Current and High Power Pulsed Magnetron Sputtering

Christian Kunze, Ricardo H. Brugnara, Nazlim Bagcivan, Kirsten Bobzin, Guido Grundmeier
Surface and Interface Analysis, 45, **2013**, 1884-1892.

The scientific work and discussion was coordinated and consolidated by CK under supervision of GG.
The manuscript was prepared by CK; RHB contributed to the introduction of the manuscript.
Hard coatings were deposited by RHB.
EDX and GDOES measurements and data evaluation were performed by RHB.
XPS and AFM measurements and data evaluation were performed by CK.
The manuscript was revised by GG, NB and KB.

Within this paper the surface chemistry of CrAlN hard coatings has been investigated comparing DC-MS and HPPMS deposition processes. It could be shown that the surface near region of the investigated coatings is enriched with oxygen in comparison to the bulk composition along with an enrichment of aluminum in the surface near region. Both, DC and HPPMS coatings, showed a non-stoichiometric chemical composition with a significant excess of cations (chromium and aluminum) in the bulk structure. The variation of the pulse length of the HPPMS process had a strong influence on the resulting composition of the surface near region mainly influencing the observed anion/cation stoichiometry. Here a significantly increased incorporation of nitrogen could be observed for short HPPMS pulse lengths. Based on these results an increased knowledge towards tailored surface compositions of CrAlN coatings could be gained.

Research article

SURFACE and INTERFACE ANALYSIS

Received: 25 May 2013 Revised: 18 September 2013 Accepted: 20 September 2013 Published online in Wiley Online Library: 17 October 2013

(wileyonlinelibrary.com) DOI 10.1002/sia.5336

Surface chemistry of PVD (Cr,Al)N coatings deposited by means of direct current and high power pulsed magnetron sputtering

Christian Kunze,[a] Ricardo H. Brugnara,[b] Nazlim Bagcivan,[b] Kirsten Bobzin[b] and Guido Grundmeier[a]*

(Cr,Al)N protective coatings were deposited using direct current (DC) and high power pulse magnetron sputtering (HPPMS) technology. The chemical analysis of the surface near region of the coatings was performed by means of X-ray photoelectron spectroscopy (XPS) and was correlated to the deposition parameters and resulting coating morphology. A surface oxidation process was observed by means of angle resolved XPS studies and XPS sputter profiles. Both DC and HPPMS coatings showed a non-stoichiometric chemical composition with a significant excess of cations (chromium and aluminum) in the bulk structure, leading to a metastable phase. The passivation reaction of the surface near region leads to an anion to metal ratio which goes along with an enrichment of aluminum in the surface near region as a thermodynamically favored composition in equilibrium with the ambient atmosphere. Interestingly, the variation of the pulse duration of the HPPMS process, which led to a change of the peak current, had a strong influence on the resulting composition of the surface near region. Copyright © 2013 John Wiley & Sons, Ltd.

Additional supporting information may be found in the online version of this article at the publisher's web site.

Keywords: (Cr,Al)N; protective coating; surface near region; XPS; HPPMS; HiPIMS

Introduction

Injection moulding is a commonly used manufacturing process for the fabrication of complex plastic parts. During plastic processing, abrasion and adhesion wear as well as corrosion take place on the surfaces of moulding tools. In order to improve these tools, hard coatings deposited via physical vapor deposition (PVD) have been developed as protective coatings. It was demonstrated that the adhesion of plastics melt can be reduced by using, e.g. TiN, TiAlN, TiAlON, CrN, CrAlN and CrAlON coatings.[1–3]

In order to analyse the adhesion mechanisms between polymers and hard coatings, the interface between polypropylene (PP) and MAlN and MAlNO (M = Ti, Cr) was recently studied by Music *et al.* using ab initio calculations.[4] It was reported that the work of separation between PP and defect-free $M_{0.5}Al_{0.5}N$ and $M_{0.5}Al_{0.5}N_{0.5}O_{0.5}$ surfaces is very small.[5] Calculations showed that radicals, that may be formed, e.g. during shearing of the PP melt,[6,7] increase the work of separation by two orders of magnitude.[4] Under technical conditions, after the deposition process, the coating is exposed to atmosphere of high oxygen and water partial pressure, which can lead to an alteration of the reactive surface near region possibly due to the high sticking coefficient of oxygen, hydrogen and water.[8] Angle resolved X-ray photoelectron spectroscopy (AR-XPS) measurements were reported for amorphous TiAlN coatings showing that the surface near region was partially oxidized and enriched with Al.[9] Gnoth *et al.* have recently investigated the surface chemistry of as-deposited TiAlN.[10] It was reported that the TiAlN coating deposited under high vacuum shows several nanometer thick oxidized surface after the deposition process.[10] To the best knowledge of the of the authors, no information about the chemical composition of the surface near region and gradients therein were reported to date for crystalline (Cr,Al)N deposited by direct current (DC) and high power pulse magnetron sputtering (HPPMS). Therefore, the goal of this work was the investigation of the surface near composition of (Cr,Al)N in order to contribute towards the understanding surface phenomena, such as the mechanisms leading to low adhesion between polymers and (Cr,Al)N coatings. Moreover, information about the chemical composition of surface near region composition data is important for generation of realistic models describing the interaction between the coating surface and material to be processed.

(Cr,Al)N coatings were deposited by DC and HPPMS process with different pulse durations (40, 80 and 200 μs). The resulting microstructure and chemical composition were analyzed by atomic force microscope (AFM), energy dispersive X-ray spectroscopy (EDX) and glow discharge optical emission spectroscopy (GDOES), respectively. To study the composition of the surface near region and gradients therein, AR-XPS was used. AR-XPS is highly surface sensitive and allows the determination of the chemical composition and chemical states. Experiments at varying take-off angles allowed for the analysis of chemical composition gradients on the nanometer scale.

* *Correspondence to: G. Grundmeier, Technical and Macromolecular Chemistry, University of Paderborn, Warburger Str. 100, 33098 Paderborn, Germany. E-mail: g.grundmeier@tc.uni-paderborn.de*

a *Technical and Macromolecular Chemistry, University of Paderborn, Warburger Str. 100, 33098, Paderborn, Germany*

b *Surface Engineering Institute, RWTH Aachen University, Kackertstr. 15, 52072, Aachen, Germany*

SURFACE and INTERFACE ANALYSIS

Experimental

Materials and chemicals

All chemicals were used without further purification. Isopropanol, tetrahydrofuran and ethanol for cleaning purposes were purchased in p.a. grade from VWR International, Germany. Silicon wafers of orientation Si(100), (p-doped with boron, single-side polished) were purchased from Si-Mat, Kaufering, Germany. For GDOES experiments, cemented carbide substrates (THM12) from WIDIA (Germany) with a size of $12.7 \times 12.7\ mm^2$ and a thickness of 4.76 mm were used.

All surfaces were cleaned with organic solvents before analysis. The samples were sonicated in tetrahydrofuran, isopropanol and ethanol for 15 min each and rinsed with clean solvent before the next cleaning step. After rinsing with pure ethanol, the samples were dried in a flow of pure nitrogen gas.

Deposition parameters

The coatings were deposited on silicon wafer (100) and on cemented carbide (THM12) via an industrial CC800/9 coating unit (CemeCon AG, Germany), equipped with one HPPMS power supply and one DC source, which were operated at constant mean power of 5 kW. A Cr target ($500 \times 80\ mm^2$) with 20 Al plugs (15 mm diameter) with a purity of 99.9% for Cr and 99.5% for Al was applied for the deposition of the coatings. The bias voltage was set to −100 V. HPPMS (Cr,Al)N coatings were deposited using different pulse durations (40, 80 and 200 µs) at constant frequency of 500 Hz and constant mean power (5 kW). The recorded voltage and current waveforms of the HPPMS process for 200 µs and 40 µs can be found in the Supplementary Material. By reducing the pulse duration, the cathode peak current increases from 260 A at 200 µs, to 280 A at 80 µs and to 660 A at 40 µs in order to keep the same mean power. Higher peak currents can be associated with an increased plasma ionization rate.[11,12] Therefore, it can be expected that the ionization rate of the metal and reactive gas atoms is dramatically increased at reduced pulse durations.[13] All (Cr,Al)N coatings were synthesized in an Ar/Kr/N_2 atmosphere at total pressure of 0.45 Pa. The Ar and Kr flows were kept constant at 120 sccm and 80 sccm, respectively. The N_2 flow rate was pressure-controlled in order to keep the chamber pressure at 0.45 Pa. All coatings were deposited for 120 min. The summarized deposition parameters are presented in Table 1.

Analytical methods

EDX Analysis of chemical composition of the bulk of the coating was carried out in a scanning electron microscope (SEM) of type DSM 982 Gemini (Zeiss, Germany) with an EDX detector.

GDOES The bulk composition of the coatings was analyzed by glow discharge optical emission spectroscopy (GDOES) in RF mode as a function of etching time. A GDOES Profiler type JY 5000 RF (Horiba, Japan) equipped with an anode of 4 mm was used.

AFM AFM topography imaging was performed by means of a Nanowizard II Ultra (JPK, Germany) system in contact mode with a constant force of about 5 nN. Cantilevers of type CSC-17 AIBS (Mikromash) with a resonance frequency of 12 kHz and a force constant of 0.15 N/m were used.

XPS Angle resolved XPS (AR-XPS) measurements were performed by means of an Omicron ESCA + System (Omicron NanoTechnology GmbH, Germany) with a base pressure of $< 3 \cdot 10^{-7}$ Pa. The system is equipped with a hemispherical energy analyzer; the element spectra were recorded at pass energies of 25 eV. For photoelectron excitation, a monochromated Al-Kα (1486.7 eV) X-ray source with a spot diameter of 600 µm was used. The take-off angle of the detected photoelectrons was varied from 30° to 80° with respect to the surface normal. The native carbon contamination on the surface which forms upon contact with the ambient atmosphere and mainly consists of low weight (hydro-)carbon species was removed by mild Ar sputtering at 350 eV for 180 s prior to the XPS measurements, which resulted in a residual carbon concentration of typically below 5 at.-%. The calibration of the spectra was performed using the remaining C 1s peak (binding energy, BE = 285.0 eV) as an internal reference. For data evaluation, the CasaXPS software (version 2.3.15) was used. All quantification of the XPS data was performed by integration of the peaks with regard to the relative sensitivity factors of the elements. As the core level energy of Al 2p overlaps with Cr 3s, the Al 2s peak was used for the evaluation of the Al content.

The typical attenuation length λ of the photo electrons in a solid can be estimated based on a square root law as a function of the kinetic energy[14] which leads to values of $\lambda = 1.6$ to 2.0 nm in the observed energy range between Cr 2p, O 1s, N 1s and Al 2s for excitation with an Al-K_α X-ray source at 1486.7 eV. The probing depth d is usually referred as 3λ and can be calculated from geometric considerations as a cosine-dependent function of the take-off angle Θ[15] according to Table 2:

$$d = 3\lambda \cos\Theta \quad (1)$$

Table 2. Probing depth as a function of the XPS take-off angle[14,15]

Take-off angle to surface normal Θ/degrees	Probing depth/ nm Cr 2p	O 1s	N 1s	Al 2s
30	4.2	4.3	4.6	5.2
60	2.4	2.5	2.7	3.0
80	0.8	0.9	0.9	1.0

Table 1. Deposition parameters of the investigated (Cr,Al)N coatings

Sample no.	Ar flow/sccm	Kr flow/sccm	N_2 flow/sccm	Pulse parameters/µs/Hz/kW	Process	Target
1	120	80	37	40, 500, 5	HPPMS	CrAl20
2	120	80	41	80, 500, 5	HPPMS	CrAl20
3	120	80	43	200, 500, 5	HPPMS	CrAl20
4	120	80	52	–, –, 5	DC	CrAl20

SURFACE and INTERFACE ANALYSIS

These considerations lead to specific information depths for each element and take-off angle of the photoelectrons and are only valid under the assumption of a homogeneous distribution of the elements within the probed surface layer. However, as the aim of this work focuses on the investigation of gradients in compositions within the surface near region, all following data will be presented without a detailed discussion of the element-dependent information depth.

To investigate the composition of the coatings towards the bulk structure of the coating, depth profiling experiments were performed by means of argon sputtering. The acceleration voltage of the Ar ions was set to 2 keV, the etching time was 30 s per sputter cycle. As the exact sputter rate of the (Cr,Al)N coatings was not calibrated, the results will be discussed qualitatively. For comparison, the sputter rate calibrated on SiO_2 is about 4 nm/min under the same operating conditions.

Results and discussion

Coating microstructure

The investigated (Cr,Al)N coatings had a thickness of 0.8 μm (40 μs), 1.3 μm (80 μs), 1.5 μm (200 μs) and 3.1 μm (DC). SEM images of the cross sections which were used for determining the coating thickness can be found in the Supplementary Material. The surface microstructure of the coatings was investigated by contact mode AFM imaging as presented in Fig. 1. The RMS roughness of the samples was determined from $2 \times 2\ \mu m^2$ scans by the JPK Data Processing Software (version 4.2.53). The coating deposited by the DC process (sample 4) showed a significantly higher roughness compared to all HPPMS coatings. The corresponding roughness values are presented in Table 3. For the HPPMS samples, the surface roughness decreased with decreasing pulse duration. By means of the AFM and SEM micrographs can be considered that the DC coating and the HPPMS coating deposited at 200 μs present columnar a microstructure, while the other coatings (80 and 40 μs) show a finer and compacter microstructure. The lowest roughness was achieved for the coatings deposited at 40 μs and 80 μs. This finding can be attributed to the increased metal ion flux, which leads to an increased ad-atom mobility and a smoother surface and finer microstructure.[16–18]

Table 3. Surface roughness of the investigated (Cr,Al)N coatings as determined by AFM topography imaging

Sample number	HPPMS pulse duration	RMS roughness/nm
1	40 μs	1.8
2	80 μs	2.0
3	200 μs	5.9
4	DC	17.8

EDX analysis

The coating composition obtained by means of EDX analysis is presented in Table 4. As quantitative analysis by means of EDX is not reliable for light elements such as nitrogen, these results can only be discussed qualitatively. For all coatings, no oxygen could be detected. Sample 4, which was deposited by DC-MS, showed an increased chromium/aluminum ratio in comparison to the HPPMS coatings which could be explained by a significantly higher sputter rate of aluminum in the HPPMS process compared to DC-MS.[19]

GDOES profiling

GDOES profiles of the investigated (Cr,Al)N coatings deposited on cemented carbide substrate are presented in Fig. 2 as a function of the etching time. All profiles were plotted after stabilization of the RF plasma in the GDOES unit. The transition point where tungsten is the only detected element can be assigned to the underlying substrate, as the concentration of carbon is not presented in the GDOES profiles. Based on the thickness of the

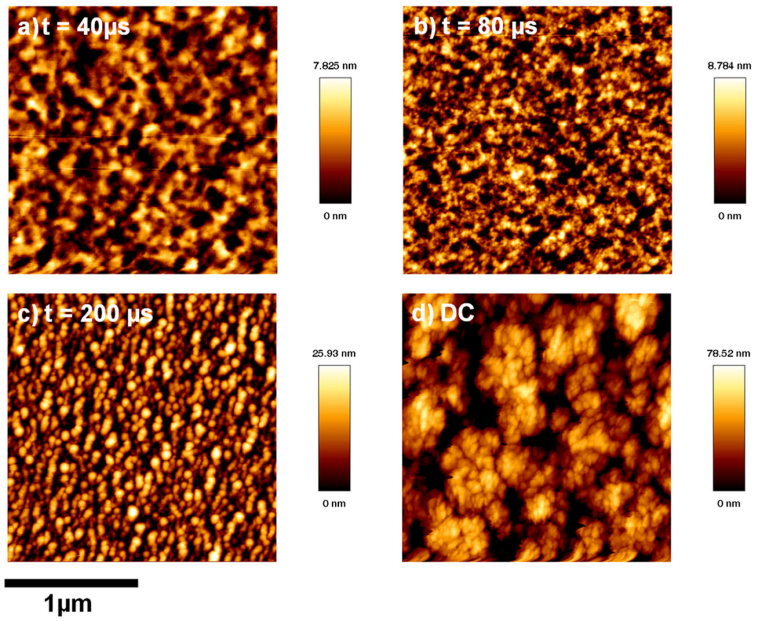

Figure 1. AFM topography images of the investigated coatings: a) sample 1 ($t = 40$ μs), b) sample 2 ($t = 80$ μs), c) sample 3 ($t = 200$ μs), c) sample 4 (DC).

SURFACE and INTERFACE ANALYSIS

Table 4. Composition of the investigated (Cr,Al)N coatings as determined by EDX measurements

Sample no., pulse duration	Cr/at.-%	Al/at.-%	N/at.-%
1, 40 µs	46	17	37
2, 80 µs	56	17	27
3, 200 µs	59	16	26
4, DC	66	10	24

(Cr,Al)N coatings as determined from SEM cross section images, the sputter rate can be estimated to about 4.2 µm/min for all samples. The finding that the HPPMS process leads to a higher Al content in the coating compared to DC-MS can be confirmed by the GDOES data. Additionally, an increased incorporation of nitrogen could be observed especially for the HPPMS coating deposited at a pulse duration of 40 µs. This finding could be explained by the high concentration of energetic N^+ and N^{2+} ions in the plasma during the HPPMS discharge at an increased peak current.[13,20] Furthermore, the increased incorporation of nitrogen into the (Cr,Al)N phase is predominantly influenced by the short HPPMS pulse duration and not by an increased partial pressure of nitrogen in the deposition chamber, as the nitrogen partial pressure was even decreased during the deposition process for short HPPMS pulse durations (see Table 1), which can be also explained by the higher grade of nitrogen ionization as discussed before.

XPS analysis

The chemical composition was analyzed by means of AR-XPS to compare the composition of the surface near region to the bulk composition of the coatings deposited under different sputter parameters.

Beside the elements of the sputter targets – chromium and aluminum – and nitrogen as a reactive gas during the plasma deposition, significant amounts of oxygen were detected in the XPS spectra. Additionally, residual amounts of adsorbed carbon species (about 1 to 5 at.-%) were observed for all samples after Ar sputter cleaning at 350 eV for 180 s. For shorter HPPMS pulse durations, the survey spectra indicated a decrease of the O/N ratio in the surface near region of the coatings. Especially, a pulse duration of 40 µs leads to a significantly lower oxygen concentration.

AR-XPS analysis of the surface near region

The chemical compositions of the surface near regions of the investigated coatings as measured by means of XPS and EDX are presented in Fig. 3. A significant enrichment of oxygen in the surface near region of all studied coatings could be derived from the AR-XPS data. Additionally, the XPS results confirmed the decrease of the O/N-ratio in the surface near region deposited with short HPPMS pulse duration (40 µs). Furthermore, the coating deposited by means of the DC plasma process (sample 4) resulted in a strongly increased Cr/Al ratio, which is in good agreement with previous results due to an increased sputter rate of Al in the HPPMS process.[19]

A comparison of some important ratios of elements as derived from the quantification of the XPS spectra is given in Table 5. For the coatings deposited by means of the HPPMS process, a similar trend was observed. The O/N ratio increases close to the surface as the incorporation of oxygen and surface oxidation is thermodynamically favored. Moreover, the Cr/Al ratio is decreased close to the surface which hints to a preferential oxidation of aluminum. A similar result was observed in a recent study by Gnoth *et al.* for TiAlN(O) coatings.[10] This observation can be explained by the thermodynamically favored formation of aluminum oxide in comparison with chromium oxide formation taking into account the

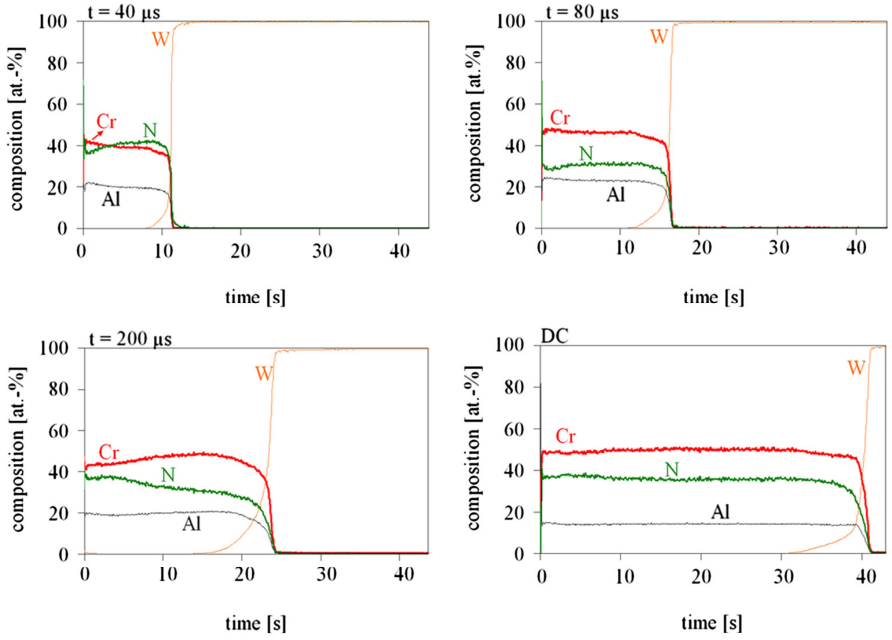

Figure 2. GDOES depth profile of the investigated (Cr,Al)N coatings deposited on cemented carbide substrates. The sputter rate can be estimated to about 4.2 µm/min.

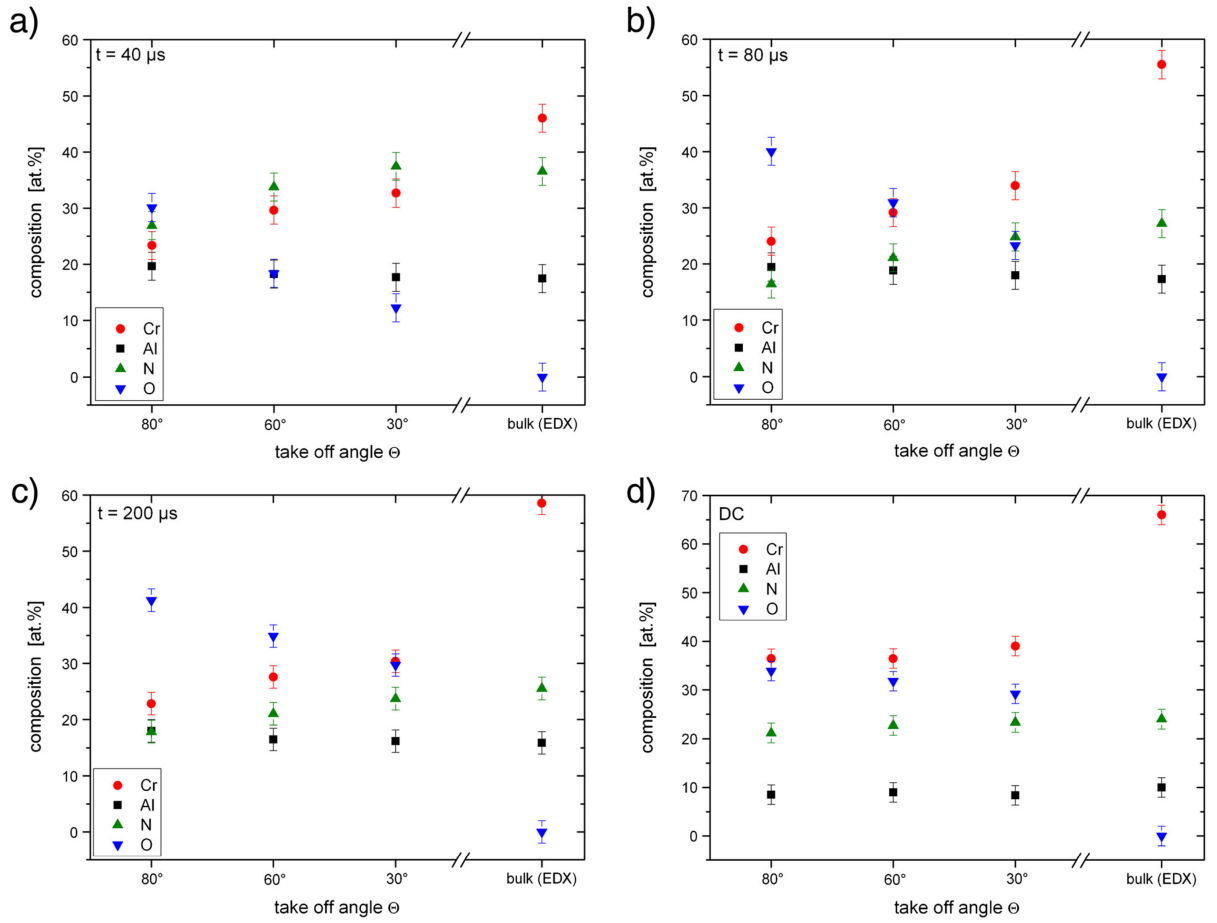

Figure 3. a) – d): Compositions of the surface near region as measured by AR-XPS and EDX for samples deposited at different HPPMS pulse durations and in the DC process.

Table 5. Atomic ratios calculated from AR-XPS composition data. The calculated element ratios include an estimated error of 4%

	$t = 40\ \mu s$			$t = 80\ \mu s$		
AR-XPS	30°	60°	80°	30°	60°	80°
O/N	0.33	0.55	1.12	0.94	1.46	2.44
Cr/Al	1.85	1.62	1.19	1.89	1.54	1.24
O/(Cr + Al)	0.24	0.38	0.70	0.45	0.64	0.92
N/(Cr + Al)	0.74	0.70	0.63	0.48	0.44	0.38
	$t = 200\ \mu s$			DC		
AR-XPS	30°	60°	80°	30°	60°	80°
O/N	1.25	1.66	2.31	1.25	1.40	1.60
Cr/Al	1.87	1.67	1.27	4.65	4.05	4.28
O/(Cr + Al)	0.64	0.79	1.01	0.62	0.70	0.75
N/(Cr + Al)	0.51	0.48	0.44	0.49	0.50	0.47

standard enthalpies of formation of Al_2O_3 ($\Delta H_f^0 = -1677$ kJ/mol) and Cr_2O_3 ($\Delta H_f^0 = -1140$ kJ/mol).[21] The coating deposited by means of the DC plasma process (sample 4) did not show a significant change in the composition at the surface near region. This could be explained by the high surface roughness of the DC-MS coating in comparison with the HPPMS coatings (see Fig. 1 and Table 3) which decreases the surface sensitivity of the angle resolved XPS experiments.

Physisorbed surface contaminations were removed by gentle Ar sputtering prior to the XPS experiments. Thus, the measured

concentrations of oxygen in the surface near region can be assigned to the formation of a surface oxide layer on (Cr,Al)N. As we are discussing a probable application of (Cr,Al)N systems as protective coatings for polymer processing, the composition of the oxidized surface near region of the (Cr,Al)N coatings has to be investigated in detail, as it determines the interaction with the polymer melt. The increase of oxygen concentration towards the outer surface indicates that an oxidation process of the (Cr,Al)N coating occurs after the completion of the deposition process. However, oxygen chemisorption within the deposition chamber after the deposition process and surface oxidation upon atmospheric exposure after venting the deposition chamber cannot be separated based on the *ex-situ* analysis performed in this work. It is likely that the oxygen partial pressure in the sputter chamber during and after the deposition process is enough for an initial surface oxygen chemisorption on the hot coating right after the sputter process even at low process pressures of 0.45 Pa.[10]

A significantly decreased O/N ratio was observed for sample 1 which was deposited with the shortest HPPMS pulse duration (40 µs) as presented in Fig. 4. The higher stability observed for sample 1 towards the post oxidation reaction could be explained either with the changes in the morphology or with the differences in the chemical composition of the coating based on the plasma parameters. The smoother surface (see Fig. 1 and Table 3) and more compact morphology lead to a reduction in the surface area and porosity of the surface near region. Thus, the interface for the oxidation reaction with oxygen is decreased which leads to a lower incorporation of oxygen. To investigate the composition of the samples towards the bulk structure complementary, Ar-sputtering profiles were measured and presented in the following section.

The element spectra of chromium (Cr 2p) show noticeable differences in peak shape and width as a function of the deposition parameters as exemplarily presented in Fig. 5. A comparison with the literature shows that a correct interpretation of the Cr 2p core level peak is not straight forward. For CrN substrates, Lippitz *et al.* used four contributions to fit the Cr $2p_{3/2}$ peak: Cr^0 at 574.0 eV, chromium nitride at 575.5 eV and two chromium oxide species at 576.9 eV and 578.2 eV,[22] while Kaciulis *et al.*[23] assumed two components at 574.6 eV for chromium nitride and 576.8 eV for

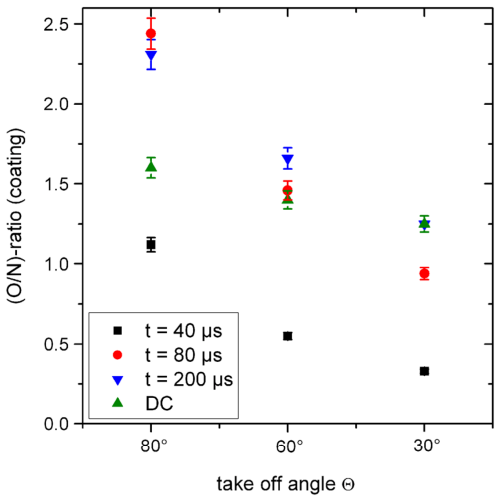

Figure 4. (O/N)-ratio in the investigated coatings as a function of the deposition parameters. As no oxygen could be detected in the EDX experiments, only the results of the XPS measurements are presented here.

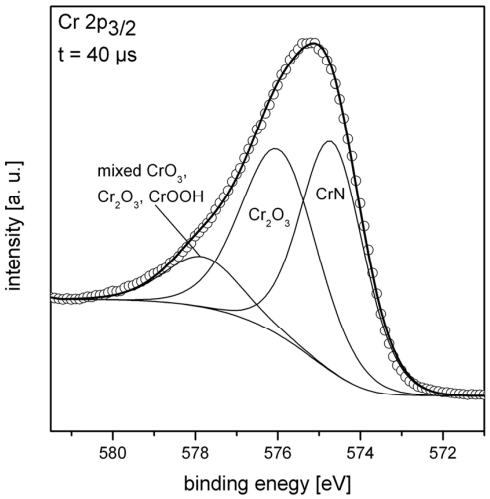

Figure 5. Cr $2p_{3/2}$ detail spectrum for sample 1 ($t = 40$ µs) at 60° take-off angle. Synthetic components of CrN, Cr_2O_3 and mixed CrO_3/Cr_2O_3/CrOOH contributions are fitted.

chromium oxide. Highly resolved XPS data of chromium oxide samples suggest that even more compounds are necessary to achieve a satisfying fit of chromium oxide species as shown by Ünveren *et al.*[24] and Biesinger *et al.*.[25] For the Cr 2p spectra measured within this work, a satisfying fit could be achieved with three components for the Cr $2p_{3/2}$ peak, as shown for sample 1 ($t = 40$ µs) in Fig. 5. The fitted peaks assign the contributions to CrN at 574.7 eV, Cr_2O_3 at 576.1 eV and a contribution at 577.9 eV that is usually assigned to higher oxidation states of Cr(VI).[26] According to Biesinger *et al.*[25], also mixed contributions of Cr_2O_3 and CrOOH cover a broad energy range in this region. As the composition of the passive oxide film is quite complex, we cannot distinguish these contributions based on the measured XPS data. However, the components fitting the Cr $2p_{3/2}$ spectra can be at least discussed qualitatively in terms of nitridic and oxidic contributions as shown for all samples in Table 6. Additionally the full width half maximum (FWHM) values of the Cr $2p_{3/2}$ peaks are presented. A trend of smaller FWHM values with a decreased amount of oxidic chromium species could be observed for the samples deposited with short HPPMS pulse durations, indicating that chromium exists in rather one oxidation state. This finding supports the predominant existence of CrN along with a significantly decreased contribution of Cr_2O_3 species, which leads to the conclusion that the incorporation of nitridic species into the deposited film is favored with short HPPMS pulse durations.

The Al 2s spectra did not show a significant peak shift as the Al–O and Al–N bonds are very similar in energy.[27] However, due to the concurrently increasing intensity of Al and O with decreasing probing depth and the previously discussed enthalpies of formation, it is reasonable to assume that aluminum preferably binds to oxygen.

Sputter depth profiling

For the HPPMS coatings with a rather smooth morphology, sputter depth profiles were measured by means of XPS. Prior to sputter depth profiling, the composition of the surface near region was in good agreement with the angle resolved XPS data presented above. For an insight towards the bulk composition of the coatings and a rough estimation of the passive layer thickness,

SURFACE and INTERFACE ANALYSIS

Table 6. Relative peak areas of the Cr $2p_{3/2}$ components and FWHM values measured at 60° take-off angle

Sample no., Pulse duration	CrN/relative area	Cr_2O_3/relative area	Mixed CrO_3, Cr_2O_3, CrOOH/relative area	FWHM Cr $2p_{3/2}$/eV
1, 40 µs	0.45	0.43	0.12	2.9
2, 80 µs	0.45	0.42	0.13	3.2
3, 200 µs	0.40	0.43	0.17	3.7
4, DC	0.43	0.41	0.16	3.7

depth profiles were acquired by means of Ar sputtering. Within this work, two comparative depth profiles for sample 1 ($t = 40$ µs) and sample 3 ($t = 200$ µs) are presented for the comparison of the strongest variation of process parameters within the HPPMS coatings. The corresponding sputter profiles are presented in Fig. 6 ($t = 40$ µs) and Fig. 7 ($t = 200$ µs). After each sputter cycle of 30 s, the coating composition was determined by means of XPS at 60° take-off angle. As the exact sputter rate of (Cr,Al)N under the applied conditions is unknown, the results can only be discussed qualitatively. Nevertheless, these findings are helpful to compare both coatings in terms of chemical composition and oxide layer thickness. The depth profile which was obtained for sample 1 ($t = 40$ µs) is presented in Fig. 6. The decreasing concentration of oxygen with increasing sputter etching time is in agreement with the previous results that oxygen incorporation is strongly increased in the surface near region. A small concentration of oxygen in the range of 4 – 5 at.-% was observed in the bulk region. This small amount of oxygen probably results from residual oxygen and/or adsorbed water within the deposition chamber. Furthermore, the concentration of nitrogen and chromium is decreased in the surface near region which hints to an additional incorporation of oxygen – probably on interstitial lattice positions – into the (Cr,Al)N matrix. Almost no depth dependency of the aluminum concentration was observed. Hence, a relative enrichment of aluminum in the surface near region – as an additional element (oxygen) is present – can be concluded. This result supports the previous results obtained by means of angle resolved XPS indicating the preferential formation of Al_2O_3 as the most thermodynamically stable species within the oxidation process.

The depth profile of sample 3 ($t = 200$ µs) is presented in Fig. 7. Although the concentrations of all elements follow the same trends as observed for sample 1 ($t = 40$ µs), significant differences in the bulk composition at long sputter times were observed. A strongly increased concentration of chromium and a significantly decreased concentration of nitrogen were observed for sample 3 ($t = 200$ µs). As these effects cannot be explained by the oxidation reaction of the surface near region, the different composition of the deposited coating could be explained with the change in the HPPMS plasma parameters.

The observed composition of the region below the passivation layer as determined by means of XPS sputter depth profiling is in good agreement with the EDX and GDOES data presented in previous sections. Regarding the stoichiometry of the (Cr,Al)N phase, both bulk structures show a significant excess of cations (chrome and aluminum) in comparison to the anionic lattice of nitrides. As no metallic Cr^0 and Al^0 contributions are expected, this result points towards a metastable, non-stoichiometric composition of the deposited coatings. To Baben *et al.* addressed the nitrogen over- or understoichiometry in TiAlN films to metal vacancies or nitrogen vacancies, based on ab initio calculations.[28] This finding is even more distinctive for sample 3 ($t = 200$ µs) due to its increased Cr/Al ratio and decreased concentration of nitrogen in comparison to sample 1 ($t = 40$ µs). This result supports the

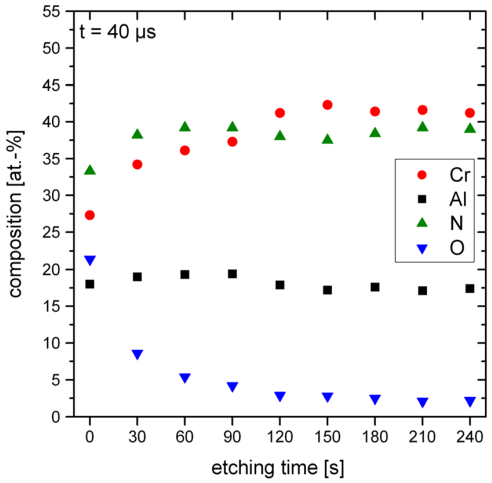

Figure 6. Depth profile for sample 1 ($t = 40$ µs) during Ar sputtering at 2 keV as a function of etching time. (The sputter rate can be estimated based on calibration experiments leading to 4 nm/min for SiO_2.).

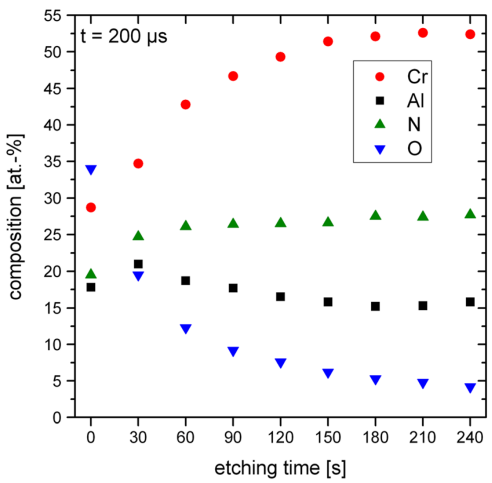

Figure 7. Depth profile for sample 3 ($t = 200$ µs) during Ar sputtering at 2 keV as a function of etching time. (The sputter rate can be estimated based on calibration experiments leading to 4 nm/min for SiO_2.).

SURFACE and INTERFACE ANALYSIS

assumption of a thinner passive layer in the case of sample 1 ($t = 40\ \mu s$), as concluded from the depth profiles. For sample 1 ($t = 40\ \mu s$) and 3 ($t = 200\ \mu s$), no significant changes in composition were observed after 120 s and about 210 s of etching times, respectively. A rough estimation of the sputter rate based on SiO_2 (sputter rate 4 nm/min) was performed which leads to a thickness estimation of the passive layer of about 8 nm in case of sample 1 ($t = 40\ \mu s$), and about 14 nm in case of coating sample 3 ($t = 200\ \mu s$). The finding of a thicker passive layer along with the incorporation of oxygen into the coating explains the strong depletion of chromium in the surface near region of sample 3 ($t = 200\ \mu s$). The combined results of bulk analysis and the angle resolved XPS data lead to the conclusion that two effects could have an influence on the thickness and chemical composition of the passive layer of the investigated (Cr,Al)N coatings: First, the stoichiometric composition, including the ratio of anions and cations in the coating itself and second the morphology and nanostructure of the coating. In the case of sample 1 ($t = 40\ \mu s$), the smoother coating leads to a decreased surface area along with a detained reaction with oxygen under ambient conditions during the passivation reaction.

Conclusions

The process parameters during DC sputtering and HPPMS deposition of (Cr,Al)N coatings could be correlated with the chemical composition of the surface near region. XPS sputter depth profiling and GDOES analysis were performed to analyze the coating composition within and below the surface near region.

It was shown that by a variation of the HPPMS pulse parameters the peak current was changed and thus the composition of the coating could be influenced in terms of volume microstructure and composition, which has an impact on the passivation reaction of the surface near region after the coating deposition upon contact with ambient atmosphere.

As measured by means of EDX and XPS depth profiling, all investigated coatings showed a non-stoichiometric chemical composition with a significant excess of cations (chromium and aluminum) in the bulk phase, indicating the presence of a metastable phase, that probably can be assigned to anion vacancies in the (Cr,Al)N crystal structure.

XPS analysis showed that independent of the process parameters all investigated coatings were covered with a several nanometer thick oxidized surface near region, which, however, differed in composition. By means of AR-XPS, it could be shown that the oxygen content increases towards the outer surface of the passive film and reaches levels up to 40 to 60 at.-%. The main oxidation reaction is most likely due to the chemisorption of oxygen as part of the residual gas in the deposition chamber immediately after deposition during the cooling phase.

Interestingly, the increased incorporation of nitrogen into the (Cr,Al)N phase is predominantly triggered by the short HPPMS pulse duration and not by an increased partial pressure of nitrogen in the deposition chamber. This finding can be explained by the higher grade of ionization of nitrogen due to a high peak current at short pulse durations. By reducing the pulse duration, the cathode peak current increases to keep the same mean power. Higher peak currents can be associated with an increased plasma ionization rate that influences the composition of the deposited material.

The passivation reaction of the surface near region is based on the incorporation of additional oxygen anions leading to an approximation of the ideal stoichiometric composition of the oxidized surface layer. However, an increased incorporation of nitrogen anions during the deposition process at short pulse durations led to coatings which were less sensitive to oxidation of the surface near region with a more compact coating microstructure and a smoother surface.

The comparison of the DC and HPPMS deposition process leads to the conclusion that the HPPMS process leads to smoother surface while the DC process rather produces a columnar morphology. The latter leads to an increased surface area, which is preferentially oxidized after the deposition process. The HPPMS process enables the deposition of smooth surfaces especially at short pulse durations which enables the reduction of the surface oxidation process.

In summary, we conclude that two effects can be considered if a tailored surface composition of (Cr,Al)N coatings is desired. First, the volume composition of the coating can be influenced by the characteristics of the HPPMS pulse parameters as shown within this work, aside from the process parameters like composition of the sputter target and partial pressures of the used reactive gases. Second, the composition of the final surface near region of the coatings upon reaction with an oxygen containing gas phase is not solely determined by the composition of the (Cr,Al)N coating but also by the microstructure and roughness.

Acknowledgements

The authors gratefully acknowledge the financial support of the German Research Foundation (DFG) within the transregional collaborative research center TRR 87/1-2010 "Pulsed high power plasmas for the synthesis of nanostructured functional layers" (SFB-TR 87), subprojects A1, A2 and C6.

References

[1] P. A. Dearnley, *Wear* **1999**, *225*, 1109.
[2] W. Michaeli, S. Hebner, F. Klaiber, J. Forster, W. Eversheim, *Cirp Ann.-Manufact. Technol.* **2007**, *56*, 545.
[3] K. Bobzin, R. Nickel, N. Bagcivan, F. D. Manz, *Plasma Processes Polym.* **2007**, *4*, S144.
[4] D. Music, D. Lange, L. Raumann, M. to Baben, F. von Fragstein, J. M. Schneider, *Surf. Sci.* **2012**, *606*, 986.
[5] T. Reeswinkel, D. Music, J. M. Schneider, *J. Phys.-Condens. Matter* **2009**, *21*, 145404.
[6] M. Ratzsch, M. Arnold, E. Borsig, H. Bucka, N. Reichelt, *Prog. Polym. Sci.* **2002**, *27*, 1195.
[7] J. Sohma, *Colloid Polymer Sci.* **1992**, *270*, 1060.
[8] J. M. Schneider, A. Anders, G. Y. Yushkov, *Appl. Phys. Lett.* **2001**, *78*, 150.
[9] A. Tempez, A. Bensaoula, A. Schultz, *J. Vac. Sci. Technol. Vac. Surf. Films* **2002**, *20*, 1320.
[10] C. Gnoth, C. Kunze, M. Hans, M. to Baben, J. Emmerlich, J. M. Schneider, G. Grundmeier, *J. Phys. D-Appl. Phys.* **2013**, *46*, 084003.
[11] J. Alami, K. Sarakinos, G. Mark, M. Wuttig, *Appl. Phys. Lett.* **2006**, *89*, 154104.
[12] J. Alami, K. Sarakinos, F. Uslu, M. Wuttig, *J. Phys. D-Appl. Phys.* **2009**, *42*, 015304.
[13] A. P. Ehiasarian, A. Vetushka, Y. A. Gonzalvo, G. Safran, L. Szekely, P. B. Barna, *J. Appl. Phys.* **2011**, *109*, 104314.
[14] M. P. Seah, W. A. Dench, *Surf. Interface Anal.* **1979**, *1*, 2.
[15] D. Briggs, P. Seah, Practical Surface Analysis: Auger and X-ray photoelectron spectroscopy, Wiley, Chichester, **1990**.
[16] V. Kouznetsov, K. Macak, J. M. Schneider, U. Helmersson, I. Petrov, *Surf. Coat. Technol.* **1999**, *122*, 290.
[17] J. Bohlmark, J. T. Gudmundsson, J. Alami, M. Latteman, U. Helmersson, *Ieee Trans. Plasma Sci.* **2005**, *33*, 346.

[18] J. T. Gudmundsson, in Proceedings of the 17th International Vacuum Congress/13th International Conference on Surface Science/ International Conference on Nanoscience and Technology, vol. *100* (Eds: L. S. O. Johansson, J. N. Andersen, M. Gothelid, U. Helmersson, L. Montelius, M. Rubel, J. Setina, L. E. Wernersson), Iop Publishing Ltd, Bristol, **2008**.
[19] N. Bagcivan, K. Bobzin, S. Theiss, *Thin Solid Films* **2013**, *528*, 180.
[20] G. Greczynski, L. Hultman, *Vacuum* **2010**, *84*, 1159.
[21] N. Wiberg, Inorganic Chemistry, de Gruyter, Berlin, **2001**.
[22] A. Lippitz, T. Hübert, *Surf. Coat. Technol.* **2005**, *200*, 250.
[23] S. Kaciulis, A. Mezzi, G. Montesperelli, F. Lamastra, M. Rapone, F. Casadei, T. Valente, G. Gusmano, *Surf. Coat. Technol.* **2006**, *201*, 313.
[24] E. Ünveren, E. Kemnitz, S. Hutton, A. Lippitz, W. E. S. Unger, *Surf. Interface Anal.* **2004**, *36*, 92.
[25] M. C. Biesinger, B. P. Payne, A. P. Grosvenor, L. W. M. Lau, A. R. Gerson, R. S. C. Smart, *Appl. Surf. Sci.* **2011**, *257*, 2717.
[26] B. Stypula, J. Stoch, *Corros. Sci.* **1994**, *36*, 2159.
[27] J. Sjölen, L. Karlsson, S. Braun, R. Murdey, A. Hörling, L. Hultman, *Surf. Coat. Technol.* **2007**, *201*, 6392.
[28] M. to Baben, L. Raumann, D. Music, J. M. Schneider, *J. Phys.-Condens. Matter* **2012**, *24*, 155401.

Supporting information

Additional supporting information may be found in the online version of this article at the publisher's web site.

Surface Chemistry of PVD (Cr,Al)N coatings deposited via Direct Current and High Power Pulsed Magnetron Sputtering

*Christian Kunze[1], Ricardo H. Brugnara[2], Nazlim Bagcivan[2], Kirsten Bobzin[2], Guido Grundmeier[1]**

[1] Technical and Macromolecular Chemistry, University of Paderborn, Paderborn, Germany.
[2] Surface Engineering Institute, RWTH Aachen University, Aachen, Germany.

*corresponding author: g.grundmeier@tc.uni-paderborn.de

Supporting Information

SEM cross section images

Cross section samples were prepared by scratching the backside of the Si wafer substrate with a diamond cutter followed by breaking the sample. The coating deposited at 200 µs exhibits a distinctive columnar structure compared to the DC-MS coating. As the pulse length is reduced from 200 to 80 and 40 µs, a change in the microstructure towards a fine microcrystalline morphology is observed.

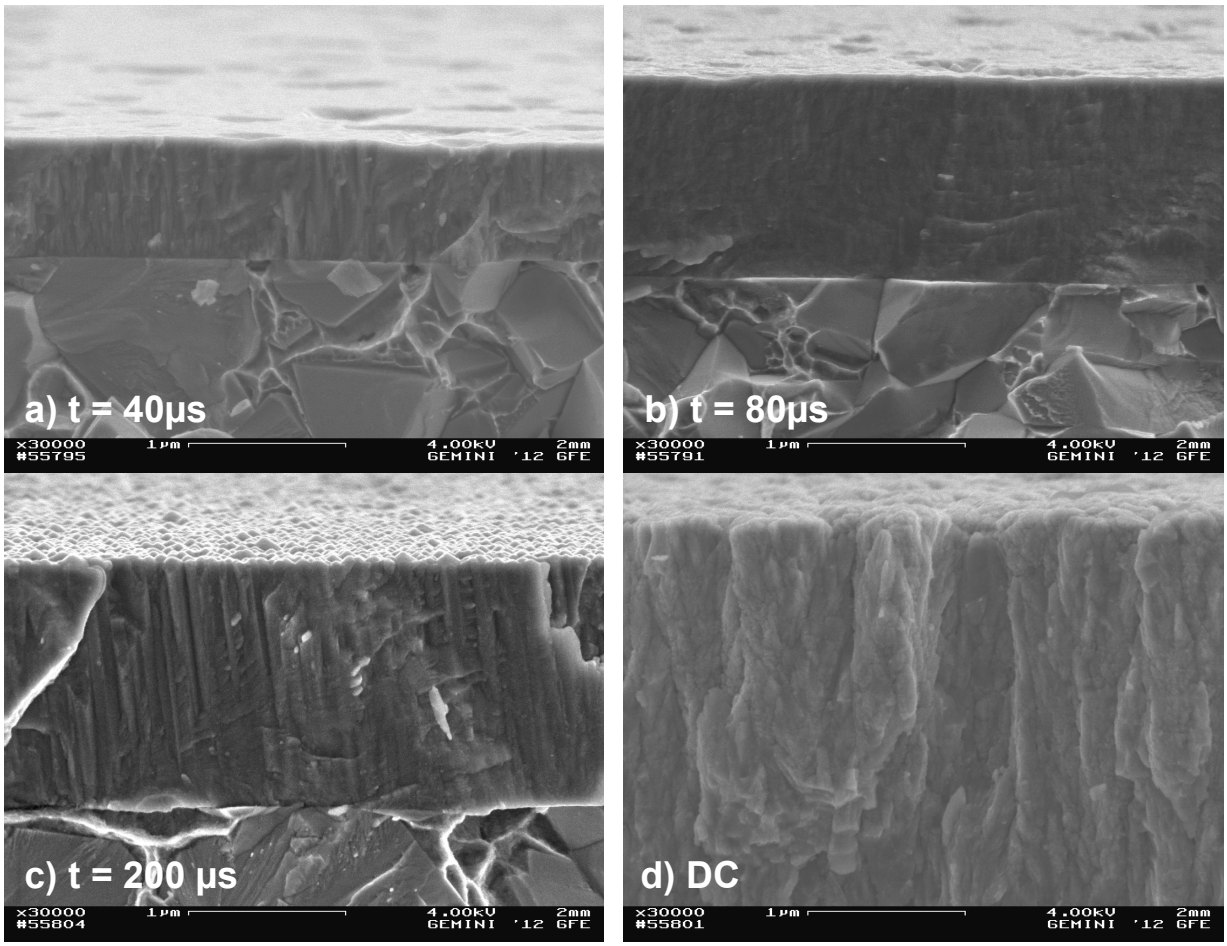

Figure 1: SEM cross-sectional images of the investigated (Cr,Al)N coatings. a) sample 1 (t = 40 µs), b) sample 2 (t = 80 µs), c) sample 3 (t = 200 µs), c) sample 4 (DC).

Voltage and current waveforms during HPPMS discharge

The recorded voltage and current waveforms during HPPMS discharge are demonstrated in Figure 2 representative for a pulse length of 200 µs (left) and 40 µs (right) at constant mean power (5kW) and frequency (500 Hz). With reduced pulse duration the current and voltage increase in order to keep the same cathode mean power.

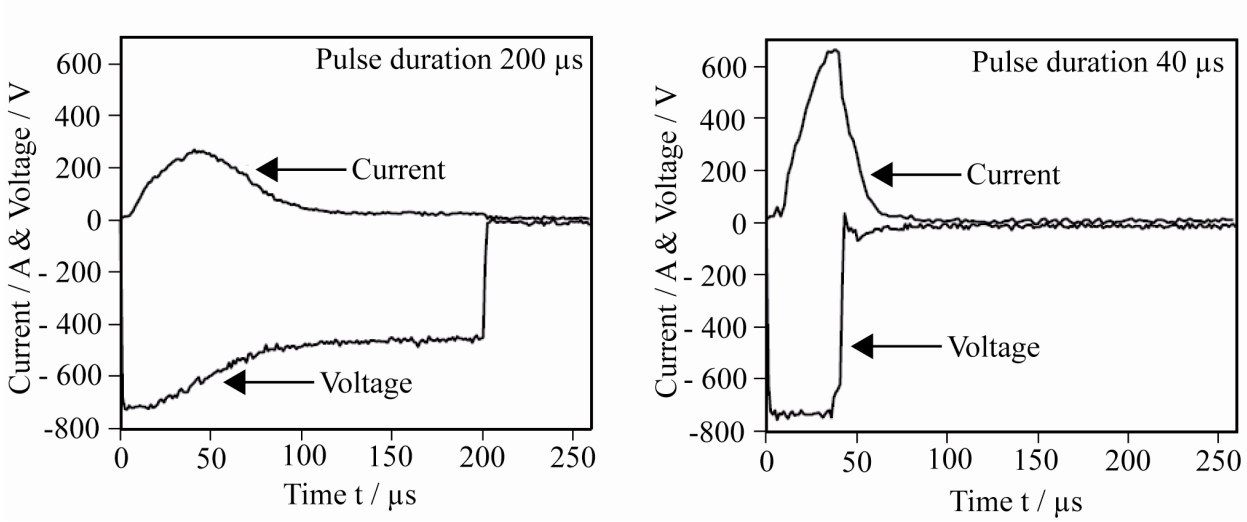

Figure 2: Cathode voltage and current measured during HPPMS discharge at constant mean power of 5 kW, frequency of 500 Hz and at a pulse duration of 200 µs (left) and 40 µs (right).

3.3 Influence of HPPMS Pulse Length and Inert Gas mixture on the Properties of (Cr,Al)N Coatings

Nazlim Bagcivan, Kirsten Bobzin, Guido Grundmeier, Martin Wiesing, Özlem Özcan, Christian Kunze, Ricardo H. Brugnara
Thin Solid Films, 549, **2013**, 192-198.

The scientific work and discussion was coordinated and consolidated by RHB and CK under supervision of GG and NB.
The manuscript was prepared by RHB and CK.
Hard coatings were deposited by RHB.
SEM, EDS, XRD and mechanical measurements and data evaluation were performed by RHB.
XPS measurements and data evaluation were performed by CK.
EIS measurements were performed by MW and ÖÖ.
The manuscript was revised by GG, NB and KB.

Within this paper the influence of different deposition parameters on the chemical composition of the surface near region of CrAlN hard coatings has been investigated. Short HPPMS pulse lengths led to an increased hardness of the deposited coatings, in comparison a coating deposited via DC-MS exhibited the lowest hardness. The use of krypton as an inert gas in the sputter process increased the deposition rate marginally while no significant changes of the mechanical properties could be observed. Electrochemical impedance spectroscopy (EIS) experiments could prove a more dense morphology of the coatings deposited by means of HPPMS which is in good correlation to the observed mechanical properties.

Thin Solid Films 549 (2013) 192–198

Contents lists available at ScienceDirect

Thin Solid Films

journal homepage: www.elsevier.com/locate/tsf

Influence of HPPMS pulse length and inert gas mixture on the properties of (Cr,Al)N coatings

N. Bagcivan [a], K. Bobzin [a], G. Grundmeier [b], M. Wiesing [b], O. Ozcan [b], C. Kunze [b], R.H. Brugnara [a,*]

[a] Surface Engineering Institute, RWTH Aachen University, Kackertstr. 15, D-52072 Aachen, Germany
[b] University of Paderborn, Technical and Macromolecular Chemistry, Warburger Str. 100, D-33098 Paderborn, Germany

ARTICLE INFO

Available online 4 July 2013

Keywords:
CrAlN
HPPMS
HIPIMS
PVD
Plastics industry

ABSTRACT

During the production of plastic products by injection molding processes adhesion and abrasion wear as well as corrosion take place in the molding tools. Concerning this, (Cr,Al)N coatings deposited via physical vapor deposition (PVD) have a good potential to be used as protective coatings on injection tools. For an effective protection of coated tools a uniform layer of coating material is also required. In this regard, the HPPMS (high power pulse magnetron sputtering) technology offers possibilities to improve coating thickness uniformity as well as to adapt the chemical and mechanical properties. The present work deals with the investigation of influence of HPPMS pulse length and the argon/krypton ratio in the deposition process on (Cr,Al)N coating properties. For this reason, (Cr,Al)N coatings were deposited with HPPMS pulse length of 40, 80 and 200 μs at constant Ar/Kr ratio (120/80 sccm). The results were compared with a coating deposited with DC Magnetron Sputtering (DC-MS) with the same Ar/Kr ratio. Afterwards, a (Cr,Al)N coating was deposited with constant pulse length (200 μs) without Kr. The chemical composition, morphology and phase composition of the coatings were analyzed by means of EDS (Energy Dispersive Spectroscopy), SEM (Scanning Electron Microscopy) and XRD (X-ray Diffraction), respectively. The composition of the surface near region in the samples was investigated by means of XPS (X-ray Photoelectron Spectroscopy). Mechanical properties were measured by means of nanoindentation. Decreasing of pulse length at constant mean power leads to a considerable increase of cathode current. It could be observed that the deposition rate of the HPPMS process reduces with decreasing pulse length. Nevertheless, short HPPMS pulse lengths and high peak currents lead to an increase of hardness from 25 GPa to 32 GPa while the DC-MS coating displays a hardness of 18 GPa. The use of krypton within the sputter process leads to a marginal increase of the deposition rate while the mechanical properties are not significantly changed. In addition, EIS (electrochemical impedance spectroscopy) was employed to investigate the defect structure of the coatings.

1. Introduction

During processing of plastic products using injection molding machines the surfaces of molding tools are often subject to adhesion and abrasion wear as well as corrosion [1]. Limited tool life of molding tools represents an issue for mass production especially of plastic products with complex geometries. Concerning this, coatings deposited via physical vapor deposition (PVD) have a good potential to be used as protective coatings on molding tools. It was demonstrated that the protection of molding tools can be improved and the adhesion of plastic melts can be reduced by using e.g. titanium and chromium based coatings [2,3]. Especially, (Cr,Al)N is an important hard transition metal nitride coating that exhibits high hardness, good abrasion wear resistance and high corrosion resistance [4–8], which makes this coating system a promising candidate for many different applications, e.g. cutting and forming operations [9–12]. Thus, (Cr,Al)N was chosen to be investigated in this work.

HPPMS (High Power Pulsed Magnetron Sputtering) is a physical vapor deposition (PVD) technology. Due to high-energy pulses a plasma density can be achieved which is higher by three orders of magnitude in comparison to conventional direct current (DC-MS) sputtering [13]. Furthermore, the MPP (Modulated Power Pulse) technique enables a creation of highly ionized sputtered species leading to deposition of dense coatings with deposition rates up to 15 μm/h and high hardness [14,15]. A detailed review of HPPMS/HIPIMS technology and its advantages is given from Sarakinos et al. [16] and Lundin et al. [17]. The main advantage of using HPPMS is that it provides high plasma densities and a high grade of ionization. First analysis using optical emission spectroscopy (OES) during sputtering of Cr and Ti targets have shown a considerable enhancement of ion/atom ratio by highly ionized plasmas compared to DC-MS sputtering [18,19]. Thus, the use of HPPMS allows for a better control of the energetic bombardment of the substrate. It offers the possibility to influence phases, microstructure, and composition of the coating by variation of the process parameters [20], e.g. peak current, frequency and pulse length. Investigations of CrN_x coatings show changes of the density and the surface roughness as the peak target current increased, while the deposition rate decreases drastically [21]. Other

* Corresponding author. Tel.: +49 241 809 5577; fax: +49 241 809 9306.
E-mail address: brugnara@iot.rwth-aachen.de (R.H. Brugnara).

0040-6090/$ – see front matter © 2013 Elsevier B.V. All rights reserved.
http://dx.doi.org/10.1016/j.tsf.2013.06.036

investigations of CrN_x reveal that an increasing frequency leads to a nano-sized grain structure and a partial suppression of the columnar growth [22]. Jing et al. reported that the crystal size and the surface roughness of titanium coatings increased with increasing pulse length [23].

The most commonly utilized inert gas for magnetron sputter deposition is argon, due to its combination of physical and chemical properties and its relatively low cost. However, the choice of the process gas may significantly affect the production and transport of a range of energetic species to the substrate, and subsequently the growth and properties of the deposited material [24]. Krypton is used for its greater atomic mass and size compared to argon, which leads to lower gas incorporation and may have beneficial effects on the kinetics of the coating growth. Its potential and kinetic secondary electron emission yields are somewhat lower than those for argon [25].

The presented work deals with the investigation of the influence of HPPMS pulse length on the properties of (Cr,Al)N coatings deposited with an argon/krypton mixture. The results were compared to other coatings obtained via a DC-MS process. For this reason, (Cr,Al)N coatings were deposited with HPPMS pulse lengths of 40, 80 and 200 μs at constant Ar/Kr ratio (120/80 sccm). The properties of these coatings were compared with a coating deposited with DC Magnetron Sputtering (DC-MS) with the same Ar/Kr ratio. Afterwards, a (Cr,Al)N coating was deposited with constant pulse length (200 μs) without Kr in the gas mixture. In addition, the chemical composition of the coatings was measured by EDS (Energy Dispersive Spectroscopy). An investigation of the chemistry of the surface near region of these coatings is of crucial importance towards understanding the interaction of the polymer melt with the (Cr,Al)N substrate such as adhesion, wear and related phenomena. To study the composition of the surface near region, X-ray photoelectron spectroscopy (XPS) was used. Tempez et.al. reported angle resolved XPS measurements for amorphous TiAlN coatings showing that the surface near region was partially oxidized and enriched with Al [26]. The information depth of XPS is limited to a few nanometers, so the results are representative for the composition of the native oxide layer of the coating. As our study focuses on (Cr,Al)N as a protective coating for tools within polymer processing it is straight forward to perform a comparative analysis of the bulk composition by means of EDS and an analysis of the surface near region by XPS as the interaction with the polymer melt is determined by the surface chemistry of the coating. Mechanical properties, morphology and phase composition were analyzed by means of Nanoindentation, SEM (Scanning Electron Microscopy) and XRD (X-ray Diffraction) measurements, respectively. EIS (electrochemical impedance spectroscopy) was employed in order to investigate the electrochemical properties and defect structure of the coatings.

2. Experimental

2.1. Materials and processes

The investigated coatings were deposited on cemented carbide (THM12), on silicon wafer (100) and on stainless steel AISI 304 (1.4301, X5CrNi18-10) via an industrial CC800/9 coating unit from CemeCon AG, equipped with one HPPMS power supply and one DC source, which were operated at constant mean power of 5 kW. A Cr target (500 × 80 mm) with 20 Al plugs (purity: Cr: 99.9% and Al: 99.5%) was applied for the deposition of the coatings. HPPMS (Cr,Al)N coatings were deposited using different pulse lengths (40, 80, 200 μs) at constant Ar/Kr ratio (120/80 sccm). The gas composition was chosen in order to achieve an Ar/Kr ratio of approximately 1.5 as reported by other authors [27–29]. Furthermore, a HPPMS (Cr,Al)N coating was deposited in pure Ar atmosphere (200 sccm) at 200 μs pulse length. In addition, a DC-MS coating was deposited with a Ar/Kr ratio of 120/80 sccm. During deposition samples were moved in a two-fold rotation. Other process parameters are shown in Table 1.

Table 1
Process parameters for deposition of the (Cr,Al)N coatings.

Deposition parameters	Unit	HPPMS	DC
Substrate	Cemented carbide, silicon, AISI 304 (1.4301, X5CrNi18-10)		
Mean cathode power	kW	5	5
Pulse length	μs	200/ 80/ 40	–
frequency	Hz	500	–
Bias voltage	V	−100	−100
Nitrogen flow		Pressure controlled	Pressure controlled
Pressure	mPa	450	450

2.2. Analytical methods

Morphology, topography and chemical composition of the samples were analyzed using scanning electron microscopy (SEM) with energy dispersive spectroscopy (EDS) for elemental analysis. The surface roughness was measured by means of a Hommel-Tester T2000 profilometer. The phase analysis was carried out via X-ray diffractometry with a grazing incidence X-ray diffractometer XRD 3003, General Electric. All measurements were performed using Cu-Kα (wavelength $\lambda = 0.15406$ nm) radiation operated at 40 kV and 40 mA. Hardness and Young's modulus were determined using a Nanoindenter XP, MTS Nano Instruments. The evaluation of the measured results was based on the equations according to Oliver and Pharr [30]. A Poisson's ratio of $\nu = 0.25$ was assumed.

XPS measurements were performed by means of an Omicron ESCA+Sytem (Omicron NanoTechnology GmbH, Taunusstein, Germany) with a base pressure of $<3 \cdot 10^{-4}$ mPa. The system is equipped with a hemispherical energy analyzer, the element spectra were recorded at pass energies of 25 eV. For photoelectron excitation a monochromated Al-Kα (1486.7 eV) X-ray source with a spot diameter of 600 μm was used. The take-off angle of the detected photoelectrons was 30° with respect to the surface normal. The calibration of the spectra was performed using the C 1 s peak (binding energy, BE = 285.0 eV) as an internal reference. For data evaluation the CasaXPS software (version 2.3.15) was used. All quantifications of the XPS data were done by integration of the peaks with regard to the relative sensitivities of the elements. As the core level energy of Al 2p overlaps with Cr 3 s, for the evaluation of the Al content the Al 2 s peak was used. Estimating the attenuation length of the electrons in a solid to $\lambda = \sim 2$ nm (for an Al-K_α X-ray source at 1486.7 eV), the information depth d can be estimated to about $3\lambda \cdot \cos(30) = 5.0–5.5$ nm [31].

Electrochemical impedance spectroscopy (EIS) measurements were performed with a Reference 600 (Gamry, Germany) potentiostat. A gold wire and a saturated Ag/AgCl electrode were used as counter and reference electrodes, respectively. Impedance data was collected in a borate buffer electrolyte (pH ~ 8.4, 19.1 g/L sodiumtetraborate decahydrate, 12.4 g/L boric acid und 7.1 g/L sodium sulfate) for a frequency range of $1–10^5$ Hz by superimposing a 10 mV AC voltage at open circuit potential.

3. Results and discussion

3.1. Cathode voltage and current measurement during HPPMS discharge

The generated pulse shape during HPPMS discharge is demonstrated in Fig. 1 representative for a pulse length of 200 μs (left) and 40 μs (right) at constant mean power (5 kW) and frequency (500 Hz). When the pulse length is reduced, the current and voltage are increased in order to keep the same mean power. It can be observed that the peak current increases drastically from 260 A at 200 μs, to 280 A at 80 μs and to 660 A at 40 μs. Higher peak currents can be associated with an increased plasma ionization rate as it was reported by Alami et al. [21,32] for Cr sputtering. Therefore, it can be assumed that the ionization rate of the metal atoms is dramatically increased with increasing peak current.

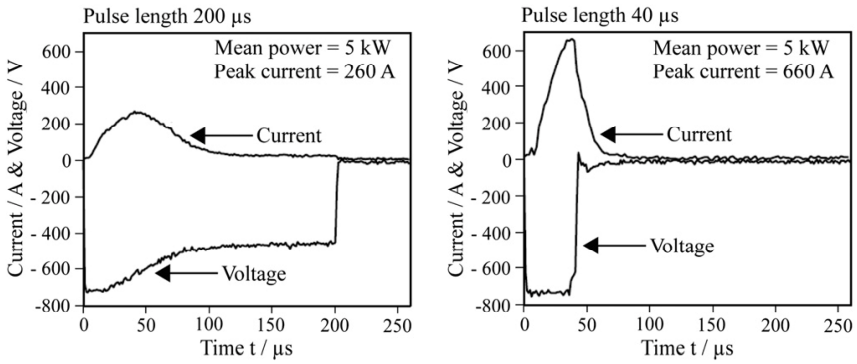

Fig. 1. Cathode voltage and current measured during HPPMS discharge at constant mean power of 5 kW, frequency of 500 Hz and at a pulse length of 200 µs (left) and 40 µs (right).

3.2. Chemical composition, morphology and topography

The chemical composition of the deposited coatings as measured by EDS is shown in Table 2. The content of nitrogen is not discussed in this section due to the fact that a quantitative EDS analysis is not possible for light elements. The results show almost constant aluminum and chromium contents with decreasing pulse length. The coatings deposited with and without Kr show also no variation in the chemical composition. An increase of the Al-content of the HPPMS coatings compared to the DC-MS sample can be observed.

Table 2
Chemical composition and thickness of the (Cr,Al)N coatings as determined by EDS and REM.

Sample	Ar/Kr [sccm]	Pulse length [µs]	Cr [at.%]	Al [at.%]	Coating thickness [µm]	Deposition rate [µm/h]
HPPMS-1	120/80	200 µs	79	21	1.55	0.77
HPPMS-2	120/80	80 µs	78	22	1.30	0.65
HPPMS-3	120/80	40 µs	76	24	0.80	0.40
HPPMS-4	200	200 µs	79	21	1.45	0.72
DC	120/80	–	88	12	3.1	1.55

This fact can be attributed to the higher sputter rate of aluminum in HPPMS process compared to DC-MS [28]. The coating thicknesses in Table 2 were determined using SEM. The deposition rates show a decrease with lower pulse lengths at the same mean power. This effect can be explained by the fact that short pulses lead to a substantial increase of peak current, as demonstrated in Fig. 1, resulting in an increase in ionization accompanied by a decrease of the deposition rate, due to self-sputtering [32].

Analysis of the morphology and the topography of the coatings were performed by means of SEM. Cross section fractures of DC-MS and HPPMS coatings deposited at 200, 80 and 40 µs are shown in Fig. 2. It can be clearly seen that the film deposited at 200 µs has a finer columnar morphology compared to the DC-MS coating. As the pulse length is reduced from 200 to 80 and 40 µs, it is clearly visible that the columnar morphology disappeared and a dense fine grained crystalline morphology is observed. The SEM micrographs of the surface (e–h) show a compact and closed coating surface, but with some pits when the pulse length is reduced. Nevertheless, the surface roughness (Ra) is 0.019 µm for the pulse duration of 200 µs and decreases to 0.014 µm for 40 µs. For DC-MS, Ra is 0.039 µm. It can be concluded, that the coating surface deposited at reduced pulse lengths is smoother than those at same average power by HPPMS (200 µs) and

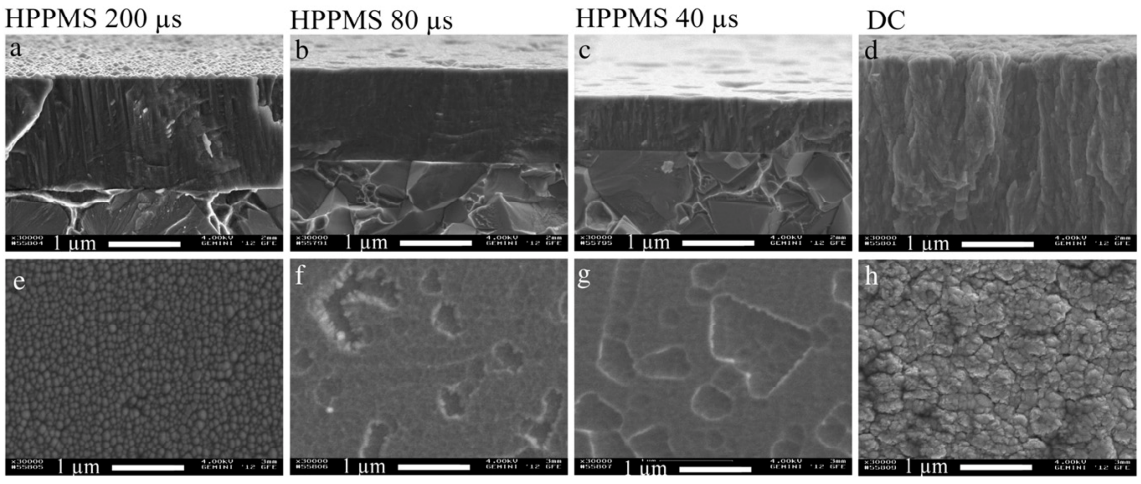

Fig. 2. SEM cross section fractures (a–d) and SEM images of the surfaces (e–h) of (Cr,Al)N coatings deposited via HPPMS at 200, 80 and 40 µs as well DC-MS process.

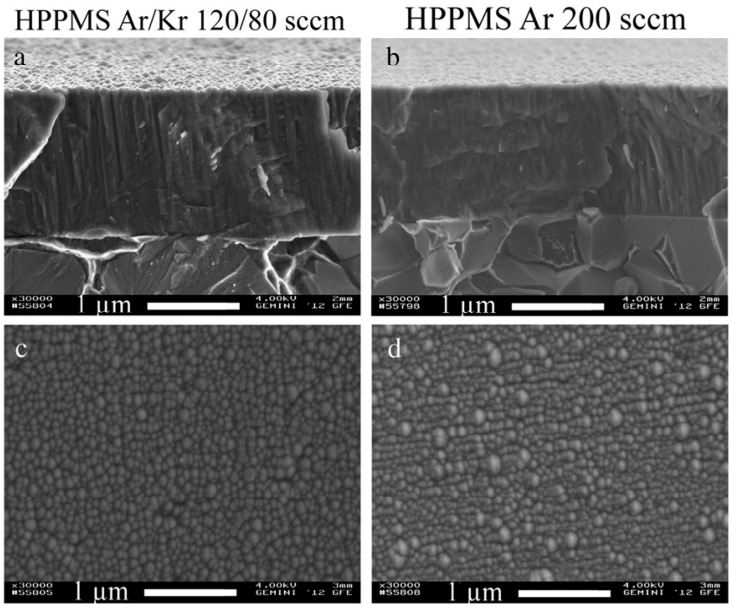

Fig. 3. SEM cross section fractures (a–b) and SEM image of the surfaces (c–d) of (Cr,Al)N coatings deposited via HPPMS at 200 µs with a Ar/Kr ratio of 120/80 sccm and with Ar (200 sccm).

DC-MS. This result could be attributed to the increased metal ion flux commonly observed in the HPPMS discharges. The ion bombardment that leads to a higher flux ratio of metal ions to neutrals results in an increased ad-atom mobility and a smoother surface [33–35].

Cross section fractures of HPPMS coatings deposited at 200 µs with and without Kr are shown in Fig. 3. The morphology and surface topography of both coatings are very similar. Its leads to the assumption, that the use of Kr in the investigated Ar/Kr ratio (120/80 sccm) does not have a considerable influence on the microstructure of the HPPMS (Cr,Al)N coating.

3.3. Composition of surface near region

The chemical composition of the surface near region was analyzed to compare the chemistry of the surface near region to the bulk composition of the coatings deposited at various deposition parameters. As aforementioned, the information depth can be estimated to about 5.0–5.5 nm. On all samples a significant contribution of C 1 s was found, which can be discussed as a native contamination layer which forms upon contact with the environmental atmosphere and mainly consists of low-weight (hydro)carbon species. Within our studies we tolerated the presence of the carbon contamination as it is also relevant for the application of the coatings in the technical process. Furthermore its impact on the analysis of the chemical composition (originating from "overlayer"-effects) of the coatings is negligible as the carbon concentration on all samples was quite similar (between 28 at.% and 30 at.%), and all XPS experiments were performed with a high depth of information from the surface near region. Nevertheless, all further XPS data are presented without discussing the carbon content. Fig. 4 shows a representative XPS spectrum of the surface near region of the HPPMS (Cr,Al)N deposited at 200 µs with a Ar/Kr ratio of 120/80 sccm.

The elemental compositions of all investigated coatings are shown in Table 3. The presence of noble gases (Ar, Kr) could not be detected in any of the investigated samples. The lower detection limit of these elements in XPS can be estimated to about 1 at.%. Thus, it can be followed that the implantation of noble gases in the surface near region plays a negligible role. A significant amount of oxygen can be assigned to the oxidation of the surface near region immediately after the end of the deposition processes in an atmosphere with relatively high oxygen and water partial pressures. Surface concentrations of oxygen ranged from 28 to 44 at.%. Moreover, the concentration of aluminum in the surface near region is significantly increased as seen from the comparative EDS data and XPS measurements. This finding can be explained by the preferential formation of aluminum oxide in the surface near region, which has been already observed for (Ti,Al)N coatings [36]. The formation of aluminum oxide instead of chromium oxide is thermodynamically favored comparing the standard enthalpies of formation of Al_2O_3 ($\Delta H^0_f = -1677$ kJ/mol) to Cr_2O_3 ($\Delta H^0_f = -1140$ kJ/mol) [37].

Table 4 shows element ratios calculated from the XPS composition data for all investigated coatings. The elemental compositions shown in Tables 3 and 4 do not show a significantly different composition

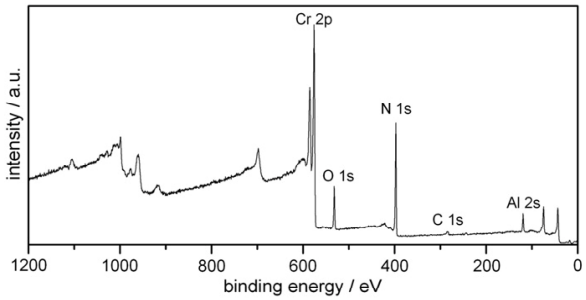

Fig. 4. Typical XPS survey spectrum of the surface near region of a (Cr,Al)N coating deposited at 200 µs with a Ar/Kr ratio of 120/80 sccm.

Table 3
Chemical composition of all investigated (Cr,Al)N coatings in the surface near region. All data are shown with an experimental uncertainty of +/−2 at.% resulting from the XPS measurement. Carbon was excluded from the calculation.

Sample ([Ar/Kr] sccm, [t] µs)	Cr 2p [at.%]	Al 2s [at.%]	N 1s [at.%]	O 1s [at.%]
HPPMS-1 (120/80 sccm, 200 µs)	24	15	19	42
HPPMS-2 (120/80 sccm, 80 µs)	23	17	21	39
HPPMS-3 (120/80 sccm, 40 µs)	24	15	34	27
HPPMS-4 (200/0 sccm, 200 µs)	24	16	27	33
DC (120/80 sccm)	28	8	20	44

comparing samples HPPMS-1 and HPPMS-2 except of the observed Cr/Al ratio. Both coatings were deposited with the same inert gas mixture (Ar/Kr 120/80 sccm) at different HPPMS pulse lengths of 200 µs and 80 µs, respectively. The coating deposited without Kr (Sample HPPMS-4) shows an increased N/O ratio which is even more significant for the coating deposited at 40 µs (HPPMS-3). This finding might lead to the assumption that these coatings are less sensitive to oxidation of the surface near region after deposition. At this point it is not fully understood whether the presence of Argon as the only inert gas in the plasma (in case of HPPMS-4) or the short HPPMS pulse length (in case of HPPMS-3) leads to the difference in composition of surface near region. Further studies are necessary to investigate this effect. For all HPPMS coatings an almost identical metal (Cr + Al) to nonmetal (N + O) ratio was observed. The coating prepared in the DC sputter process shows a significantly different composition of the surface near region in comparison to the HPPMS samples which is mainly hallmarked by a significantly increased Cr/Al ratio. This finding can be explained by an increased sputter rate of Al in the HPPMS process which has been already reported in [28]. Additionally, a decreased metal/nonmetal ratio (Cr + Al)/(N + O) was observed in the surface near region which correlates with the smaller sputter rate of Al during the DC-MS process.

Table 4
Element ratios calculated from the XPS composition data. The calculated values include an estimated error of 4%.

Sample ([Ar/Kr] sccm, [t] µs)	Cr/Al	N/O	(Cr + Al)/(N + O)
HPPMS-1 (120/80 sccm, 200 µs)	1.67	0.46	0.64
HPPMS-2 (120/80 sccm, 80 µs)	1.38	0.53	0.66
HPPMS-3 (120/80 sccm, 40 µs)	1.55	1.22	0.63
HPPMS-4 (200/0 sccm, 200 µs)	1.50	0.82	0.66
DC (120/80 sccm)	3.32	0.46	0.56

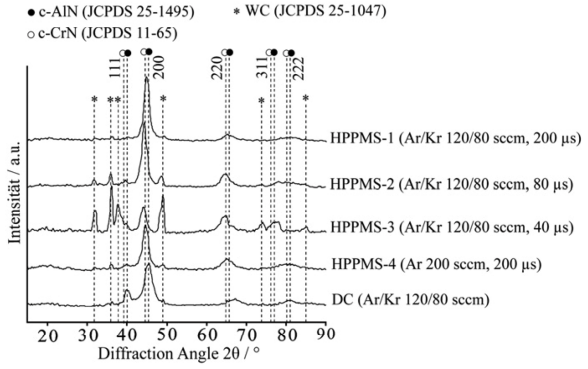

Fig. 5. XRD patterns of the (Cr,Al)N coatings.

3.4. Phase analysis

The phase composition of the (Cr,Al)N coatings was analyzed using XRD. Fig. 5 shows the XRD patterns of all deposited coatings. The increase of the substrate peaks can be explained by the different coating thicknesses. All coatings present a NaCl-type crystal structure, indicating that the crystalline structures of the (Cr,Al)N coatings are predominantly cubic. The diffraction peaks of the crystallographic planes (111), (200), (220), (311) and (222) corresponding to the cubic CrN and cubic AlN phase are identified. Furthermore, a preferential growth of (200) grains is observed for the HPPMS coatings as well as the DC-MS sample. According to [38], the CrN (200) plane presents the lowest surface energy. One possible explanation of the occurrence of a (200) preferred orientation can be the formation of new crystal islands during the deposition with bias (−100 V) in order to minimize the coating surface energy, which has been demonstrated by other authors [28,39,40].

3.5. Mechanical properties

The Hardness, Young's modulus and the H^3/E^2 ratio of the investigated coatings are shown in Table 5. The H^3/E^2 ratio can be used as an important parameter to evaluate the resistance of materials to plastic deformation. In other words, the plastic deformation is reduced with high ratio of H^3/E^2 [41]. All HPPMS (Cr,Al)N films showed a significantly higher hardness and H^3/E^2 ratio compared to the DC-MS coating. One explanation for this is the low Al content in the DC-MS coating. With decreasing pulse length from 200 to 40 µs a considerable increase of hardness (from 25.0 to 32.4 GPa) and H^3/E^2 (from 0.086 to 0.163 GPa) was achieved. It is known that the decrease of the coating porosity, which means an increase of the material density, leads to an enhancement of the hardness. In this study, as the pulse length was reduced from 200 to 80 and 40 µs, the peak current is increased and the microstructure became denser, which could be contributed to the improvement of the hardness and H^3/E^2 ratio.

3.6. Electrochemical impedance spectroscopy (EIS)

The impedance and phase angle graphs of the investigated coating systems are presented in Fig. 6. For low frequencies an increase of impedance was observed with all HPPMS (Cr,Al)N coatings in comparison to the reference steel substrate AISI 304 (1.4301, X5CrNi18-10). For the samples prepared with an Ar/Kr ratio of 120/80 sccm and with pulse lengths of 200 and 80 µs, as well as the sample deposited with a pulse length of 200 µs under pure Ar atmosphere EIS analysis yielded similar profiles. EDX and XPS analyses indicated a similar chemical composition of the HPPMS coatings which was also reflected in the electrochemical properties. A clear difference was observed comparing films prepared by means of HPPMS and DC-MS processes,

Table 5
Hardness and Young's modulus of (Cr,Al)N coatings determined by Nanoindentation.

Sample ([Ar/Kr] sccm, [t] µs)	Hardness [GPa]	Young's modulus [GPa]	H^3/E^2 [GPa]
HPPMS-1 (120/80 sccm, 200 µs)	25.0 ± 1.5	425 ± 17	0.086
HPPMS-2 (120/80 sccm, 80 µs)	30.1 ± 2.6	408 ± 28	0.163
HPPMS-3 (120/80 sccm, 40 µs)	32.4 ± 3.7	453 ± 44	0.165
HPPMS-4 (200/0 sccm, 200 µs)	25.3 ± 1.5	418 ± 21	0.092
DC (120/80 sccm)	18.0 ± 2.2	393 ± 25	0.037

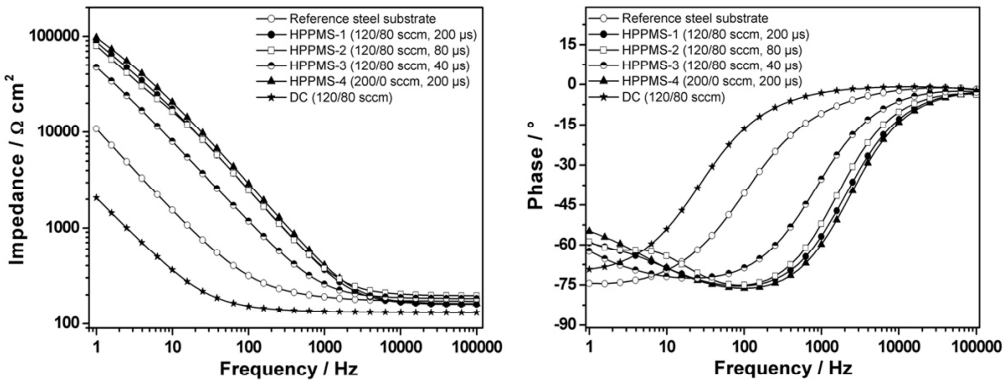

Fig. 6. Impedance and phase angle graphs of (Cr,Al)N coatings on stainless steel substrates AISI 304 (1.4301, X5CrNi18-10).

Table 6
Calculated capacitance values for (Cr,Al)N coatings prepared by means of HPPMS process.

Sample ([Ar/Kr] sccm, [t] µs)	Frequency at phase minimum [Hz]	Capacitance at phase minimum [µF]
HPPMS-1 (120/80 sccm, 200 µs)	79	0.67
HPPMS-2 (120/80 sccm, 80 µs)	100	0.65
HPPMS-3 (120/80 sccm, 40 µs)	20	1.90
HPPMS-4 (200/0 sccm, 200 µs)	100	0.56

where the DC-MS sample has shown significantly lower impedance values at lower frequencies.

Additionally, the capacitances of the (Cr,Al)N coatings prepared by means of HPPMS process were evaluated at the phase minima and are presented in Table 6. The samples prepared with an Ar/Kr ratio of 120/80 sccm at pulse lengths of 200 and 80 µs, as well as the sample deposited with a pulse length of 200 µs under pure Ar atmosphere did not show a significant difference in the evaluated capacitance values. Considering that all HPPMS films have a similar chemical composition (see Table 2), the slight increase in the capacitance of the coating prepared at 40 µs could be explained with the lower thickness of this coating.

The DC-MS (Cr,Al)N coating had a phase profile similar to the AISI 304 (1.4301, X5CrNi18-10) reference sample and has shown no phase minimum indicating that the double layer capacitance is dominating the impedance response of the system. This behavior of the DC-MS (Cr,Al)N coating could be explained with a combined effect of the increase in Cr/Al ratio and the film morphology. The DC-MS process is known to generate a coating microstructure with lower density in comparison to the HPPMS process, as discussed before. The decreased impedance values observed at low frequencies and the phase angle profile indicate the presence of pores in the DC-MS coating compared to HPPMS coatings.

4. Summary

The synthesis of (Cr,Al)N coatings by HPPMS has been studied for various values of pulse length (200, 80, 40 µs) and for different inert gas mixtures (Ar/Kr 120/80 and Ar/Kr 200/0 sccm) at constant mean power. One DC-MS experiment was carried out at the same mean power values and constant Ar/Kr ratio (120/80 sccm) for comparison. The shortening of pulse length led to a significant increase of peak current from 280 A at 200 µs to 660 A at 40 µs. It was observed that the deposition rate of HPPMS (Cr,Al)N was predominantly influenced by variation of pulse length and accordingly the peak current. The deposition rate decreased nonlinearly with reduced pulse length. For the HPPMS coatings the highest deposition rate (0.77 µm/h) was obtained at a 200 µs pulse length and an Ar/Kr ratio of 120/80 sccm.

In the (Cr,Al)N coating deposited at a pulse length of 80 and 40 µs it is clearly visible that the columnar structure disappeared and a dense fine grained crystalline microstructure is observed. Further, a smoother surface was achieved compared to the DC-MS and HPPMS coating (200 µs). The experiments with and without Kr did not show a considerable influence of this noble gas on the microstructure of the coatings. For all investigated coatings a significant amount of oxygen was detected in the surface near region, due to a passivation reaction of the surface near region. The surface concentrations of oxygen ranged from 28 to 44 at.%, with the lowest oxygen content in the coating deposited at 40 µs. Hence, the composition of the surface passive layer has to be taken into account when discussing interfacial processes such as adhesion and interactions with a polymer melt. The preferred orientation is (200) for the DC-MS as well as HPPMS coatings. Regarding the mechanical properties a significant increase of hardness and H^3/E^2 ratio is achieved when the pulse length is reduced from 200 µs (25.0 GPa; 0.086 GPa) to 40 µs (32.4 GPa; 0.163 GPa). EIS results were in good agreement with the microstructure and chemical composition analysis indicating the presence of a defect rich structure in the DC-MS coating compared to the HPPMS coatings.

Acknowledgment

The authors gratefully acknowledge the financial support of the German Research Foundation (DFG) within the transregional collaborative research center TRR87/1 (SFB-TR 87) subprojects A1, A2 and C6.

References

[1] E.J. Bienk, N.J. Mikkelsen, Wear 207 (1–2) (1997) 6.
[2] K. Bobzin, R. Nickel, N. Bagcivan, F.D. Manz, Plasma Processes Polym. 4 (S1) (2007) 144.
[3] G. Tosello, H.N. Hansen, S. Gasparin, J.A. Albajez, J.I. Esmoris, CIRP Ann. Manuf. Technol. 61 (1) (2012) 535.
[4] O. Knotek, F. Löffler, H.-J. Scholl, Surf. Coat. Technol. 45 (1991) 53.
[5] J. Lin, B. Mishra, J.J. Moore, W.D. Sproul, Surf. Coat. Technol. 201 (2006) 4329.
[6] Harish C. Barshilia, N. Selvakumar, B. Deepthi, K.S. Rajam, Surf. Coat. Technol. 201 (6) (2006) 2193.
[7] K. Bobzin, E. Lugscheider, R. Nickel, N. Bagcivan, A. Krämer, Wear 263 (2007) 1274.
[8] Xing-zhao Ding, A.L.K. Tan, X.T. Zeng, C. Wang, T. Yue, C.Q. Sun, Thin Solid Films 516 (16) (2008) 5716.
[9] B.C. Schramm, H. Scheerer, H. Hoche, E. Broszeit, E. Abele, C. Berger, Surf. Coat. Technol. 188 (2004) 623.
[10] G.S. Fox-Rabinovich, B.D. Beake, J.L. Endrino, S.C. Veldhuis, R. Parkinson, L.S. Shuster, M.S. Migranov, Surf. Coat. Technol. 200 (2006) 5738.

[11] K.-D. Bouzakis, N. Michailidis, S. Gerardis, G. Katirtzoglou, E. Lili, M. Pappa, M. Brizuela, A. Garcia-Luis, R. Cremer, Surf. Coat. Technol. 203 (25) (2008) 781.
[12] M. Wieland, M. Merklein, Key Eng. Mater. 438 (2010) 81.
[13] J. Alami, P.A.O. Persson, D. Music, J.T. Gudmundsson, J. Böhlmark, U. Helmersson, J. Vac. Sci. Technol. A 23 (2) (2005) 278.
[14] J. Lin, J.J. Moore, W.D. Sproul, B. Mishra, Z. Wu, J. Wang, Surf. Coat. Technol. 204 (2010) 2230.
[15] J. Lin, W.D. Sproul, J.J. Moore, S. Lee, S. Myers, Surf. Coat. Technol. 205 (2011) 3226.
[16] K. Sarakinos, J. Alami, S. Konstantinidis, Surf. Coat. Technol. 204 (11) (2010) 1661.
[17] D. Lundin, K. Sarakinos, J. Mater. Res. 27 (5) (2012) 780.
[18] A.P. Ehiasarian, R. New, W.-D. Münz, L. Hultman, U. Helmersson, V. Kouznetsov, Vacuum 65 (19) (2002) 147.
[19] A.P. Ehiasarian, W.-D. Münz, L. Hultman, U. Helmersson, I. Petrov, Surf. Coat. Technol. 163–164 (2003) 267.
[20] J. Alami, S. Bolz, K. Sarakinos, J. Alloys Comp. 483 (2009) 530.
[21] J. Alami, K. Sarakinos, F. Uslu, M. Wuttig, J. Phys. D: Appl. Phys. 42 (2009) 015304, (7 pp.).
[22] G. Greczynski, J. Jensen, J. Böhlmark, L. Hultman, Surf. Coat. Technol. 205 (25) (2010) 118.
[23] F.J. Jing, T.L. Yin, K. Yukimura, H. Sun, Y.X. Leng, N. Huang, Vacuum 86 (12) (2012) 2114.
[24] G.T. West, P.J. Kelly, Surf. Coat. Technol. 206 (7) (2011) 1648.
[25] A. Anders, Surf. Coat. Technol. 205 (2) (2011) S1.
[26] A. Tempez, A. Bensaoula, A. Schultz, J. Vac. Sci. Technol. A 20 (2002) 1320.
[27] M. Panjan, T. Peterman, M. Čekada, P. Panja, Surf. Coat. Technol. 204 (6–7) (2009) 850.
[28] N. Bagcivan, K. Bobzin, S. Theiß, Thin Solid Films 528 (2013) 180.
[29] E. Vogli, W. Tillmann, U. Selvadurai-Lassl, G. Fischer, J. Herper, Appl. Surf. Sci. 257 (20) (2011) 8550.
[30] W.C. Oliver, G.M. Pharr, J. Mater. Res. 7 (1992) 1564.
[31] J.F. Watts, J. Wolstenholme, J. Wiley, Chichester and West Sussex and England and and New York, 2003.
[32] J. Alami, K. Sarakinos, G. Mark, M. Wuttig, Appl. Phys. Lett. 89 (2006) 154104.
[33] V. Kouznetsov, Karol Macak, J.M. Schneider, U. Helmersson, Surf. Coat. Technol. 122 (1999) 290.
[34] J. Bohlmark, J.T. Gudmundsson, J. Alami, M. Latteman, U. Helmersson, IEEE Trans. Plasma Sci. 33 (2005) 346.
[35] J.T. Gudmundsson, J. Phys. Conf. Ser. 100 (2008), (id. 082013).
[36] C. Gnoth, C. Kunze, M. Hans, M. to Baben, J. Emmerlich, J.M. Schneider, G. Grundmeier, J. Phys. D: Appl. Phys. 46 (2013) 084003, http://dx.doi.org/10.1088/0022-3727/46/8/084003, (7 pp.).
[37] A.F. Holleman, N. Wiberg, de Gruyter, Berlin, 102 (2007) ISBN 978-3-11-017770-1.
[38] G. Abadias, Surf. Coat. Technol. 202 (2008) 2223.
[39] Y. Lv, L. Ji, X. Liu, H. Li, H. Zhou, J. Chen, Appl. Surf. Sci. 258 (2012) 3864.
[40] Q.H. Kong, L. Ji, H.X. Li, X.H. Liu, Y.J. Wang, J.M. Chen, H.D. Zhou, Mater. Sci. Eng. B: Adv. Funct. Solid-State Mater 176 (2011) 850.
[41] J. Musil, Surf. Coat. Technol. 125 (2000) 322.

3.4 Temporal evolution of oxygen chemisorption on TiAlN

Christian Kunze, Denis Music, Moritz to Baben, Jochen M. Schneider, Guido. Grundmeier
Applied Surface Science, 290, **2013**, 504-508.

The scientific work and discussion was coordinated and consolidated by CK under supervision of GG.
The manuscript was prepared by CK; DM contributed to the discussion of the molecular dynamics simulation results.
Hard coatings were deposited by MtB.
MD simulations and data evaluation were performed by DM.
XPS measurements and data evaluation were performed by CK.
The manuscript was revised by GG and JMS.

Within this paper the temporal evolution of oxygen chemisorption on TiAlN surfaces has been studied by *in-situ* XPS experiments and complementary *ab initio* molecular dynamics (MD) simulations. It could be shown that oxygen preferentially reacts with surface Ti atoms although the formation of Al–O bonds would be expected due to thermodynamic reasons. The reaction goes along with the displacement of Ti from the surface plane. Within this work it could be shown experimentally and theoretically that Ti and not Al determines the chemisorption of oxygen on TiAlN for the first time.

Applied Surface Science 290 (2014) 504–508

Contents lists available at ScienceDirect

Applied Surface Science

journal homepage: www.elsevier.com/locate/apsusc

Temporal evolution of oxygen chemisorption on TiAlN

ARTICLE INFO

Keywords:
TiAlN
Chemisorption
X-ray photoelectron spectroscopy
Ab initio molecular dynamics

ABSTRACT

The temporal evolution of the surface chemistry of cubic TiAlN at 1×10^{-3} mPa oxygen partial pressure and 300 K was analysed by means of X-ray photoelectron spectroscopy and by *ab initio* molecular dynamics simulations. Both the experimental and theoretical data imply that Ti and not Al determines the oxygen chemisorption process. Dissociative adsorption of oxygen is followed by upward movements of Ti, generating vacancies in the TiAlN interface and the formation of Ti—O—Ti bridges with Ti_2O_3-like bonding passivating the surface.

1. Introduction

TiAlN is widely used as protective coating for cutting and forming tools due to the high hardness combined with good oxidation and wear resistance [1,2]. It exhibits the NaCl structure (space group Fm-3m) up to an AlN fraction of 0.5–0.9 [3–9], where it transforms into the thermodynamically stable hexagonal configuration with inferior mechanical properties. While structure, phase stability, electronic structure, and mechanical properties of TiAlN have been discussed extensively [3,10–15], its surface characteristics have only recently been studied even though they are critical for the performance of protective coatings in contact with molten aluminum [16] or for polymer forming tools [17,18].

It was shown previously by chemical analysis of TiAlN and TiAlNO protective coatings that oxygen is enriched at the surface near region [19]. The oxidation of the surface near region was suggested to be due to reaction with residual gas immediately after deposition during cooling in the deposition system and/or reaction with atmospheric oxygen at room temperature [19]. Tempez et al. studied amorphous TiAlN coatings by means of ex situ X-ray photoelectron spectroscopy (XPS) and reported that the surface near region was partly oxidized giving rise to Ti—O and Al—O bonding along with an enrichment of Al due to air exposure [20]. The detailed chemical composition of the surface near region formed under atmospheric conditions of high power pulsed magnetron sputtering (HPPMS) TiAlN and TiAlNO coatings have been discussed recently [19]. In a recent theoretical work [21], surface processes on $Ti_{0.5}Al_{0.5}N(0\,0\,1)$ interacting with O_2 at room temperature were explored using *ab initio* molecular dynamics (MD) simulations. Dissociative adsorption of O_2 occurs on Ti sites, which are unusual sites as Al_2O_3 is more stable than TiO_2. It was suggested that an increased Ti—O bond strength relative to Al—O surface bond strength is the electronic origin for the early stages of titanium oxide formation on $Ti_{0.5}Al_{0.5}N(0\,0\,1)$. At larger coverages, Al—O bonds are formed. Another unexpected finding was that Ti escapes from the TiAlN(0 0 1)/O interface layer, moves upwards generating both vacancies and the coverage of the nitride interface layer with Ti—O [21]. These predictions have not been confirmed by experiments as no temporal evolution of the surface chemistry is available in literature.

At elevated temperatures, surface chemistry and kinetics may be radically different. McIntyre et al. studied the oxidation of TiAlN at temperatures between 1023 and 1173 K in a pure oxygen atmosphere at ambient pressure [2]. Under these conditions they identified aluminum and oxygen as the mobile species leading to an aluminum oxide rich top layer of about 100 nm in thickness with an underlying titanium oxide rich layer of similar thickness. An oxidation kinetics that initially varies parabolically with time has been observed, followed by accelerated oxidation in conjunction with crack formation.

Other spectroscopic methods offer complementary information about the bulk phase of the investigated material. Barshilia and Rajam studied the thermal stability of TiAlN coatings by means of Raman spectroscopy [22]. Under atmospheric conditions they did not observe any changes below 973 K and reported a formation of anatase TiO_2 and Al_2O_3 at 1073 K, whereas they did not observe a phase transformation for the same coatings annealed under vacuum conditions.

In this work, we devise a strategy to identify the temporal evolution of the surface chemistry of TiAlN at a low O_2 partial pressure of 1×10^{-3} mPa. We studied the temporal evolution of surface chemistry of HPPMS and TiAlN coatings at 300 K combining XPS and *ab initio* MD simulations.

2. Theoretical methods

To identify the atomic processes leading to the observed chemisorption kinetics, an *ab initio* MD study of $Ti_{0.5}Al_{0.5}N(0\,0\,1)$ interacting with four O_2 molecules was carried out using the OpenMX code [23], based on the density functional theory [24] and basis functions in the form of linear combination of localized pseudo atomic orbitals [25] in conjunction with the generalized gradient approximation [26]. The basis functions used were specified as follows: Ti5.0-s2p2d1, Al6.0-s2p2, N4.5-s2p1, and

0169-4332/$ – see front matter © 2013 Elsevier B.V. All rights reserved.
http://dx.doi.org/10.1016/j.apsusc.2013.11.091

O4.5-s2p1. Ti, Al, N, and O designate the chemical name, followed by the cutoff radius (Bohr radius units) in the confinement scheme and the last set of symbols defines primitive orbitals applied. The energy cutoff (150 Ry) and the $96 \times 96 \times 240$ real-space grid were adjusted to reach the accuracy of 10^{-6} H/atom. A canonical ensemble at 300 K was used to simulate $Ti_{0.5}Al_{0.5}N(0\,0\,1)$ surface (6 atomic layers, surface area 12.536×12.536 Å^2, 216 atoms) interacting with O_2. The MD time step was 1.0 fs and the total simulation time was 2000 fs. The motion of atoms was studied by analyzing atomic trajectories during the MD run, as implemented in the ASAP code [27]. More details can be found elsewhere [21].

3. Experimental

3.1. Deposition of TiAlN

TiAlN coatings were synthesized on Si(1 0 0) substrates using HPPMS in a CC-800/9 CemeCon deposition chamber using a 500×88 mm^2 TiAl sputter target consisting of a Ti plate with inlays of Al. The average power density was approximately 10.5 W cm^{-2} and the substrate temperature was 693 K. More experimental details pertaining to the synthesis of the thin films as well as their composition can be found elsewhere [19]. The thickness of the TiAlN coating used in this study was 1.4 μm. Clean TiAlN surfaces were created under UHV conditions by removal of the native passive layer by means of Ar sputtering with 2 keV for 300 s.

It was proven that no preferential sputtering took place. A corresponding depth profile is provided as supplementary data that show a steady state in the chemical composition after the native surface oxide layer has been removed. Furthermore no chemical changes within the core level spectra of titanium and aluminum could be observed with an increasing of sputter cycles after the initial removal of the surface oxide layer. The generated surface is thereby similar to one that is formed by the sputter deposition process without forming reaction products due to exposure to residual gas and/or atmosphere [19].

3.2. Investigation of oxygen chemisorption by means of XPS

The chemisorption of oxygen on the surface was induced by a controlled exposure to oxygen under UHV conditions at a base pressure of lower than 1×10^{-4} mPa. The temporal evolution of the surface composition at room temperature and at a defined oxygen partial pressure was investigated by means of XPS, as previously described in [19], with a 128 channel electron detector (Argus, Oxford Instruments, Taunusstein, Germany) and operated at a pass energy of 25 eV for high resolution spectra. For time resolved spectra the pass energy was raised to 100 eV to increase the observed energy range of the 128 channel detector as discussed below. The principal energy resolution of the spectrometer could be estimated by a calibration based on Ag $3d_{5/2}$ that gives full width half maximum values of 0.65 for 25 eV pass energy and 0.8 for 100 eV pass energy, respectively. The take-off angle of the photoelectrons was 60° with respect to the surface normal which leads to an information depth of about 3 nm [28]. During oxygen dosing the pressure in the XPS chamber was increased from the base pressure of $p_{base} = 1 \times 10^{-4}$ to $p_{dosing} = 1 \times 10^{-3}$ mPa, which resulted in an oxygen partial pressure of $pO_2 = 0.9 \times 10^{-3}$ mPa. XPS data of the O 1s, Ti 2p, N 1s, and Al 2p core level peaks were successively measured in such a way that the 128 channels of the electron detector covered the whole core level peak ("snapshot mode"). The acquisition time per core level spectrum was 4 s to achieve a satisfying signal to noise ratio. The time resolution of the experiment was 26 s per loop cycle resulting from the time needed to acquire the core level spectra (4 s per element) and switch the observed energy range of the photoelectron analyzer (2.5 s after each acquisition). The pass energy was set to 100 eV to cover the energy range of the corresponding core level spectra which leads to an overall energy range of 14.3 eV that is covered by the 128 channels of the detector. This procedure allowed us to follow the temporal evolution of the elemental composition of the surface near region.

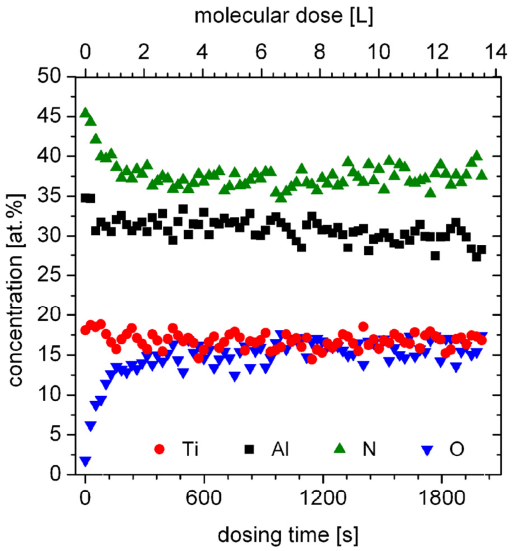

Fig. 1. Temporal evolution of surface chemistry for the surface near region of TiAlN measured *in situ* by "snapshot mode" XPS during O_2 dosing.

As the time resolution of the spectroscopy was in the order of 26 s, it is interesting to estimate how many monolayers are formed in a corresponding time scale. The rate of oxygen adsorption $\dot{N}$ can be estimated from the kinetic theory of ideal gases [29]:

$$\dot{N} = \frac{p \times A}{\sqrt{2\pi m k_B T}}, \quad (1)$$

where, $\dot{N}$ is the number of molecules hitting a surface area per unit of time, p is the oxygen partial pressure of 1×10^{-3} mPa, A designates the surface area covered by one oxygen molecule (0.1×10^{-18} m^2), m is the mass of the oxygen molecule (5.31×10^{-26} kg), k_B is the Boltzman constant, and T is the temperature (300 K). We assumed the sticking coefficient of 1. This results in the chemisorption of 2.7×10^{-3} oxygen monolayers per second. Thus, about 370 s are necessary for the formation of an oxygen monolayer, which allow us to resolve the chemisorption process over time.

4. Results and discussion

4.1. Temporal evolution of surface chemistry

The temporal evolution of surface chemistry of TiAlN during oxygen exposure as investigated by means of XPS is presented in Fig. 1 as a function of dosing time in seconds and also molecular dose in Langmuir (1 L = 1 Torr 1 μs). The major changes occur within the first 150 s. After about 300 s the surface concentration of oxygen reaches an almost constant value of about 15%. Comparing the approximated monolayer adsorption time for oxygen molecules of 360 s this indicates that the first monolayer of chemisorbed oxygen inhibits the three dimensional growth of an oxide film at the given oxygen partial pressure and temperature.

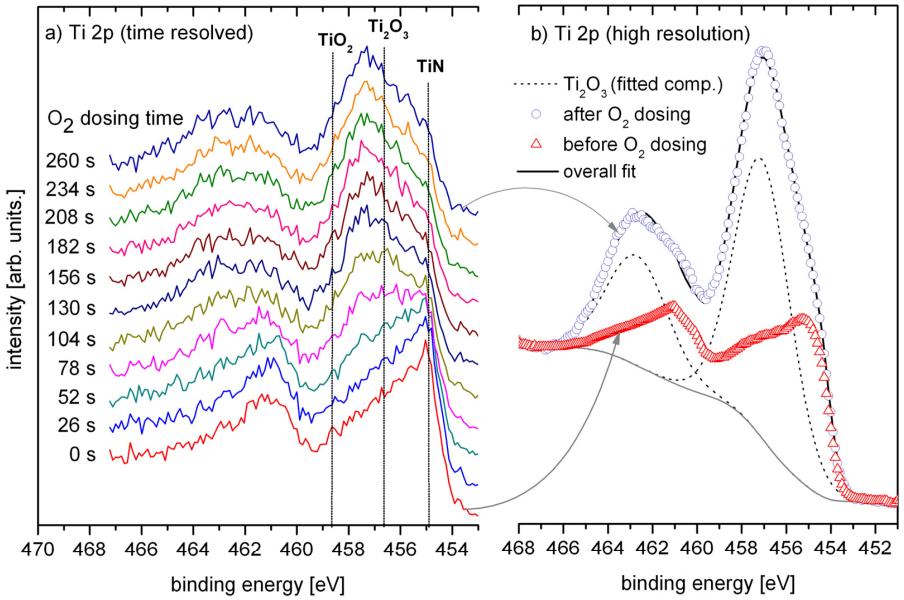

Fig. 2. (a) Ti 2p core level XPS spectra monitored in "snapshot mode" during O_2 dosing. Note the signal to noise ratio is comparatively poor due to the short acquisition time of 4 s per spectrum. (b) Ti 2p core level XPS spectra before (triangles) and after (circles) O_2 dosing with fitted Ti_2O_3 contributions. Corresponding spectra are indicated by the curved arrows, with the limitation that the spectrum plotted with circle symbol represents the situation after the end of the dosing experiment and not after 260 s.

As oxygen is chemisorbed on TiAlN a concomitant decrease in *N* concentration is measured. In the early stage of oxygen dosing a sharp decrease of the aluminum concentration is observed, while the titanium concentration remains constant. As shown by the time resolved elemental spectra and *ab initio* MD simulations (see below) this initial increase in the Ti/Al-concentration is assigned to the preferential formation of a Ti_2O_3 surface monolayer which shields the underlying material. This may lead to a sudden drop in the aluminum concentration as its XPS signal is impeded by the formation of Ti_2O_3. Within the first 300 s a preferential formation of oxidic titanium species is leading to a converging surface chemistry. For the given temperature and oxygen partial pressure no significant changes of the TiAlN composition after 900 s were observed.

The temporal evolution of the Ti 2p core level XPS spectra during oxygen dosing is given in Fig. 2(a). Within the first minutes of the oxygen exposure, nitridic titanium species react to form Ti_2O_3. After about 180 s no significant further changes in the peak shape of the Ti 2p core level spectra were observed. This is consistent with the temporal evolution of surface chemistry (see Fig. 1). This observation implies a preferential reaction of titanium with oxygen during the initial chemisorption process.

High resolution Ti 2p core level XPS spectra before and after oxygen dosing allow for the deconvolution of the oxidic and nitridic peak contributions as shown in Fig. 2(b). The purely nitridic Ti 2p peak is characterized by a strong asymmetry with a tail reaching to higher binding energies. This may be assigned to the screening of core orbitals by valence band electrons for conductive materials [30], which makes a modeling of the Ti 2p peak in TiAlN via a fit of synthetic compounds difficult [31,32]. Thus we used the Ti 2p spectrum that was obtained prior to oxygen dosing as a reference spectrum, which was introduced as the nitridic Ti 2p component into the Ti 2p spectrum obtained after oxygen dosing. To represent the oxidic Ti_2O_3 contributions, additional synthetic compounds of the shape GL (30) (Gaussian (30%)–Lorentzian (70%)) [33] were fitted as shown in Fig. 2(b) which allows for obtaining the contribution of oxidic and nitridic titanium compounds, via the peak areas. The Ti 2p core level spectrum still shows contributions of TiN after the chemisorption of oxygen, as the information depth of the XPS measurement is in the order of a few nanometers. It can be assumed that a three dimensional oxide layer forms at increased oxygen partial pressures [19] and/or significantly elevated temperatures [2].

The elemental compositions of the TiAlN sample were obtained from high resolved XPS spectra before and after oxygen dosing and are given in Table 1. As surface contaminations were removed by the argon sputtering prior to the experiments, as described in Section 3.1, a quantitative analysis of the surface composition is possibly based on the XPS results.

Considering the anion to cation ratio, an almost stoichiometric TiAlN composition before oxygen dosing could be observed while after dosing non-metal over stoichiometry is observed which is in agreement with *ab initio* calculations on TiAlNO [34]. In the final state of the oxide formation reaction at low oxygen partial pressure, the observed concentration of Ti(III) bound to oxygen would correspond to an oxygen concentration of 14.4 at.% if a pure Ti_2O_3 layer would cover the surface. The observed difference of 3.6% is assigned to the formation of aluminum oxide. It is interesting to note that the depth information is sufficient to identify the nitridic contribution of the Ti 2p peak, indicating that the decrease in oxygen uptake observed in Fig. 1 after around 150 s is due to passivation and not due to insufficient depth resolution in XPS.

Atmospherically exposed TiAlN films further oxidize up to Ti(IV), as shown in a previous study [19]. Within this study, no formation of TiO_2 could be detected based on the XPS data. Thus we suggest that higher partial pressures of oxygen and/or the presence of water adsorbates are necessary to form TiO_2 on TiAlN.

4.2. *Ab inito molecular dynamics studies*

Fig. 3 shows the interaction of the $Ti_{0.5}Al_{0.5}N(0\,0\,1)$ surface with four O_2 molecules, as obtained by *ab initio* MD studies. It is evident that a dissociative adsorption of O_2 occurs: individual O atoms

Table 1
Elemental composition of the TiAlN sample.

	Ti 2p (at.%)		Al 2p (at.%)	N 1s (at.%)	O 1s (at.%)
	Ti_2O_3	TiN			
Before O_2 dosing	–	19	31	47	<3
After O_2 dosing (14 L, 35 min)	9.6	6.4	29	37	18

interact with metal atoms, but never with N. Ti sites are preferred over Al sites. There are four types of metal —O bonds formed: (i) single Ti—O bond (referred to as Ti1), (ii) double Ti—O bond (referred to as Ti3), (iii) triple Ti—O bond (referred to as Ti2) and (iv) single Al—O bond (referred to as Al1). As discussed previously [21], Ti escapes from the $Ti_{0.5}Al_{0.5}N(0\,0\,1)$/O interface layer, which is induced by an increased Ti—O coordination (double and triple bonds) compared to single Ti—O bonds. This generates Ti vacancies in the $Ti_{0.5}Al_{0.5}N(0\,0\,1)$/O interface layer. Based on the bond length and coordination data, these triple Ti—O bonds are consistent with TiO_2 as well as corundum Ti_2O_3 [21,35]. Hence, it is reasonable to assume that the O adsorption induces Ti extraction and the associated vacancy formation enables and constitutes the initial stage of oxide formation. This is consistent with the XPS data presented above.

To evaluate the kinetics of O_2 on the $Ti_{0.5}Al_{0.5}N(0\,0\,1)$ surface, we plot the displacement of Ti1, Ti2, Ti3, and Al1 as a function of time in Fig. 4. Clearly, O_2 induces a displacement of metal atoms on TiAlN(0 0 1). The fastest process is triple Ti—O bond and Ti vacancy formation (Ti2), followed by single Ti—O bond formation (Ti1). The slowest processes are double Ti—O bond and Ti vacancy formation (Ti3) as well as single Al—O bond formation (Al1). These data are consistent with the temporal evolution of the chemical composition presented in Fig. 1 and the corresponding binding energies in Fig. 2. We propose that the kinetics of the initial chemisorption of oxygen on TiAlN is governed by triple Ti—O bond and Ti vacancy formation. This may be understood based on the electronic structure of TiAlN [11]. TiAlN appears metallic since the Fermi level is occupied.

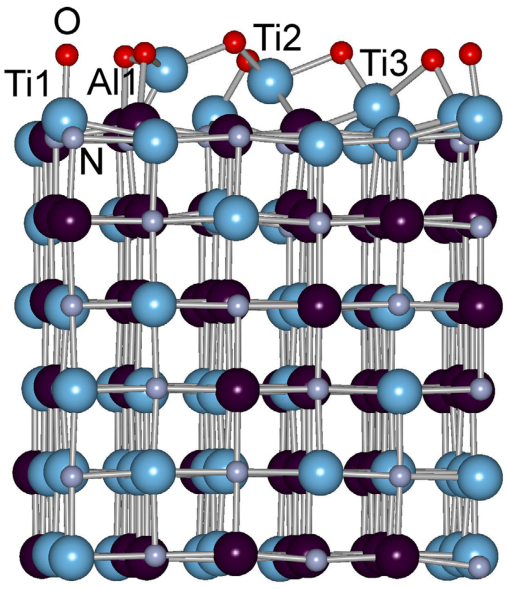

Fig. 3. MD snapshot of $Ti_{0.5}Al_{0.5}N(0\,0\,1)$ interacting with four O_2 molecules at 300 K after 2000 fs. Nearest neighbours are connected. Some surface atoms (Ti1, Ti2, Ti3, and Al1) are additionally marked due to their importance in kinetic processes.

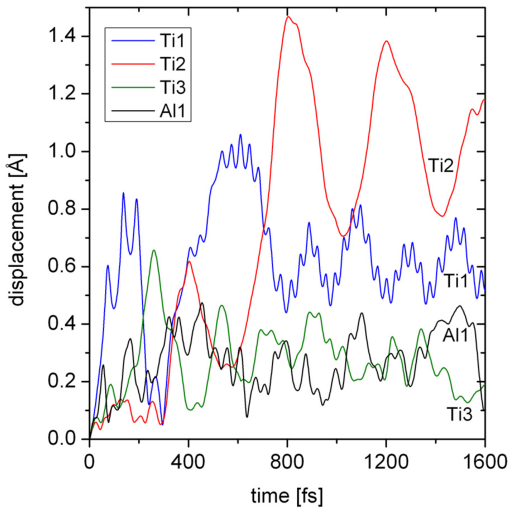

Fig. 4. Displacement of Ti and Al atoms, marked in Fig. 3, as a function of time.

There are Ti d–N p and Al p–N p hybridizations present. The following mechanism is proposed. As Ti d states dominate the Fermi level, it is conceivable that Ti atoms are more mobile as Al atoms since they occupy deeper core states. This is consistent with diffusion barrier on TiN(0 0 1): 0.40 eV for Ti and 0.47 eV for Al [36]. More support for preferred Ti–O interactions can be gained from the effective charge analysis. We performed the Mulliken populations analysis [37] and it should be noted that the calculated effective charge is only proportional to the formal charge. Clean $Ti_{0.5}Al_{0.5}N(0\,0\,1)$ possesses the following effective charge: from +0.7 to +0.8 for Ti, from +0.8 to +0.9 for Al and from −0.6 to −0.9 for N. As four O_2 molecules react with $Ti_{0.5}Al_{0.5}N(0\,0\,1)$ during the *ab initio* MD run, the largest changes occur for surface Ti atoms, increasing their formal charge up to 1.0. Simultaneously, oxygen reaches the effective charge values of −0.5 to −0.6. This indicates that there is a transfer of Ti valence electrons to adsorbed oxygen, which is consistent with our XPS data.

5. Conclusions

According to the results that were obtained within this work, we propose that oxygen chemisorption on TiAlN results in the formation of Ti_2O_3 like bonding and Ti vacancy formation, while the reaction of aluminum with oxygen plays a subordinated rule. This interpretation is based on both experimental data and *ab initio* MD simulation results. The initial step is dissociative adsorption of oxygen, as the electron density of Ti at the Fermi level of the solid surface is larger than that of the Al atoms, the oxygen preferentially coordinates to Ti: first as Ti—O single bonds followed by double- and three-fold coordination of Ti. This process creates Ti vacancies in the TiAlN surface along with the displacement of surface titanium atoms into top layer positions. The formation of Ti_2O_3 inhibits the further transfer of electrons to adsorbed oxygen, which suppresses

the reaction of aluminum with oxygen. These results are relevant for basic understanding of initial stages of oxidation, surface diffusion and nucleation on reaction layers of transition metal nitrides upon exposure to residual, and environmental gases.

Acknowledgement

The authors gratefully acknowledge the financial support of the German Research Foundation (DFG) within the transregional collaborative research center TR 87/1-2010 "Pulsed high power plasmas for the synthesis of nanostructured functional layers" (SFB-TR 87).

Appendix A. Supplementary data

Supplementary data associated with this article can be found, in the online version, at http://dx.doi.org/10.1016/j.apsusc.2013.11.091.

References

[1] W.D. Münz, Titanium aluminum nitride films: a new alternative to TiN coatings, J. Vac. Sci. Technol. A 4 (1986) 2717–2725.
[2] D. McIntyre, J.E. Greene, G. Håkansson, J.E. Sundgren, W.D. Münz, Oxidation of metastable single-phase polycrystalline $Ti_{0.5}Al_{0.5}N$ films: kinetics and mechanisms, J. Appl. Phys. 67 (1990) 1542–1553.
[3] P.H. Mayrhofer, A. Horling, L. Karlsson, J. Sjolen, T. Larsson, C. Mitterer, L. Hultman, Self-organized nanostructures in the Ti–Al–N system, Appl. Phys. Lett. 83 (2003) 2049–2051.
[4] R. Cremer, K. Reichert, D. Neuschutz, A composition spread approach to the optimization of (Ti,Al) N hard coatings deposited by DC and bipolar pulsed magnetron sputtering, Surf. Coat. Technol. 142 (2001) 642–648.
[5] A. Horling, L. Hultman, M. Oden, J. Sjolen, L. Karlsson, Thermal stability of arc evaporated high aluminum-conteht $Ti_{1-x}Al_xN$ thin films, J. Vac. Sci. Technol. A 20 (2002) 1815–1823.
[6] R. Prange, R. Cremer, D. Neuschutz, Plasma-enhanced CVD of (Ti,Al) N films from chloridic precursors in a DC glow discharge, Surf. Coat. Technol. 133 (2000) 208–214.
[7] J.Y. Rauch, C. Rousselot, N. Martin, Structure and composition of TixAl1-xN thin films sputter deposited using a composite metallic target, Surf. Coat. Technol. 157 (2002) 138–143.
[8] K. Kutschej, P.H. Mayrhofer, M. Kathrein, P. Polcik, R. Tessadri, C. Mitterer, Structure, mechanical and tribological properties of sputtered $Ti_{1-x}Al_xN$ coatings with $0.5 <= x <= 0.75$, Surf. Coat. Technol. 200 (2005) 2358–2365.
[9] G. Greczynski, J. Lu, M. Johansson, J. Jensen, I. Petrov, J.E. Greene, L. Hultman, Selection of metal ion irradiation for controlling $Ti_{1-x}Al_xN$ alloy growth via hybrid HIPIMS/magnetron co-sputtering, Vacuum 86 (2012) 1036–1040.
[10] P.H. Mayrhofer, F.D. Fischer, H.J. Boehm, C. Mitterer, J.M. Schneider, Energetic balance and kinetics for the decomposition of supersaturated $Ti_{1-x}Al_xN$, Acta Mater. 55 (2007) 1441–1446.
[11] P.H. Mayrhofer, D. Music, J.M. Schneider, Influence of the Al distribution on the structure, elastic properties, and phase stability of supersaturated $Ti_{1-x}Al_xN$, J. Appl. Phys. 100 (2006) 094906.
[12] P.H. Mayrhofer, D. Music, J.M. Schneider, Ab initio calculated binodal and spinodal of cubic $Ti_{1-x}Al_xN$, Appl. Phys. Lett. 88 (2006) 071922.
[13] F. Rovere, D. Music, S. Ershov, M. to Baben, H.G. Fuss, P.H. Mayrhofer, J.M. Schneider, Experimental and computational study on the phase stability of Al-containing cubic transition metal nitrides, J. Phys. D 43 (2010) 035302.
[14] B. Alling, A.V. Ruban, A. Karimi, O.E. Peil, S.I. Simak, L. Hultman, I.A. Abrikosov, Mixing and decomposition thermodynamics of c-$Ti_{1-x}Al_xN$ from first-principles calculations, Phys. Rev. B 75 (2007) 045123.
[15] A. Horling, L. Hultman, M. Oden, J. Sjolen, L. Karlsson, Mechanical properties and machining performance of $Ti_{1-x}Al_xN$-coated cutting tools, Surf. Coat. Technol. 191 (2005) 384–392.
[16] K. Kawata, H. Sugimura, O. Takai, Characterization of multilayer films of Ti-Al–O–C–N system prepared by pulsed d.c. plasma-enhanced chemical vapor deposition, Thin Solid Films 390 (2001) 64–69.
[17] K. Bobzin, R. Nickel, N. Bagcivan, F.D. Manz, PVD – coatings in injection molding machines for processing optical polymers, Plasma Processes Polym. 4 (2007) S144–S149.
[18] D. Music, D. Lange, L. Raumann, M. to Baben, F. von Fragstein, J.M. Schneider, Polypropylene–MAlN (M=Ti, Cr) interface interactions, Surf. Sci. 606 (2012) 986–989.
[19] C. Gnoth, C. Kunze, M. Hans, M. to Baben, J. Emmerlich, J.M. Schneider, G. Grundmeier, Surface chemistry of TiAlN and TiAlNO coatings deposited by means of high power pulsed magnetron sputtering, J. Phys. D 46 (2013) 084003.
[20] A. Tempez, A. Bensaoula, A. Schultz, Characterization of TiAlN thin film annealed under O_2 by in situ time of flight direct recoil spectroscopy/mass spectroscopy of recoiled ions and ex situ x-ray photoelectron spectroscopy, J. Vac. Sci. Technol. A 20 (2002) 1320–1326.
[21] D. Music, J.M. Schneider, Ab initio study of $Ti_{0.5}Al_{0.5}N(0\,0\,1)$ — residual and environmental gas interactions, New J. Phys. 15 (2013) 073004.
[22] H.C. Barshilia, K.S. Rajam, Raman spectroscopy studies on the thermal stability of TiN, CrN, TiAlN coatings and nanolayered TiN/CrN, TiAlN/CrN multilayer coatings, J. Mater. Res. 19 (2004) 3196–3205.
[23] T. Ozaki, H. Kino, Efficient projector expansion for the *ab initio* LCAO method, Phys. Rev. B 72 (2005) 045121.
[24] P. Hohenberg, W. Kohn, Inhomogeneous electron gas, Phys. Rev. 136 (1964) B864.
[25] T. Ozaki, Variationally optimized atomic orbitals for large-scale electronic structures, Phys. Rev. B 67 (2003) 155108.
[26] J.P. Perdew, K. Burke, M. Ernzerhof, Generalized gradient approximation made simple, Phys. Rev. Lett. 77 (1996) 3865.
[27] D. Music, F. Hensling, T. Pazur, J. Bednarcik, M. Hans, V. Schnabel, C. Hostert, J.M. Schneider, Bonding and elastic properties of amorphous $AlYB_{14}$, Solid State Commun. 169 (2013) 6–9.
[28] J.F. Watts, J. Wolstenholme, An Introduction to Surface Analysis by XPS and AES, Wiley, 2003.
[29] P.W. Atkins, J. De Paula, M. Bär, Physical Chemistry, Oxford University Press, 2002.
[30] L. Porte, L. Roux, J. Hanus, Vacancy effects in the X-Ray photoelctron-spectra of TiN_x, Phys. Rev. B 28 (1983) 3214–3224.
[31] N.C. Saha, H.G. Tompkins, Titanium nitride oxidation chemistry: an X-Ray photoelctron-spectroscopy study, J. Appl. Phys. 72 (1992) 3072–3079.
[32] A. Schuler, P. Oelhafen, In situ core-level and valence-band photoelectron spectroscopy of reactively sputtered titanium aluminum nitride films, Phys. Rev. B 63 (2001) 115413.
[33] M.C. Biesinger, L.W.M. Lau, A.R. Gerson, R.S.C. Smart, Resolving surface chemical states in XPS analysis of first row transition metals, oxides and hydroxides: Sc, Ti, V, Cu and Zn, Appl. Surf. Sci. 257 (2010) 887–898.
[34] M. to Baben, L. Raumann, J.M. Schneider, Phase stability and elastic properties of titanium aluminum oxynitride studied by ab initio calculations, J. Phys. D 46 (2013) 084002.
[35] C.E. Rice, W.R. Robinson, High-temperature crystal-chemistry of Ti_2O_3–structural-changes accompanying semiconductor-metal transition, Acta Crystallogr. Sect. B 33 (1977) 1342–1348.
[36] B. Alling, P. Steneteg, C. Tholander, F. Tasnadi, I. Petrov, J.E. Greene, L. Hultman, Configurational disorder effects on adatom mobilities on $Ti_{1-x}Al_xN(0\,0\,1)$ surfaces from first principles, Phys. Rev. B 85 (2012) 245422.
[37] R.S. Mulliken, Electronic population analysis on LCAO-MO molecular wave functions, J. Chem. Phys. 23 (1955) 1833–1840.

Christian Kunze [a]
Denis Music [b]
Moritz to Baben [b]
Jochen M. Schneider [b]
Guido Grundmeier [a,*]
[a] *Technical and Macromolecular Chemistry, University of Paderborn, Warburger Str. 100, 33098 Paderborn, Germany*
[b] *Materials Chemistry, RWTH Aachen University, Kopernikusstr. 10, 52074 Aachen, Germany*

[*] Corresponding author. Tel.: +49525160 5700; fax: +49525160 6244.
E-mail address: g.grundmeier@tc.uni-paderborn.de (G. Grundmeier)

26 July 2013

1 October 2013

17 November 2013
Available online 24 November 2013

Temporal Evolution of Oxygen Chemisorption on TiAlN

Christian Kunze[a], *Denis Music*[b], *Moritz to Baben*[b], *Jochen M. Schneider*[b], *Guido Grundmeier*[a,*]

[a] Technical and Macromolecular Chemistry, University of Paderborn, Warburger Str. 100, 33098 Paderborn, Germany.

[b] Materials Chemistry, RWTH Aachen University, Kopernikusstr. 10, 52074 Aachen, Germany.

*corresponding author: g.grundmeier@tc.uni-paderborn.de

Supplementary data

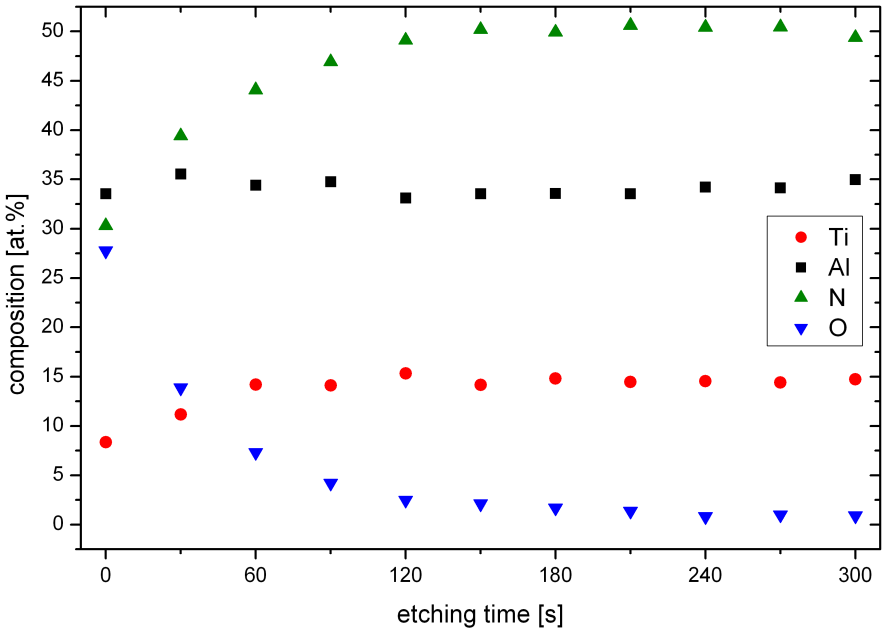

Figure 1: Depth profile of the TiAlN coating used within this work during Ar sputtering with 2 keV. The sputter rate can be estimated based on a calibration on SiO_2 to about 4 nm/minute.

3.5 Surface chemistry and nonadecanoic acid adsorbate layers on TiO_2(100) surfaces prepared at ambient conditions

Christian Kunze, Boray Torun, Ignacio Giner, Guido Grundmeier
Surface Science, 606, **2012**, 1527-1533.

The scientific work and discussion was coordinated and consolidated by CK under supervision of GG.
The manuscript was prepared by CK; IG contributed to the introduction of the manuscript.
Graphics within the manuscript were re-worked by BT.
TiO_2 single crystals were prepared by CK, BT and IG.
AFM measurements were performed by CK.
LEED measurements were performed by CK and IG, LEED data evaluation was performed by IG.
XPS measurements and data evaluation were performed by CK.
The manuscript was revised by GG.

Within this work the adsorption of carboxy-functional molecules (nonadecanoic acid) on atmospherically prepared TiO_2(100) single crystalline surfaces has been investigated. The presented approach aims in a molecular understanding of adsorbate formation on titania surfaces by applying a model system of TiO_2 single crystal surfaces and a carboxylic acid as a model adsorbate. It could be shown that the atmospherically prepared TiO_2(100) substrates exhibit a well ordered structure that is characterized by an OH surface termination. These substrates weakly interact with carboxy-functional groups leading to an unordered monolayer of nonadecanoic acid which replaces the native carbon contamination which originates from molecules that are present in the ambient atmosphere.

Surface Science 606 (2012) 1527–1533

Contents lists available at SciVerse ScienceDirect

Surface Science

journal homepage: www.elsevier.com/locate/susc

Surface chemistry and nonadecanoic acid adsorbate layers on TiO_2(100) surfaces prepared at ambient conditions

C. Kunze, B. Torun, I. Giner, G. Grundmeier *

University of Paderborn, Institute for Technical and Macromolecular Chemistry, Warburger Str. 100, 33098 Paderborn, Germany

ARTICLE INFO

Article history:
Received 21 February 2012
Accepted 30 May 2012
Available online 6 June 2012

Keywords:
Titanium dioxide
Single crystal
Surface adsorbates
Atmospheric preparation
XPS
Hydroxyl termination
Nonadecylcarboxylic acid
AFM

ABSTRACT

The surface and adsorbate chemistry of the TiO_2(100) surface prepared at high temperatures and ambient conditions were studied by means of angle resolved X-ray photoelectron spectroscopy (AR-XPS), Low Energy Electron Diffraction (LEED) and Atomic Force Microscopy (AFM) based nanoshaving studies. The TiO_2(100) surface shows a 1×1 structure with a 1×3 superstructure assigned to surface defects. A significant hydroxide surface concentration was revealed by means of AR-XPS measurements. The adsorbate formation of nonadecanoic acid (NDCA) from ethanolic solution led to disordered sub-monolayer surface coverage. The weak interaction between the carboxylic acid group and the TiO_2 surface is assumed to be a combination of the neutral to acid behavior of the TiO_2 surface and the stable hydroxide surface layer created under ambient conditions.

1. Introduction

Titanium dioxide (TiO_2) plays a crucial role for modern technical applications such as the design of new catalysts [1–3] or biomaterials [4–6]. TiO_2 particles in rutile or anatase phase are widely used inorganic pigments. Moreover, the use of TiO_2 for photocatalytical processes [7–9] and as semiconductor electrode for dye sensitized solar cells [10–12] have led to a great scientific interest in the surface chemistry and surface physics of TiO_2.

For an optimal color effect the desired particle size is in the range of 250 to 400 nm. The physical properties of TiO_2 particles (e.g. its transparency at visible wavelengths and its large index of refraction) have made it the world's most widely used white pigment for polymers [13]. The processability and functional properties of such pigments strongly depend on the particle–particle interactions and the surface chemistry of the particles.

As the interactions between small particles are mostly driven by van der Waals interactions, hydrogen bonding and capillarity forces, the chemical and physical structures of the particle surface are of outmost importance. The TiO_2 surface has been intensively studied by Diebold et al. [14,15] and Henderson et al. [16] under UHV conditions. On single crystals prepared under UHV conditions Diebold et al. found oxygen depletion resulting in the formation of surface defects [14,15]. Different water adsorption behavior was reported by Henderson et al. for different TiO_2 crystal orientations [16]. However, as such single crystalline surfaces were prepared and analyzed under UHV conditions the corresponding studies are not representative for TiO_2 surfaces prepared under ambient conditions of high water and oxygen activity.

For the prediction of the behavior of particle collectives under ambient conditions the knowledge of the exact adsorbate chemistry on the considered surfaces plays a crucial role towards understanding force interactions between solids. The adsorption of small molecules such as water, alcohols or acids has been intensively studied within the last years mostly under UHV conditions [17–20]. In contrast, few studies showed the adsorption of larger molecules under atmospheric conditions [21,22]. In both cases, the possibility of obtaining well-defined stepped TiO_2(100) surfaces with monoatomically flat terraces promoted the use of this crystal orientation as model system.

Adsorption studies under UHV conditions have been mostly performed on the (110) surface [14,23]. The preparation of these surfaces in UHV conditions results in the formation of well-ordered TiO_2 surfaces free of surface hydroxides. The adsorption of different molecules like carboxylic acids [23,24], alcohols [25,26], and aldehydes [27,28], onto the (110) surface has been widely studied. The adsorption mechanism of a carboxylic acid onto the surface has been elucidated and occurs via preferential binding to the five-fold Ti^{4+} in a bidentate mode. Moreover, the adsorption of the carboxylic acid leads to the formation of a hydroxide group on the bridging oxygen of the lattice [29,30].

* Corresponding author. Tel.: +49 5251 605700; fax: +49 5251 60 3244.
E-mail address: g.grundmeier@tc.uni-paderborn.de (G. Grundmeier).

0039-6028/$ – see front matter © 2012 Elsevier B.V. All rights reserved.
doi:10.1016/j.susc.2012.05.025

When discussing force interactions between particles under ambient conditions in addition to van der Waals interactions, capillarity forces also have to be considered. Butt et al. investigated capillarity forces between particle modified AFM tips and surfaces of different roughness as a function of relative humidity [31]. They reported that an influence of relative humidity on the adhesion force was only detectable on hydrophilic surfaces. Hashimoto et al. studied the influence of UV light on the wettability properties of TiO_2 single crystals and observed a reversible surface wettability conversion based on a photo induced reduction of Ti^{4+} to Ti^{3+} [32].

Whitesides et al. and Nuzzo et al. investigated the adsorbate formation of alkanehydroxamic and carboxylic acids on various oxide covered metals [33]. Due to the higher complexation constant of the hydroxamic acids with metal ions in contrast to carboxylic acids they could observe the formation of self-assembled monolayers. For the combination of the carboxylic acids and amorphous TiO_2 oxide films on Ti no self-assembly process was observed. The authors assigned this behavior mainly to the acid to neutral behavior of the TiO_2 oxide film [33].

Nakamura et al. and Yamamoto et al. showed the preparation of well-defined stepped terrace TiO_2 surfaces via a wet chemical etching procedure followed by an annealing step in air [34–36]. Lu et al. also showed the formation of TiO_2 surface with well stepped terraces by means of a modified procedure, a manual polishing of the samples, followed by sonication in pure water and annealing.

In this paper, the main focus was set on the investigation of the adsorption of model molecules to enable a fundamental understanding of particle–wall interactions under ambient conditions in the presence of adsorbates. As a model molecule to simulate contaminations from ambient atmosphere nonadecanoic acid (NDCA) was chosen for three main reasons. Firstly, the carboxylic acid group mimics the chemical functionalities of contaminations which are present in ambient conditions, secondly the aliphatic chain is of defined chemical composition that gives an intense carbon signal in XPS experiments and finally allows the detection of a height contrast in AFM based nanoshaving investigations. To correlate the properties of single crystalline surfaces of TiO_2 with more complex TiO_2 particle surfaces we followed the approach of an atmospheric preparation of the single crystalline surface. The characterization of the bare and adsorbate covered surfaces was performed microscopically by means of Atomic Force Microscopy (AFM) and spectroscopically by means of Low Energy Electron Diffraction (LEED) and angle resolved X-ray photoelectron spectroscopy (XPS).

2. Experimental

2.1. Materials and chemicals

Rutile TiO_2 single crystals in (100) orientation of 10 mm × 10 mm × 0.5 mm size grown by the Verneuil process were obtained from Mateck GmbH (Juelich, Germany). All chemicals and solvents were of p.a. grade (analytical reagent grade) and used without any further purification unless mentioned otherwise. Ethanol, used as a solvent and for general cleaning purposes, was purchased from VWR International. Nonadecanoic acid (97%) was obtained from Fluka (Fluka, Germany). Hydrofluoric acid (40%) was obtained from Merck KGa (Merck, Germany). Water was obtained from an Ultraclear TWF (SG Wasseraufbereitung, Barsbüttel, Germany) system with a maximum electrical conductance of 0.055 $\mu S \cdot cm^{-1}$.

2.2. Atmospheric preparation of TiO_2(100) single crystalline surfaces

TiO_2(100) single crystalline surfaces which are stable under ambient conditions were prepared from one-side polished TiO_2(100) rutile single crystals by a wet chemical etching procedure followed by an annealing step according to the preparation route proposed by Nakamura et al. [34] and Yamamoto et al. [35]. To avoid contamination of the crystal during the preparation, etching was performed in a PTFE vessel.

As a pre-cleaning step, the TiO_2 crystals were sonicated in ultrapure water. For the preparation of single crystalline TiO_2 surfaces, the crystals were etched in 20% HF solution for 20 min. After the etching process the crystals were intensively rinsed with ultrapure water and dried in a stream of pure nitrogen gas.

After the etching step the crystals were directly transferred into a tube furnace consisting of a horizontal Al_2O_3 tube and annealed at 680 °C for 48 to 72 h in ambient air. To avoid mechanical stress in the crystal as well in the annealing tube a heating and cooling rate of 3 °C/min was chosen, resulting in a ramping time of about 3.5 h. After preparation the crystals were checked for surface quality by means of AFM.

2.3. Adsorption of NDCA monolayers on TiO_2 single crystalline surfaces

For studies of adsorbate formation on single crystalline TiO_2 surfaces nonadecanoic acid (NDCA, $C_{18}H_{37}COOH$) was chosen as a model molecule to study the interaction of carboxylic acids with the TiO_2 surface. The freshly prepared TiO_2 single crystals were immersed into a 1 mM ethanolic solution of NDCA for 12–16 h, according to typical preparation methods of self-assembled monolayers [37]. After the adsorption step crystals were rinsed with ethanol and dried in a nitrogen stream.

2.4. Analytical methods

2.4.1. AFM instrumentation

AFM measurements were performed by means of a JPK Nanowizard II Ultra (JPK Instruments AG, Berlin, Germany) equipped with an anti-noise- and anti-vibration-box under ambient conditions in air. Contact mode imaging was applied for bare TiO_2 single crystal surfaces. AC mode scanning was performed on TiO_2 surfaces with adsorbed molecules. Measurements in contact mode were performed at constant forces ranging from 2 to 5 nN. Imaging in AC mode was done at constant amplitude, which was damped to 98–90% of the free-air amplitude. The scan speed was between 1 and 2 μm per second, at a scan resolution of 512 × 512 pixels. For contact mode imaging rectangular silicon cantilevers type DP17 (obtained from Mikromash, Estonia) with a pyramidal shaped silicon tip were used. AC mode imaging, as well as Nanoshaving experiments was performed with NSC15 cantilevers (obtained from Mikromash, Estonia) with a resonance frequency of about 320 kHz in air and a force constant of 40 $N\,m^{-1}$. A similar experimental approach was followed by Grundmeier et al. for studies of organophosphonic acid self-assembled monolayers on Al_2O_3 surfaces [38].

2.4.2. AFM topographic imaging

The etching and annealing process as described above led to well defined surface structures (see Fig. 1) with about 150–250 nm wide atomically flat terraces. The step height between the terraces was 500 pm which corresponds to one rutile unit cell (c = 459 pm) [39].

2.4.3. Contact angle experiments

Contact angle experiments were performed by means of a SCA 20 (DataPhysics Instruments GmbH, Filderstadt, Germany) system at ambient conditions with ultrapure water as liquid. To minimize the influence of gravity on the drop shape the drop volume was set to 5 μl during all experiments.

2.4.4. XPS instrumentation

The TiO_2 crystals were directly transferred into the UHV system after the annealing step, to avoid further contamination from the laboratory atmosphere. The investigated "as prepared" surfaces were taken out of the oven after annealing when the crystals were cooled down to about 100 °C and were directly mounted on the UHV sample holder. The time

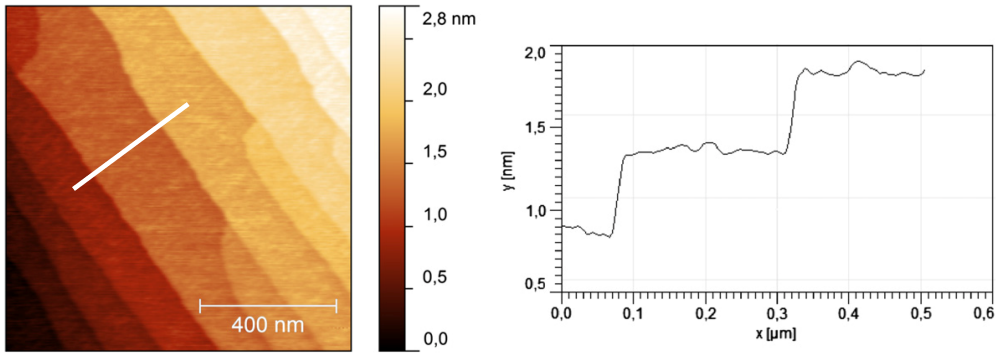

Fig. 1. AFM topography image of the TiO_2(100) single crystalline surface with about 250 nm wide atomically flat terraces (left). Cross section of the marked area (right).

needed to transfer the bare crystal from the annealing oven to the UHV load lock was between 5 and 10 min. In the case of SAM coated samples longer exposure times to laboratory conditions can be expected since the transfer into and out of the NDCA solution followed by rinsing and drying has to be considered. Within the UHV system no pretreatment of the sample was performed prior to surface analysis.

XPS measurements were performed by means of an Omicron ESCA+ System (Omicron NanoTechnology GmbH, Germany) with a base pressure of $<2 \cdot 10^{-9}$ mbar. The system is equipped with a hemispherical energy analyzer, the element spectra were recorded at pass energies of 25 eV. For photoelectron excitation a monochromated Al Kα (1486.3 eV) X-ray source with a spot diameter of 600 µm was used. The take-off angle of the detected photoelectrons was varied from 10° to 70° with respect to the surface plane. The calibration of the spectra was performed using the C 1s peak (binding energy, BE = 285 eV) as an internal reference. For data evaluation the CasaXPS [40] software was used. Unless mentioned otherwise all quantification of the XPS data was done by integration of the peaks with regard to the relative sensitivities of the elements. Components within one peak were fitted using a Gaussian–Lorentzian lineshape (30% Lorentzian and 70% Gaussian).

Angle resolved XPS experiments were performed for the analysis of the surface chemistry of the prepared crystals. XPS spectra were recorded at take-off angles of the photoelectrons from 70° to 10° with respect to the surface plane. Estimating the escape depth of the electrons in a solid to λ = ~3 nm (for an Al K_α X-ray source at 1486.3 eV), the probing depth *d* can be calculated as a function of the take-off angle Θ according [41] to Table 1:

$$d = \lambda \sin\Theta \quad (1)$$

The angle resolved spectra presented in Figs. 3, 4, 6 and 7 were normalized by using the O^{2-} peak maximum to create comparable line plots, as the count rate strongly decreases with decreasing take-off angle of the photoelectron. For comparison the measured count rate for the O 1s signal of the bare TiO_2(100) sample at the peak maximum was $120 \cdot 10^3$ counts/s at 70° take-off angle and decreased to $8 \cdot 10^3$ counts/s at 10° take-off angle caused by the typical angular distribution of the emitted photoelectrons.

Table 1
Probing depth as a function of the XPS take-off angle.

Take-off angle Θ/degrees	Probing depth/nm	Equivalent in unit cells TiO_2(100)
70	2.82	6
40	1.93	4
20	1.03	2
10	0.52	1

2.4.5. LEED instrumentation

For LEED experiments Omicron Spectra LEED optics were used at an incident angle of the electrons close to 90° with respect to the surface plane. The beam energy was varied from 80 eV to 120 eV to optimize LEED intensity. The LEED pattern of the surface was simulated and compared with the experimental crystal parameters using the software LEEDpat30 [42].

3. Results and discussion

3.1. Characterization of TiO_2 single crystals prepared under ambient conditions

3.1.1. LEED analysis

The surface and adsorbate structure of TiO_2 surfaces was analyzed by means of LEED experiments after the high temperature annealing step. The corresponding LEED images obtained with a beam energy of 80 eV is shown in Fig. 2 (left image). The (100) surface clearly shows a rectangular LEED pattern (bright points) with several secondary points along the (010) direction. The lattice parameters for TiO_2(100) are a = 4.6 Å and b = 2.6 Å and α = 90° [14]. The evaluation of the pattern and the respective distances led to the conclusion that the superstructure corresponds to a 1×5 reconstruction. Fig. 2 (right image) shows the simulated LEED pattern of the surface created using the software

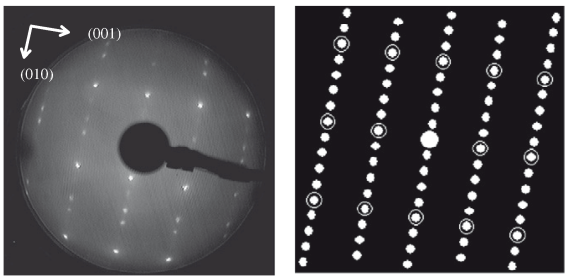

Fig. 2. The observed LEED pattern on the TiO_2(100) (left) surface and the corresponding simulation (right) of the 1×5 reconstruction.

LEEDpat30 [42]. In the literature, 1×1 and 1×3 surface reconstructions have been reported on TiO_2 surfaces prepared in UHV [43,44]. Moreover, due to the controversies regarding the interpretation of the stepped surface of the 1×3 reconstruction, 1×5 and 1×7 reconstructions have as well been reported [45]. Thus the apparent 1×5 reconstruction can be explained as a misinterpretation of the real 1×3 surface structure due to the presence of steps alongside the (010) direction Therefore it can be concluded that the TiO_2(100) single crystal prepared under ambient conditions exhibited a 1×3 surface reconstruction [45]. Nakamura et al. showed a 1×1 reconstruction of the surface when annealing was performed under atmospheric conditions with an oxygen excess [34]. However, Lu et al. observed a reconstruction 1×3 of a TiO_2(100) crystal annealed under atmospheric conditions [46]. The mechanism which leads to this kind of reconstruction under excess of oxygen is still unclear.

3.1.2. X-ray photoelectron spectroscopy (XPS)

The overall element composition of the TiO_2 surface as a function of the take-off angle is presented in Table 2. Except a typical contamination with carbon originating from the atmospheric preparation no elements other than titanium and oxygen were detected. The concentrations of oxygen and titanium are decreasing with decreasing take-off angle of the photoelectrons along with an increasing carbon signal which can be explained by the adsorbate layer of atmospheric contamination on the top of the crystal. Thus for the most surface sensitive XPS experiment at 10° the highest concentration of carbon was observed.

In contrast to a TiO_2 surface prepared in UHV conditions with an O 1s spectrum purely originating from O^{2-} species [23]. The O 1s AR-XP spectra in Fig. 3 confirm that hydroxides, adsorbed water and carboxylic acid groups are present on the oxide surface as the contribution of O 1s electrons with binding energies higher than 530 eV increases with decreasing take off angle.

To analyze the composition of the prepared surface more deeply in terms of titanium and oxygen composition, in Table 3 the ratio of oxygen to titanium is presented as a function of the take-off angle. Moreover, for the analysis of the surface adsorbate layer the oxygen peak is deconvoluted into its chemical contributions. The O 1s spectra consisted of three components assigned to the O^{2-} peak at 529.6 eV and surface OH groups indicated as Ti-OH at 530.8 eV which are created during the annealing under ambient conditions. Furthermore some metal carbonates such as titanium carbonate show binding energies in this region which might occur as residual species from the preparation process [47–49]. An ad-layer of specifically adsorbed water which is stable even under UHV conditions and oxygen associated with organic acids was assigned to a binding energy of 532.3 eV. The contributions of water and oxygen associated with carboxylic acids could not be clearly resolved due to the broad distribution and overlapping of the respective orbital energies [50,51]. Unfortunately a detailed differentiation between these species was not possible because of the undefended nature of the native contamination layer originating from COO and CO–R species.

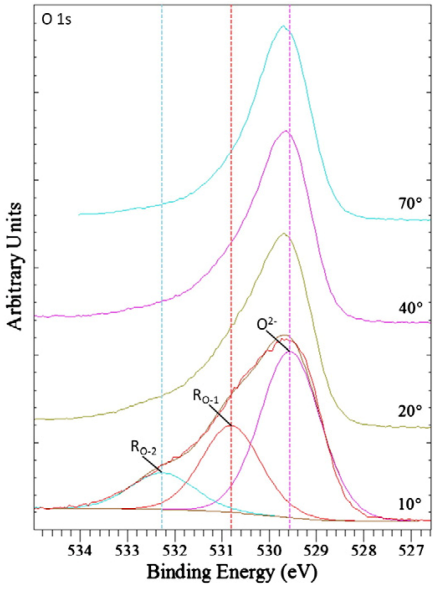

Fig. 3. O 1s spectra of the TiO_2(100) surface. The take-off angles of the photoelectrons are given with respect to the surface plane. For better interpretability the spectra were normalized to the peak maximum as indicated by the vertical line at 529.6 eV.

Sham and Lazarus reported two kinds of surface OH species separated by 1.5 eV and 2.8 eV from the O 1s core level on UHV prepared rutile surfaces assigned to OH "bridge" positions on the surface and alkaline OH "top" positions [52]. However we assume that due to the atmospheric preparation route the different O 1s species cannot be clearly distinguished, as the native ad-layer on the crystal surface leads to different O 1s contributions that have to be considered.

The increasing O_Σ/Ti ratio with decreasing take-off angle implies an oxygen enrichment of the surface which could be supported by the detailed analysis of surface R_{O-1}/O^{2-} and R_{O-2}/O^{2-} contributions indicating a hydroxide terminated surface. The O^{2-}/Ti ratio stays nearly constant with a value of O^{2-}/Ti = 2:1 indicating that the observed excess of oxygen (as indicated by O_Σ/Ti) is mainly due to an adsorbate layer of surface hydroxides as proven by the significantly increasing R_{O-1}/O^{2-} ratio with decreasing take-off angles.

The detailed analysis of the carbon compounds on the (100) surface is presented in Fig. 4. Beside the dominant aliphatic contribution, carbon–oxygen single bonds and carbon–oxygen double bonds were observed.

The C 1s detailed analysis for the TiO_2(100) surface is presented in for varying take off angles. About one third of carbon atoms are bound to either one (CO–R) or two (COO) oxygen atoms. Moreover, it can be concluded that low-weight carbon species such as carboxylic acids,

Table 2
Surface composition of (100) surface as measured by means of XPS at varying angles. All data are given with an experimental uncertainty of ±0.5%.

Angle (°)	O 1s (at.−%) at 530.2 eV	Ti 2p 3/2 (at.−%) at 458.8 eV	C 1s (at.−%) at 285 eV
70	63.2 ± 0.5	27.9 ± 0.5	8.9 ± 0.5
40	62.5 ± 0.5	24.7 ± 0.5	12.8 ± 0.5
20	61.3 ± 0.5	19.0 ± 0.5	19.7 ± 0.5
10	51.2 ± 0.5	13.8 ± 0.5	35.0 ± 0.5

Table 3
Detailed composition of the O 1s element spectra at varying take-off angles of the photoelectron. Presented values are ratios between component peak areas. The given uncertainties are resulting from the experiment and the fitting procedure of the model peak during data evaluation.

Angle (°)	O_Σ/Ti	O^{2-}/Ti	R_{O-1}/O^{2-}	R_{O-2}/O^{2-}
70	2.3 ± 0.09	1.9 ± 0.08	0.19 ± 0.008	0.04 ± 0.002
40	2.5 ± 0.10	1.9 ± 0.08	0.26 ± 0.010	0.07 ± 0.003
20	3.2 ± 0.13	2.1 ± 0.08	0.46 ± 0.018	0.12 ± 0.005
10	3.7 ± 0.15	2.2 ± 0.09	0.48 ± 0.019	0.26 ± 0.01

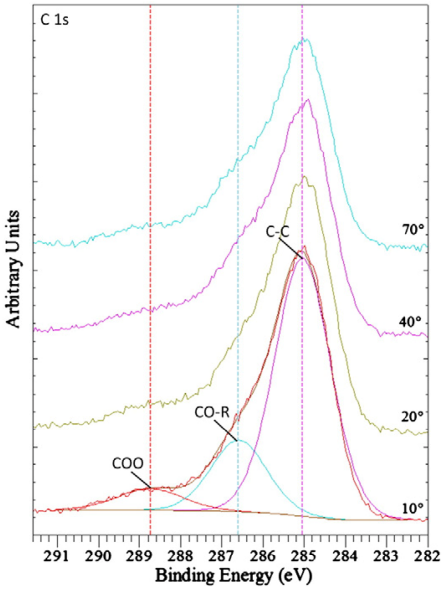

Fig. 4. C 1s element spectra at varying take-off angles. The take-off angles of the photoelectrons are given with respect to the surface plane. For better interpretability the spectra were normalized to the peak maximum as indicated by the vertical line at 285 eV.

ketones, ethers and metal carbonates, as shown in Table 4, contribute to the formation of atmospheric adsorbate films due to the contact with the laboratory atmosphere during cooling down after annealing and transfer of the crystal into the UHV system. As no significant angle dependency was observed, a disordered, non-oriented structure of the adsorbate layer can be suggested.

Table 4
Detailed XPS analysis of the carbon 1s peak of the native adsorbate layer as a function of the take-off angle. All data are given with an experimental uncertainty of ±0.5% resulting from the experiment and the following component-fit.

Angle (°)	COO (at.−%) (288 eV)	CO–R (at.−%) (286.5 eV)	C–C (at.−%) (285 eV)
70	7.8 ± 0.5	31.7 ± 0.5	60.5 ± 0.5
40	8.1 ± 0.5	32.9 ± 0.5	59.0 ± 0.5
20	8.3 ± 0.5	30.0 ± 0.5	61.7 ± 0.5
10	8.0 ± 0.5	30.1 ± 0.5	61.9 ± 0.5

3.2. Studies on NDCA film formation on TiO_2 single crystalline surfaces

3.2.1. AFM based nanoshaving studies

The sub-microscopic structure of the adsorbed NDCA film was studied by means of AC-mode AFM topographic imaging. Within the original scanning area a nanoshaving experiment was performed within a smaller frame of 500 × 500 nm^2 by means of contact mode scanning with a significantly higher force leading to a removal of the adsorbed NDCA molecules as shown in Fig. 5.

A submonolayer coverage of NDCA on the TiO_2(100) surface was observed as shown in Fig. 5. The shaved area showed the TiO_2 terraces of the bare TiO_2(100) surface proving that the adsorbate film could be removed during the nanoshaving experiments. The found corrugation of about 120 pm comparing the covered and shaved areas was lower in height than the theoretical height of a NDCA monolayer, indicating a disordered film of adsorbed NDCA molecules and a low surface concentration.

3.2.2. Surface composition and hydrophobicity

The static water contact angle of a freshly prepared TiO_2 surface was observed to be 18 ± 2° indicating a hydrophilic surface. On NDCA covered surfaces a contact angle of 45 ± 2° was measured where increase of the contact angle with respect to the as-prepared sample can be explained by a higher coverage of the crystal with hydrophobic aliphatic species. Since the contact angle mainly depends on the surface chemistry of the outermost layer the presence of adsorbed species can cause significant changes to the observed contact angle. Moreover, the orientation of adsorbed molecules plays an important role for the contact angle. From studies of thiol SAMs on gold substrates it is known that the degree of organization influences the observed contact angle with highly organized film (long adsorption time) resulting in higher contact angles and less organized films leading to lower contact angles [53]. In the case of a perfectly ordered CH_3 terminated SAM (e.g. octadecylthiole on Au [54]) typically a contact angle higher than 100° is found. Comparing this value with the observed contact angle for NDCA on TiO_2 which is similar to octadecylthiol in terms of the chemical end group indicates a disordered monolayer rather than an organized SAM.

Complementary XPS analysis proved the NDCA film formation with a significantly increased carbon concentration in comparison to the bare substrate (see Table 5 and for comparison Table 2). The

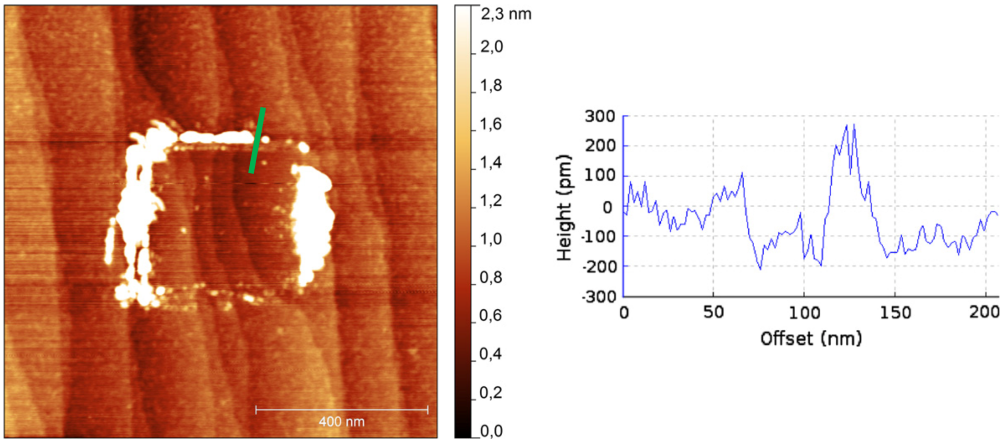

Fig. 5. Nanoshaving on an NDCA covered TiO_2(100) surface shows the disordered structure of the adsorbate layer (left). Cross section of the marked area (right).

Table 5
Surface composition of the NDCA covered TiO_2(100) crystal as measured by means of AR-XPS.

Angle (°)	O 1s (at.−%) at 530.2 eV	Ti 2p 3/2 (at.−%) at 458.8 eV	C 1s (at.−%) at 285 eV
70	54.1 ± 0.5	22.6 ± 0.5	23.2 ± 0.5
40	52.6 ± 0.5	18.2 ± 0.5	29.2 ± 0.5
20	41.7 ± 0.5	13.9 ± 0.5	44.4 ± 0.5
10	29.1 ± 0.5	8.9 ± 0.5	62.0 ± 0.5

Table 6
Detailed composition of the O 1s element spectra of the NDCA covered surface at varying take-off angles. Presented values are ratios between component peak areas. The given uncertainties are resulting from the experiment and the fitting procedure of the model peak during data evaluation.

Angle (°)	O_Σ/Ti	O^{2-}/Ti	R_{O-1}/O^{2-}	R_{O-2}/O^{2-}
70	2.4 ± 0.10	2.0 ± 0.08	0.16 ± 0.006	0.05 ± 0.002
40	2.8 ± 0.11	2.1 ± 0.08	0.24 ± 0.010	0.08 ± 0.003
20	3.0 ± 0.12	2.0 ± 0.08	0.32 ± 0.013	0.16 ± 0.006
10	3.3 ± 0.13	1.8 ± 0.07	0.60 ± 0.024	0.24 ± 0.010

angular dependency of the oxygen, titanium and carbon contributions shows the same trend as in Table 2.

The NDCA adsorbate layer shows the typical C 1s spectrum of a long chain carboxylic acid as seen in Fig. 6. Detailed XPS analysis of the NDCA covered TiO_2 crystals showed a C 1s peak with a peak width of 1.5 eV of the C–C component at 10°. The overall amount of carbon was increased by a factor of more than two in comparison to the bare substrate along with an increased O/Ti ratio (see Table 6 for detailed analysis) confirming a successful adsorption of NDCA on the crystal surface.

Thus the adsorption of NDCA led to a partial substitution of the atmospheric surface contamination most probably due to the additional van der Waals interactions of the long aliphatic chains. This result was supported by the analysis of the full width half maxima (FWHM) of the fitted C–C species comparing the as-prepared surface and the surface after adsorption of NDCA. For the as-prepared surface a FWHM of 1.9 eV was found in comparison to 1.5 eV for the NDCA covered surface. This result supports the partial substitution of the poorly defined contamination layer by a well-defined carbon species (NDCA). The different contributions of aliphatic carbon (285 eV), CO–R (286.5 eV) and COO (288.0 eV) did not show a trend as a function of the take-off angle. The ratio of the aliphatic carbon and the carboxylic carbon (C–C/COO) varied between 18.6 for 10° and 15.9 for 70° reflecting the molecular composition of the NDCA molecule.

To investigate the impact of the NDCA adsorption on the chemistry of the titanium dioxide surface the O 1s signals have been analyzed in comparison to the O 1s spectra of the as-prepared TiO_2(100) surface. The spectra presented in Fig. 7 do not show any significant change in regard to the XPS data before immersion (Fig. 3). Furthermore, the analysis of the contributions of the O 1s signal as presented in Table 6 and Fig. 7 reveals that the crystal surface underneath the NDCA surface layer still shows a similar OH:O^{2-} ratio as for the bare crystal along with a reduced overall amount of oxygen relative to the Ti 2p signal, which could be explained by the substitution of previously adsorbed water molecules.

As a result, no significant change in surface chemistry of the TiO_2(100) after adsorption the NDCA could be verified. The measured ratios of O_Σ/Ti, Ti–OH/O^{2-} and (H_2O, COOH)/O^{2-} follow the same trend as a function of take-off angle compared to Table 3. These results lead to the hypothesis that the adsorption of NDCA onto the TiO_2 surface prepared at ambient conditions is characterized by a weak interaction between the carboxylic acid group and the hydroxide covered surface. Moreover, this hypothesis is supported by the AFM nanoshaving experiments. Henderson has reported that an adsorbed water molecule dissociates at the TiO_2(100) leading to the formation of two hydroxide groups at the surface, one hydroxide group attached to the five-fold Ti^{4+} sites and the other at the bridging O^{2-} [16]. Moreover, volatile organic compounds could be strongly adsorbed onto the surface by means of a new Ti – O bond. The presence of both volatile compounds and hydroxide groups bound to the five-fold Ti^{4+} sites seems to

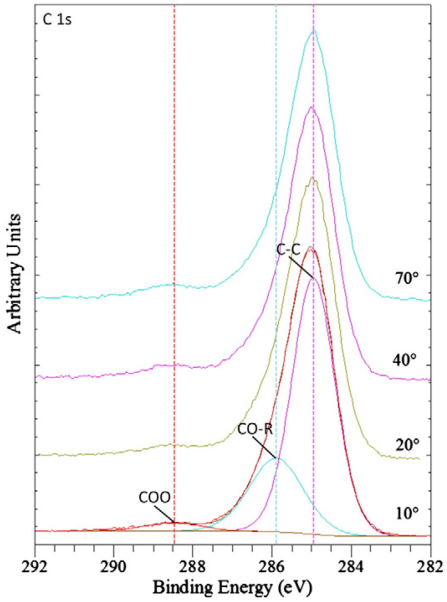

Fig. 6. C 1s spectrum of NDCA covered TiO_2 crystal at varying take-off angles. For better interpretability, the spectra were normalized to the peak maximum as indicated by the vertical line at 285 eV.

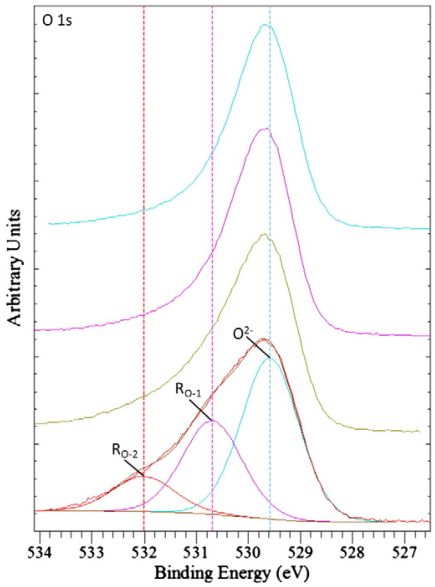

Fig. 7. O 1s spectra of the NDCA covered TiO_2(100) surface. The take-off angles of the photoelectrons are given with respect to the surface plane. For better interpretability, the spectra were normalized to the peak maximum as indicated by the vertical line.

inhibit the adsorption of the carboxylic acid onto the TiO_2 surface, thus only a weak interaction via hydrogen bonding can be formed between the carboxylic acid and the hydroxide group [14]. Thus, it can be concluded that the presence of the hydroxide groups, volatile compounds and the water adlayer at the surface prevents the formation of the NDCA self-assembly at ambient conditions.

4. Conclusions

The manuscripts describes an atmospheric high temperature preparation route of rutile $TiO_2(100)$ single crystalline surfaces leading to morphologically well-defined $TiO_2(100)$ surfaces with terminating surface hydroxide groups.

The $TiO_2(100)$ surface prepared at high temperature and ambient water and oxygen partial pressures showed a non-typical LEED pattern characterized by the presence of a 1×3 superstructure. The interpretation of the XPS data of the O 1s peak led us to the conclusion that hydroxide groups terminate the crystal surface. Moreover, the as prepared surface consists of organocarboxylic adsorbates which originate from the laboratory atmosphere. The adsorption of NDCA from ethanolic solution led to a significant substitution of the atmospheric contamination layer as proven by the XPS analysis. The surface concentration of carbon species increased by a factor of two and led to an increase of the static water contact angle from $18\pm3°$ for the as prepared surface to $45\pm3°$ for the NDCA covered surface. Moreover, the ratio between the carbon atoms of carboxylic acid groups and aliphatic carbon reflected the composition of the NDCA molecule. No self-assembled monolayer but a disordered adsorbate layer of NDCA molecules on the crystal surface was observed as deduced from the interpretation of the AR-XPS analysis and AFM based nanoshaving experiments. Nanoshaving proved to be a suitable method for the analysis of such sub-monolayer adsorbate layers. For the NDCA covered surface, nanoshaving revealed a disordered surface layer with submonolayer thickness of about 0.120 nm. We assume that the weak interfacial forces between the carboxylic acid group and the hydroxide terminated TiO_2 leads to the disorder and low coverage of the monolayer.

It has to be emphasized that the presented results are determined by the atmospheric preparation route of the TiO_2 surface. We conclude that results of this work suggest that there may be differences concerning the surface chemistry and the adsorption of admolecules between TiO_2 surfaces prepared in UHV and under atmospheric conditions. We think that the chosen strategy of following an atmospheric preparation route of the substrates and adsorbate layers significantly extends the applicability of single crystal based fundamental analysis to the understanding of the relationship between the surface chemistry and process characteristics of TiO_2 particle ensembles.

The prepared TiO_2 substrates are well suited as a model system for studies of adsorbate formation, particle wall interactions and interfacial reactions of related technical systems such as TiO_2 powders. The presented system also reflects common processes of relevant particle systems including a high-temperature synthesis, adsorbate formation as well as surface and interfacial reactions.

Acknowledgments

We gratefully acknowledge the Deutsche Forschungsgemeinschaft for financial support within the “Schwerpunktprogramm Partikel im Kontakt” DFG-SPP 1486.

References

[1] B. Kraeutler, A.J. Bard, J. Am. Chem. Soc. 100 (1978) 4317.
[2] A. Fujishima, X.T. Zhang, D.A. Tryk, Surf. Sci. Rep. 63 (2008) 515.
[3] Z.B. Zhang, C.C. Wang, R. Zakaria, J.Y. Ying, J. Phys. Chem. B 102 (1998) 10871.
[4] X. Nie, A. Leyland, A. Matthews, Surf. Coat.Technol. 125 (2000) 407.
[5] J.X. Liu, D.Z. Yang, F. Shi, Y.J. Cai, Thin Solid Films 429 (2003) 225.
[6] D.S. Koktysh, X.R. Liang, B.G. Yun, I. Pastoriza-Santos, R.L. Matts, M. Giersig, C. Serra-Rodriguez, L.M. Liz-Marzan, N.A. Kotov, Adv. Funct. Mater. 12 (2002) 255.
[7] W.Y. Choi, A. Termin, M.R. Hoffmann, J. Phys. Chem. 98 (1994) 13669.
[8] S.U.M. Khan, M. Al-Shahry, W.B. Ingler, Science 297 (2002) 2243.
[9] A.L. Linsebigler, G.Q. Lu, J.T. Yates, Chem. Rev. 95 (1995) 735.
[10] B. Oregan, M. Gratzel, Nature 353 (1991) 737.
[11] M. Gratzel, Nature 414 (2001) 338.
[12] U. Bach, D. Lupo, P. Comte, J.E. Moser, F. Weissortel, J. Salbeck, H. Spreitzer, M. Gratzel, Nature 395 (1998) 583.
[13] J.H. Braun, A. Baidins, R.E. Marganski, Prog. Org. Coat. 20 (1992) 105.
[14] U. Diebold, Surf. Sci. Rep. 48 (2003) 53.
[15] U. Diebold, J. Lehman, T. Mahmoud, M. Kuhn, G. Leonardelli, W. Hebenstreit, M. Schmid, P. Varga, Surf. Sci. 411 (1998) 137.
[16] M.A. Henderson, Langmuir 12 (1996) 5093.
[17] A. Linsebigler, G.Q. Lu, J.T. Yates, J. Chem. Phys. 103 (1995) 9438.
[18] M.A. Henderson, Surf. Sci. 319 (1994) 315.
[19] C.J. Zhang, P.J.D. Lindan, J. Chem. Phys. 118 (2003) 4620.
[20] A.D. Roddick-Lanzilotta, A.J. McQuillan, J. Colloid Interface Sci. 227 (2000) 48.
[21] R. Tero, T. Ujihara, T. Urisut, Langmuir 24 (2008) 11567.
[22] J.B. Sambur, C.M. Averill, C. Bradley, J. Schuttlefield, S.H. Lee, J.R. Reynods, K.S. Schanze, B.A. Parkinson, Langmuir 27 (2011) 11906.
[23] E.M.J. Johansson, S. Plogmaker, L.E. Walle, R. Scholin, A. Borg, A. Sandell, H. Rensmo, J. Phys. Chem. C 114 (2010) 15015.
[24] M.A. Henderson, J. Phys. Chem. 99 (1995) 15253.
[25] H. Onishi, T. Aruga, C. Egawa, Y. Iwasawa, Surf. Sci. 193 (1988) 33.
[26] M.A. Henderson, S. Otero-Tapia, M.E. Castro, Faraday Discuss. 114 (1999) 313.
[27] H. Idriss, K.S. Kim, M.A. Barteau, Surf. Sci. 262 (1992) 113.
[28] G.Q. Lu, A. Linsebigler, J.T. Yates, J. Phys. Chem. 98 (1994) 11733.
[29] S.A. Chambers, S. Thevuthasan, Y.J. Kim, G.S. Herman, Z. Wang, E. Tober, R. Ynzunza, J. Morais, C.H.F. Peden, K. Ferris, C.S. Fadley, Chem. Phys. Lett. 267 (1997) 51.
[30] A. Gutierrez-Sosa, P. Martinez-Escolano, H. Raza, R. Lindsay, P.L. Wincott, G. Thornton, Surf. Sci. 471 (2001) 163.
[31] M. Farshchi-Tabrizi, M. Kappl, Y.J. Cheng, J. Gutmann, H.J. Butt, Langmuir 22 (2006) 2171.
[32] R. Wang, N. Sakai, A. Fujishima, T. Watanabe, K. Hashimoto, J. Phys. Chem. B 103 (1999) 2188.
[33] J.P. Folkers, C.B. Gorman, P.E. Laibinis, S. Buchholz, G.M. Whitesides, R.G. Nuzzo, Langmuir 11 (1995) 813.
[34] R. Nakamura, N. Ohashi, A. Imanishi, T. Osawa, Y. Matsumoto, H. Koinuma, Y. Nakato, J. Phys. Chem. B 109 (2005) 1648.
[35] Y. Yamamoto, K. Nakajima, T. Ohsawa, Y. Matsumoto, H. Konuma, Jpn. J. Appl. Phys., Part 2 44 (2005) L511.
[36] A. Imanishi, T. Okamura, N. Ohashi, R. Nakamura, Y. Nakato, J. Am. Chem. Soc. 129 (2007) 11569.
[37] J.C. Love, L.A. Estroff, J.K. Kriebel, R.G. Nuzzo, G.M. Whitesides, Chem. Rev. 105 (2005) 1103.
[38] B. Torun, B. Oezkaya, G. Grundmeier, Langmuir 28 (2012) 6919.
[39] S.C. Abrahams, J.I. Bernstei, J. Chem. Phys. 55 (1971) 3206-&.
[40] CasaXPS, http://www.casaxps.com/.
[41] D.F. Mitchell, K.B. Clark, J.A. Bardwell, W.N. Lennard, G.R. Massoumi, I.V. Mitchell, Surf. Interface Anal. 21 (1994) 44.
[42] LEEDpat30, http://w3.rz-berlin.mpg.de/_hermann/LEEDpat/.
[43] Y.W. Chung, W.J. Lo, G.A. Somorjai, Surf. Sci. 64 (1977) 588.
[44] Q. Guo, I. Cocks, E.M. Williams, Surf. Sci. 366 (1996) 99.
[45] C.A. Muryn, P.J. Hardman, J.J. Crouch, G.N. Raiker, G. Thornton, D.S.L. Law, Surf. Sci. 251 (1991) 747.
[46] Y. Lu, B. Jaeckel, B.A. Parkinson, Langmuir 22 (2006) 4472.
[47] J. Schnadt, J.N. O'Shea, L. Patthey, J. Schiessling, J. Krempasky, M. Shi, N. Martensson, P.A. Bruhwiler, Surf. Sci. 544 (2003) 74.
[48] H. Idriss, P. Legare, G. Maire, Surf. Sci. 515 (2002) 413.
[49] L. Patthey, H. Rensmo, P. Persson, K. Westermark, L. Vayssieres, A. Stashans, A. Petersson, P.A. Bruhwiler, H. Siegbahn, S. Lunell, N. Martensson, J. Chem. Phys. 110 (1999) 5913.
[50] P.R. Moses, L.M. Wier, J.C. Lennox, H.O. Finklea, J.R. Lenhard, R.W. Murray, Anal. Chem. 50 (1978) 576.
[51] J. Wielant, T. Hauffman, O. Blajiev, R. Hausbrand, H. Terryn, J. Phys. Chem. C 111 (2007) 13177.
[52] T.K. Sham, M.S. Lazarus, Chem. Phys. Lett. 68 (1979) 426.
[53] C.D. Bain, E.B. Troughton, Y.T. Tao, J. Evall, G.M. Whitesides, R.G. Nuzzo, J. Am. Chem. Soc. 111 (1989) 321.
[54] P.E. Laibinis, G.M. Whitesides, D.L. Allara, Y.T. Tao, A.N. Parikh, R.G. Nuzzo, J. Am. Chem. Soc. 113 (1991) 7152.

3.6 Influence of the surface chemistry on TiO_2 - TiO_2 nanocontact forces as measured by an UHV-AFM

Christian Kunze, Ignacio Giner, Boray Torun, Guido Grundmeier
Chemical Physics Letters, 597, **2014**, 134-138.

The scientific work and discussion was coordinated and consolidated by CK under supervision of GG.
The manuscript was prepared by CK; IG contributed to the discussion of the UPS results.
TiO_2 single crystalline surfaces were prepared by CK and IG.
TiO_2 coated AFM tips were prepared by CK.
XPS and UPS experiments were performed by CK and IG, data evaluation was performed by CK.
UHV AFM experiments were performed by CK and IG, data evaluation was performed by CK.
The manuscript was revised by GG.

Within this work the interaction forces within a TiO_2 – TiO_2 nanocontact have been investigated by means of UHV AFM force-distance spectroscopy, which is a novel approach towards understanding contact forces on a fundamental level. Atmospherically prepared TiO_2 single crystalline surfaces as introduced in the paper presented in section 3.5, were employed as a substrate to measure interaction forces. Furthermore a defect free reference system was prepared by adsorbing an octadecylphosphonic acid (ODPA) monolayer on a TiO_2 single crystalline surface. It could be shown that the TiO_2 surface defect density plays an important role that determines the strength of interaction. The observed contact forces could be correlated to the surface defect density and were discussed based on the change in electronic structure induced by the surface defects and the impact on the Hamaker constant.

Chemical Physics Letters 597 (2014) 134–138

Contents lists available at ScienceDirect

Chemical Physics Letters

journal homepage: www.elsevier.com/locate/cplett

Influence of the surface chemistry on TiO_2 – TiO_2 nanocontact forces as measured by an UHV–AFM

Christian Kunze, Ignacio Giner, Boray Torun, Guido Grundmeier *

Technical and Macromolecular Chemistry, University of Paderborn, Warburger Str. 100, 33098 Paderborn, Germany

ARTICLE INFO

Article history:
Received 12 November 2013
In final form 18 February 2014
Available online 25 February 2014

ABSTRACT

Particle-wall contact forces between a TiO_2 film coated AFM tip and TiO_2(1 1 0) single crystal surfaces were analyzed by means of UHV–AFM. As a reference system an octadecylphosphonic acid monolayer covered TiO_2(1 1 0) surface was studied. The defect chemistry of the TiO_2 substrate was modified by Ar ion bombardment, water dosing at 3×10^{-6} Pa and an annealing step at 473 K which resulted in a varying density of Ti(III) states. The observed contact forces are correlated to the surface defect density and are discussed in terms of the change in the electronic structure and its influence on the Hamaker constant.

1. Introduction

Adhesion forces between micro- and nanoparticles play a major role in processes such as fluidization, agglomeration and sintering [1]. These processes are utilized in a wide range of technical fields, including the production of pharmaceutical powders, paints, and solar cells [2,3]. TiO_2 is a material of high scientific interest and has already been studied intensively [4,5]. Several phenomena correlated to the TiO_2 surface structure such as contact forces are not fully understood, yet. Contact forces between micro- and nanoparticles can be directly quantified by an atomic force microscope (AFM) [6]. Under ambient conditions particle–particle interactions are significantly influenced by side effects such as the formation of capillary forces [7,8] which are avoided under ultra high vacuum conditions (UHV) [5,9]. Up to now only few AFM contact force experiments under UHV conditions have been reported in the literature, e.g. by Tadepalli et al. who studied the bond formation at Cu–Cu interfaces [10].

Within this Letter we focus on TiO_2 – TiO_2 contact forces under ultrahigh vacuum conditions (UHV) on a fundamental level. TiO_2 single crystalline surfaces provide an excellent platform for studying adhesion phenomena due to their well-defined atomic surface structure [11] and surface chemistry. As shown by Takeuchi et al. the chemical composition of TiO_2 surfaces can be modified by the presence of water and the exposure to UV-light, which may result in a change of the adhesion phenomena [12].

When discussing force interactions on a nanoscopic level, not only specific interactions directly located in the contact area, but also the sub-surface composition and electronic properties have to be considered [13]. The presence of local dipoles and gradients in electron density of the interacting materials are crucial for the TiO_2 – TiO_2 system, as they contribute to the van der Waals interactions [14,15]. Interfacial forces of oxides can be influenced by the adsorption of self-assembled monolayers such as organophosphonic acids which form 2-dimensional crystalline aliphatic films [16].

In this Letter, the contact forces between a TiO_2 coated conical AFM tip and a rutile TiO_2(1 1 0) surface in different states were investigated under UHV-conditions to simulate a particle-wall contact. The study is based on the combination of an UHV AFM and X-ray photoelectron spectroscopy (XPS) in one UHV analytical system.

The analyzed interactions under different experimental conditions allow for the correlation of the adhesion forces and the chemical composition of the surfaces as well as the determination of the role of organic surface layers, defects and water.

2. Experimental

2.1. Preparation of TiO_2(1 1 0) single crystalline substrates

As planar substrates for the AFM adhesion experiments TiO_2(1 1 0) single crystalline surfaces were prepared under ambient lab conditions according to the procedure described in detail in reference [11]. Briefly, commercially available rutile TiO_2(1 1 0) single crystals (CrysTec, Germany) were etched in 20% HF (Merck KGa, Germany) for 10 min, followed by annealing in a horizontal tube furnace at 923 K for 48–72 h. The surface morphology after annealing was evaluated by means of an AFM (JKP Nanowizard II Ultra AFM, *JPK Instruments*, Germany) operated under ambient conditions. TiO_2(1 1 0) single crystalline surfaces after the annealing step

* Corresponding author.
E-mail address: g.grundmeier@tc.uni-paderborn.de (G. Grundmeier).

http://dx.doi.org/10.1016/j.cplett.2014.02.036
0009-2614/

showed atomically flat terraces of about 200–500 nm width with a step height of about 0.3 nm that corresponds to one TiO_2 unit cell in [1 1 0] direction (c = 0.296 nm) [17]. The crystals were directly introduced into the UHV analytical system after the annealing step, to minimize the contamination of the TiO_2(1 1 0) surface at the ambient atmosphere.

2.1.1. Adsorption of octadecyl phosphonic acid (ODPA) on TiO_2(1 1 0)

To replace poorly defined carbon contaminations due to atmospheric preparation, the TiO_2(1 1 0) substrate was chemically modified with ODPA (octadecyl phosphonic acid) to create 2-dimensional aliphatic crystalline surface layer. A freshly prepared and annealed TiO_2(1 1 0) crystal was placed in a 1 mM solution of ODPA (obtained from *Alfa Aesar*, 97% purity) in absolute ethanol (purity > 98%, obtained from VWR International) for 16 h. The formation of the adsorbate layer was monitored by static contact angle measurements (*Data Physics OCA 20*, Filderstadt, Germany), with a fixed drop volume of 5 μl. The contact angle was increased from 68° (bare surface) to 102° (after ODPA adsorption) which indicated the formation of a dense monolayer. A detailed XPS surface analysis of the ODPA covered TiO_2 substrate can be found in the supplementary material (Section 1) that showed a pronounced aliphatic C 1s peak leading to an overall carbon concentration of about 52 at.-% and about 2 at.-% P 2p. Due to the low surface energy of the ODPA covered substrate an additional contamination with atmospheric adsorbates can be neglected.

2.2. Preparation of TiO_2 coated AFM tips

TiO_2 modified AFM tips were prepared from AFM cantilevers type *NSC19* (*Mikromasch*, Bulgaria) by coating the AFM tip with a 150 nm thick titanium coating via a plasma-enhanced PVD process. The titanium target was sputtered by a DC plasma in pure Argon atmosphere at 0.2×10^{-3} Pa with a mean power of 2 kW and 300 V bias voltage. These parameters resulted in a deposition rate of 14 nm/min. To create a fully oxidized tip surface, the coated cantilevers were annealed for 16 h in air at 873 K. The geometry of the TiO_2 modified AFM tip was characterized by inverse AFM scanning with a spike grid type TGT1 (*NT-MDT*, Russia) under ambient conditions and SEM investigations which showed a tip radius of about 50 nm and a very smooth polycrystalline film covering the tip apex (see: Supplementary material Section 2).

2.3. Characterization of the crystalline phase of the TiO_2 coated AFM tips

As the AFM tip itself is too small to be analyzed, a planar model sample deposited on Si(100) of 10×10 mm^2 size – which was prepared and treated under the same conditions as the AFM tip in each step – was used as a representative sample for XPS, UPS and XRD investigations as described below.

The crystallographic structure of the TiO_2 AFM tip coating was investigated by means of grazing incidence XRD (GI-XRD). These results proved that this polycrystalline film revealed a rutile structure (see Figure 3 in the Supplementary material).

2.4. Combined surface analysis and UHV AFM based contact force measurements

The employed UHV-analytical set-up combining XPS and AFM is described in detail in a recent publication [11]. XPS was performed in an UHV chamber with a base pressure lower than 5×10^{-8} Pa. The surface composition was investigated by means of an *ESCA* + photoelectron spectroscopy system equipped with a 128 channel electron detector (*Oxford Instruments*, Taunusstein, Germany). The take-off angle of the photoelectrons was 60° with respect to the surface normal which leads to an information depth of about 2.4 nm in XPS [18] for the used monochromated Al-Kα X-ray source with a photoelectron energy of 1486.7 eV. The electron analyzer was operated at a pass energy of 25 eV. Ultraviolet photoelectron spectroscopy (UPS) was performed in the same chamber with a HeI source (excitation energy of 21.2 eV). In UPS mode the electron analyzer was operated at a pass energy of 1 eV.

UHV AFM topography imaging and force distance spectroscopy was performed by means of a *VT-AFM XA* (Oxford Instruments, Taunusstein, Germany). For topograpic imaging in contact mode cantilevers of type *CSC17*, (Mikromasch, Bulgaria), were used.

AFM force distance spectroscopy experiments were performed for each surface state by collecting AFM force distance curves from an overlying 16×16 point grid on a 2×2 μm^2 probing area at room temperature allowing a data interpretation based on a statistical basis. The approach and retract speed of the AFM tip was set to 1 μm/s, the overall distance of each force curve was 250 nm. The measured forces were calibrated based on the sensitivity of the AFM setup derived from the force curve and the nominal spring constant of the AFM cantilever.

2.5. Modification of TiO_2(1 1 0) surfaces via Ar^+ bombardment

Ar^+ bombardment of both TiO_2 surfaces – the TiO_2(1 1 0) and the TiO_2 coated AFM tip – was performed with an ion-energy of 200 eV, which resulted in the complete removal of carbon contaminations after 12 min for the TiO_2(1 1 0) single crystalline substrate and 15 min for the TiO_2 modified AFM tip.

3. Results and discussion

3.1. Role of surface defects

Before and after Ar^+ bombardment, the crystallinity of the TiO_2(1 1 0) surface was checked by means of low energy electron diffraction (LEED), detailed information describing the setup can be found in [11]. After Ar^+ bombardment, the LEED image still indicated a clear rectangular pattern similar as for the untreated sample which is presented in the supplementary material (Figure 5).

Additionally, the surface topography after the Ar^+ bombardment step was measured by UHV AFM in contact mode that showed very smooth terraces without evidence for surface damage during the procedure which is presented in the supplementary material (Figure 6).

3.1.1. XPS investigations

Figure 1a) shows the Ti 2p elemental spectra of the TiO_2(1 1 0) substrate before and after Ar^+ bombardment cleaning. No significant differences between the XPS spectra of the TiO_2(1 1 0) substrate and the TiO_2 coated film were observed. Additional XPS spectra (Ti 2p and O 1s XPS data of the TiO_2 coating) are presented in the supplementary material (Sections 6 and 7).

After Ar^+ bombardment, the TiO_2 samples presented a high defect density in the surface near region. In both cases around 20% of the titanium was in the +III oxidation state which can be explained by the transfer of an electron to the empty Ti 3d orbital during the creation of the surface defects as discussed by Wendt et al. [19]. As also mentioned there, the defects created by Ar^+ bombardment are complex, with a different variety of local environments where O and Ti surface atoms coexist. The exact defect distribution is still subject of controversy, but it is widely accepted that via Ar^+ bombardment both – surface defects and sub-surface defects – are created [20]. The found defect density is comparable to values up to 25% after Ar^+ bombardement discussed in the literature [21].

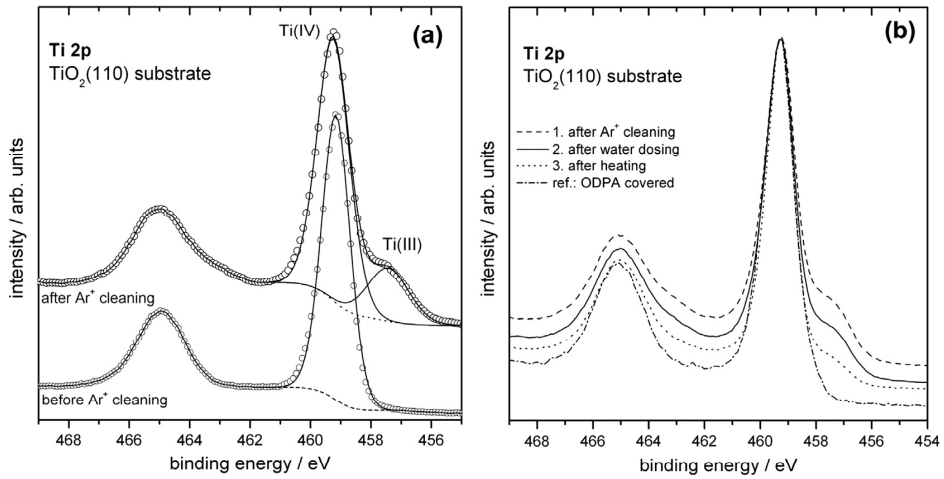

Figure 1. (a) Ti 2p core level spectra of the $TiO_2(1\,1\,0)$ substrate before and after Ar^+ cleaning (b) Ti 2p core level spectra of the Ar^+ cleaned surface after water dosing at 3×10^{-6} Pa for 30 min followed by annealing the sample to 473 K for 30 min. For comparison the Ti 2p core level of a ODPA adsorbed monolayer onto TiO_2 bare crystal which reflects a defect-free surface is shown.

As our work aims at the investigation of the adhesion phenomena, the Ar^+ cleaned defective surface was selected as the initial point for the surface chemistry variation. Via a leak valve system water was dosed at 3×10^{-6} Pa for 30 min followed by a subsequent annealing at 473 K for 30 min. After each step XPS and UPS measurements were performed. As the sample had to be transferred from the AFM to the XPS chamber within the UHV system it was only possible to observe permanent changes in the chemistry of the surface near TiO_2 region. The Ti 2p core level spectra as presented in Figure 1b) show a decrease in Ti(III) defect density at 457.2 eV binding energy after water dosing and subsequent annealing. For comparison the defect-free ODPA covered $TiO_2(1\,1\,0)$ surface is shown as a reference. From these results a saturation of surface defects by a reaction with H_2O and annealing was followed. As pointed out by Wang et al, top-surface defects will be reduced more easily than the sub-surface defects [20]. Hence, the presence of Ti (III) states after the heating may be mainly ascribed to sub-surface defects.

The corresponding O 1s spectra are presented in the supplementary material (Figure 7) and did not show any significant differences after water dosing and annealing of the $TiO_2(1\,1\,0)$ substrate. Walle et al. studied the interaction of water with defective $TiO_2(1\,1\,0)$ surfaces and reported that the formation of defects has almost no influence on the observed O 1s spectra and that the surface OH—H_2O balance is an inherent property of the $TiO_2(1\,1\,0)$ surface itself [22]. Within this Letter no strongly adsorbed water layer was observed during exposure to 3×10^{-6} Pa water partial pressure, which is also in accordance with the results of Walle et al. [22]. Ketteler et al. studied the adsorption of water on $TiO_2(1\,1\,0)$ surfaces at elevated pressures up to 200 Pa [23]. They found that bridge O-vacancies are reactive surface sites for the dissociation of water followed by the formation of surface OH. Within the O1s spectra they also did not observe an increase in surface OH at higher partial pressures of water.

For the thin TiO_2 coating only very small differences in the Ti(III)/Ti(IV) ratio could be observed after exposure to the same conditions of water dosing which might hint to a different mechanism of defect saturation. However, as this finding indicates that the chemistry of the TiO_2 AFM tip coating is marginally affected by the procedure of Ar^+ cleaning – water dosing – heating in comparison to the $TiO_2(1\,1\,0)$ substrate, it allows to assign the observed change in contact forces mainly to changes in the chemistry of the $TiO_2(1\,1\,0)$ surface. The changes in surface chemistry of the $TiO_2(1\,1\,0)$ substrate are reflected in the Ti(III)/Ti(IV) ratios observed in the Ti 2p core level spectra. After Ar^+ cleaning 20% of Ti(III) contributions were detected, which decreased to 17% Ti(III) after water dosing and to 10% Ti(III) after heating, respectively. A detailed quantification of the $TiO_2(1\,1\,0)$ single crystal regarding O 1s and Ti 2p contributions can be found in the supplementary material (Table 1).

3.1.2. UPS investigations

Variations in the valence orbitals during the procedure were analyzed by means of UPS. Figure 2 shows UPS spectra of the $TiO_2(1\,1\,0)$ substrate after the Ar^+ cleaning process followed by water dosing and subsequent heating. As a comparison the UPS spectrum of the ODPA covered $TiO_2(1\,1\,0)$ substrate is shown, that reflects a defect-free surface. Although the information depth of

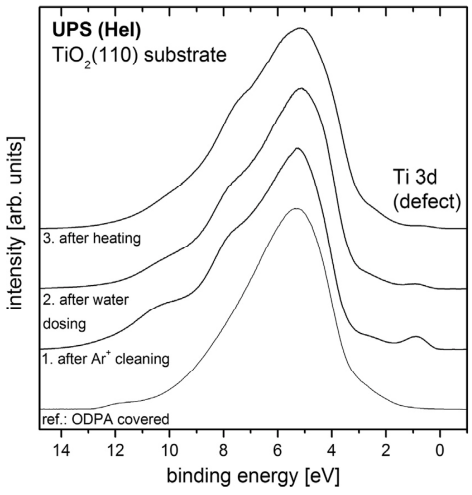

Figure 2. UPS spectra of $TiO_2(1\,1\,0)$ surfaces after different step procedure.

UPS is significantly smaller than for XPS, the substrate electronic structure can still be observed [24,25] as indicated by the O 2p observed main peak including oxygen from the phosphonic acid anchor group and the oxide substrate [26].

The O 2p valence band presents a main feature located at 5.5 eV with shoulders at 7 eV and 11 eV as also observed by Krischok et al. [27]. The most relevant peak at 0.9 eV is assigned to Ti 3d transitions. The area of this peak is directly related to the presence of defects in the surface near region [28]. The UPS spectra clearly show that the ODPA monolayer covered TiO_2 surface is free of Ti 3d defects. After water dosing the intensity of the Ti 3d transition is significantly reduced, indicating that the water exposure decreases the surface defect density. After heating up to 473 K, the intensity of the Ti 3d transition is further reduced which indicates an additional healing process. The observed UPS data are in excellent agreement with the XPS data.

3.2. UHV AFM force–distance spectroscopy

As the exact contact geometry of the AFM experiment cannot be perfectly described, the same TiO_2 coated AFM tip was used for the whole set of experiments to assure comparability. As the maximum forces during the tip-substrate contact were kept quite small (<20 nN) and the contact area of the 50 nm radius TiO_2 coated AFM tip is way larger than for a standard AFM tip we do not expect any influence of tip degradation such as flattening of the tip that would lead to an increased contact area. Furthermore, the influence of the TiO_2 substrate roughness can be neglected, since the width of the terraces (about 200–500 nm) is large in comparison to the tip radius (50 nm), and the step height (0.3 nm) is smaller than the roughness of the TiO_2 coated tip.

The histograms of the AFM contact forces as obtained from the force distance curves are presented in Figure 3. The observed force curves (see: Supplementary material, Figure 9) did not show any long range interactions. For the Ar^+ cleaned surface a broad distribution and the highest adhesion forces were observed which could be attributed to the defective $TiO_2(1\,1\,0)$ surface state. The strong interaction found between the TiO_2 surfaces can be explained by the occupied Ti $3d^1$ orbital configurations that offer electrons for the formation of additional bonds. Yong et al. studied the contact of TiO_2 surfaces via molecular dynamics simulations and conclude

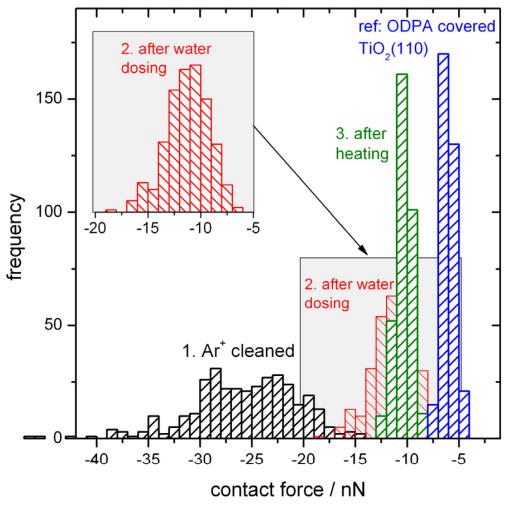

Figure 3. Histograms of contact forces for different surface chemistries of the TiO_2 – TiO_2 nanocontact.

that the deformation of TiO_2 in the contact area creates defects that lead to additional bonds along with higher adhesion forces [29]. As within our work TiO_2 defects are created via the cleaning process we expect a comparable mechanism of interaction. As a second effect the Hamaker constant is increased due to the strong gradient in electron density in the surface near region caused by the TiO_2 defects. Recent DFT studies revealed that excess electrons from the oxygen vacancies delocalized along the surface creating an electron gradient from the surface to the bulk [14]. Studies of the local electron density in grain boundaries by means of high resolution transmission electron spectroscopy and valence electron energy-loss spectroscopy showed an increased contribution of London dispersion forces in Fe doped $SrTiO_3$ [30] and silicon nitride films [31].

The broad distribution of the histogram hints to a chemically inhomogeneous defective surface offering multiple defects within the contact area for interaction. After water dosing a significantly narrower distribution and a significant lower adhesion force was observed. We propose that this finding can be attributed to the decreasing defect density in the surface near region, while the contact geometry is not affected. After heating of the $TiO_2(1\,1\,0)$ substrate, the defect density is further decreased leading to a narrower force distribution pointing towards a more homogeneous surface composition.

For the ODPA covered $TiO_2(1\,1\,0)$ surface the smallest interaction and the narrowest distribution force has been observed. This effect is mainly dominated by the changed surface chemistry of the substrate from TiO_2 to an aliphatic carbon chemistry.

3.3. Estimation of interaction forces based on Hamaker constants

The non-retarded Hamaker constant A_{11} for the interaction TiO_2/vacuum/TiO_2 can be found according to the literature to be about 150×10^{-21} J [32]. The Hamaker constant A_{22} for the interaction of hydrocarbon chains C_nH_{2n}/vacuum/C_nH_{2n} can be estimated to about 28×10^{-21} J [33]. The relation:

$$A_{12} \approx \sqrt{A_{11} \cdot A_{22}} \tag{1}$$

gives a combined Hamaker constant A_{12} TiO_2/vacuum/C_nH_{2n} of 65×10^{-21} J which lowers the interaction force by a factor of 2.3 comparing the TiO_2 tip in contact with the $TiO_2(1\,1\,0)$ substrate. This finding is in very good agreement with the observed adhesion forces of the AFM studies when regarding the $TiO_2(1\,1\,0)$ substrate after the healing of defects. It can be followed that the increase in interaction force for the Ti(III) rich surfaces can be explained by the increased donor density and electron density in the conduction band of TiO_2 [34,35]. Thus this finding has to be addressed to both – surface and sub-surface defects – as they contribute to the interaction volume relevant for the van der Waals interactions [14].

4. Conclusions

In this contribution a new experimental approach which correlates particle-wall contact forces between TiO_2 – TiO_2 nanocontacts under UHV conditions regarding the surface defect density is proposed. The higher TiO_2 – TiO_2 contact forces for the Ti(III) rich surface in comparison to the bare but in Ti(III) depleted surface were measured. This might be ascribed to the increase in London dispersion forces due to the defect induced change in the surface electronic structure. The increase in the dispersion forces is explained by the increased density of electrons in the conducting band of Ti(III) rich TiO_2 surfaces. The broad distribution in the observed adhesion forces for the defective surface is attributed to randomly distributed multiple defects within the contact area. A lowered defect density could be correlated with a decreased

overall interaction force along with a narrower distribution of observed force values. The comparison of an almost defect free TiO_2(1 1 0) substrates showed that the difference in interaction can be discussed based on the non-retarded Hamaker constants.

Acknowledgements

The authors gratefully acknowledge the financial support of the German Research Foundation (DFG) within the 'Schwerpunktprogramm Partikel im Kontakt' DFG-SPP 1486.

We thank Dr. Harish Parala from the workgroup of Prof. Dr. Anjana Devi, Chair II of Inorganic Chemistry, Ruhr University Bochum for GI-XRD measurements.

Furthermore we would like to thank Fabian Assion, M.Sc. from the workgroup of Prof. Dr.-Ing. U. Hilleringmann, Faculty of Computer Science, Electrical Engineering and Mathematics at the University of Paderborn for the deposition of the PVD titanium coatings.

Appendix A. Supplementary data

Supplementary data associated with this article can be found, in the online version, at http://dx.doi.org/10.1016/j.cplett.2014.02.036.

References

[1] S. Salameh et al., Langmuir 28 (2012) 11457.
[2] H. Weller, Adv. Mater. 5 (1993) 88.
[3] N.G. Park, J. van de Lagemaat, A.J. Frank, J. Phys. Chem. B 104 (2000) 8989.
[4] U. Diebold, Surf. Sci. Rep. 48 (2003) 53.
[5] X. Chen, S.S. Mao, Chem. Rev. 107 (2007) 2891.
[6] M. Farshchi-Tabrizi, M. Kappl, Y.J. Cheng, J. Gutmann, H.J. Butt, Langmuir 22 (2006) 2171.
[7] P.A. Kralchevsky, K. Nagayama, Langmuir 10 (1994) 23.
[8] X.D. Xiao, L.M. Qian, Langmuir 16 (2000) 8153.
[9] J.Y. Park, D.F. Ogletree, M. Salmeron, C.J. Jenks, P.A. Thiel, Tribol. Lett. 17 (2004) 629.
[10] R. Tadepalli, C.V. Thompson, Appl. Phys. Lett. 90 (2007) 151919.
[11] C. Kunze, B. Torun, I. Giner, G. Grundmeier, Surf. Sci. 606 (2012) 1527.
[12] M. Takeuchi, G. Martra, S. Coluccia, M. Anpo, J. Phys. Chem. C 111 (2007) 9811.
[13] J.N. Israelachvili, Intermolecular and Surface Forces, Elsevier Science, 2010.
[14] S. Chretien, H. Metiu, J. Phys. Chem. C 115 (2011) 4696.
[15] J. Mahanty, B.W. Ninham, Dispersion Forces, Academic Press, 1976.
[16] P. Thissen, M. Valtiner, G. Grundmeier, Langmuir 26 (2010) 156.
[17] C.J. Howard, T.M. Sabine, F. Dickson, Acta Crystallogr. B 47 (1991) 462.
[18] J.F. Watts, J. Wolstenholme, An Introduction to Surface Analysis by XPS and AES, Wiley, 2003.
[19] S. Wendt et al., Science 320 (2008) 1755.
[20] L.Q. Wang, D.R. Baer, M.H. Engelhard, A.N. Shultz, Surf. Sci. 344 (1995) 237.
[21] L.Q. Wang, D.R. Baer, M.H. Engelhard, Surf. Sci. 320 (1994) 295.
[22] L.E. Walle, A. Borg, P. Uvdal, A. Sandell, Phys. Rev. B 86 (2012) 205415.
[23] G. Ketteler et al., J. Phys. Chem. C 111 (2007) 8278.
[24] D.M. Alloway et al., J. Phys. Chem. B 107 (2003) 11690.
[25] Y.-P. Lin et al., J. Phys. Chem. C 117 (2013) 9895.
[26] S.A. Paniagua et al., J. Phys. Chem. C 112 (2008) 7809.
[27] S. Krischok, J. Gunster, D.W. Goodman, O. Hofft, V. Kempter, Surf. Interface Anal. 37 (2005) 77.
[28] C.M. Yim, C.L. Pang, G. Thornton, Phys. Rev. Lett. 104 (2010) 036806.
[29] C.W. Yong, W. Smith, K. Kendall, J. Mater. Chem. 12 (2002) 2807.
[30] K. van Benthem, G. Tan, L.K. DeNoyer, R.H. French, M. Rühle, Phys. Rev. Lett. 93 (2004) 227201.
[31] R.H. French, H. Mullejans, D.J. Jones, G. Duscher, R.M. Cannon, M. Ruhle, Acta Mater. 46 (1998) 2271.
[32] L. Bergström, Adv. Colloid Interface Sci. 70 (1997) 125.
[33] C.J. Drummond, G. Georgaklis, D.Y.C. Chan, Langmuir 12 (1996) 2617.
[34] S. Sounilhac, E. Barthel, F. Creuzet, Appl. Surf. Sci. 140 (1999) 411.
[35] S. Sounilhac, E. Barthel, F. Creuzet, J. Appl. Phys. 85 (1999) 222.

Influence of the surface chemistry on TiO_2 - TiO_2 nanocontact forces as measured by an UHV-AFM

*Christian Kunze, Ignacio Giner, Boray Torun and Guido Grundmeier**

Technical and Macromolecular Chemistry, University of Paderborn, Warburger Str. 100, 33098 Paderborn, Germany.

*corresponding author: g.grundmeier@tc.uni-paderborn.de

Supplementary Material

1. XPS C 1s and P 2p spectra of the ODPA covered TiO_2(110) substrate

On the ODPA covered TiO_2(110) surface showed a pronounced C 1s signal with a predominantly aliphatic contribution at 284.5 eV was found leading to an overall carbon concentration of 52%. Additionally the presence of phosphorous (~ 1 – 2 at.-%) could be proven, indicating a successful adsorption of ODPA on the TiO_2(110) surface.

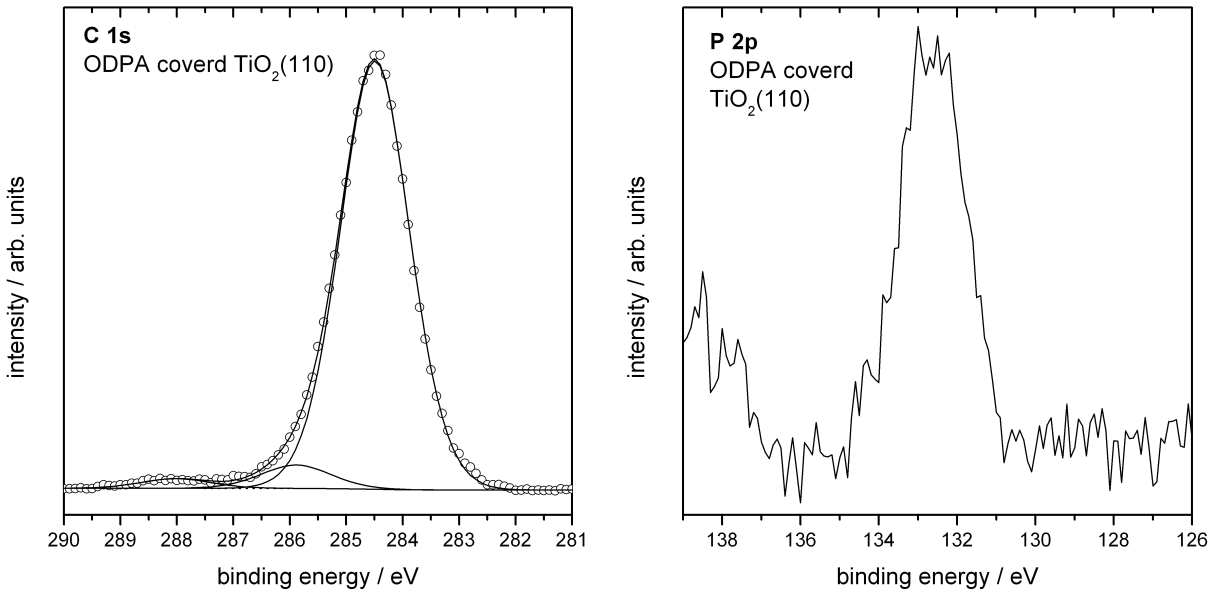

Figure 1: XPS C 1s and P 2p core level spectra of the ODPA coverd TiO_2(110) surface

2. Tip shape analysis of the TiO_2 coated AFM tip

The tip shape of the TiO_2 modified AFM tip was characterized by inverse AFM scanning with a spike grid type TGT1 (*NT-MDT*, Russia) under ambient conditions by means of a JPK Nanowizard II Ultra AFM (*JPK Instruments*, Germany). Based on the image presented in Figure 2 the radius of the TiO_2 coated tip is about 50 nm.

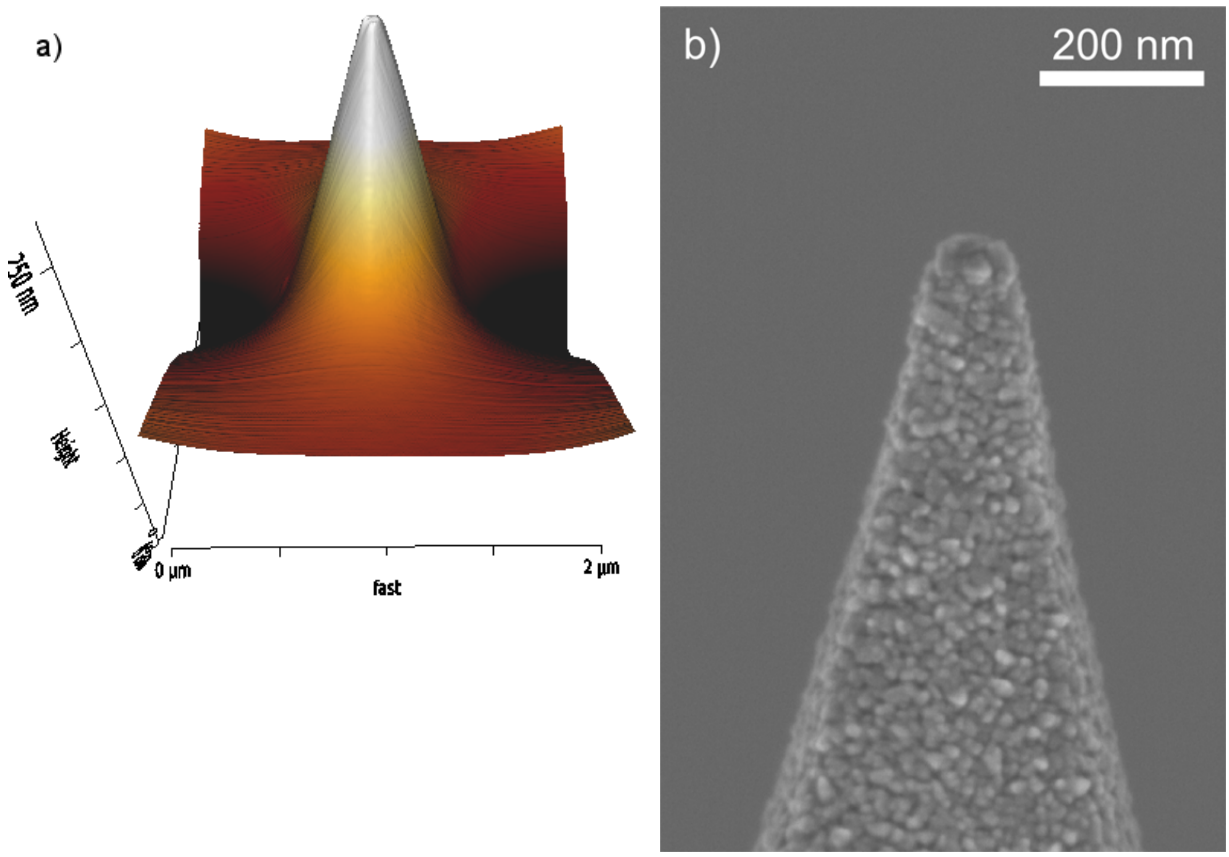

Figure 2 a.b: a) AFM image of the TiO_2 coated tip geometry obtained by inverse AFM scanning and b) by SEM imaging

3. Crystallinity of the TiO_2 AFM tip coating

X-ray diffraction (GI-XRD) patterns were recorded in grazing incidence (with typical incidence angle $\omega = 1°$) and parallel beam geometry with a Panalytical X'Pert Pro MRD diffractometer equipped with a pixel detector and a parabolic mirror in front of a Cu Kα X-ray source (1.5418 Å). The diffractogram presented in Figure 3 indicates the rutile TiO_2 phase (JCPDS-079-5859).

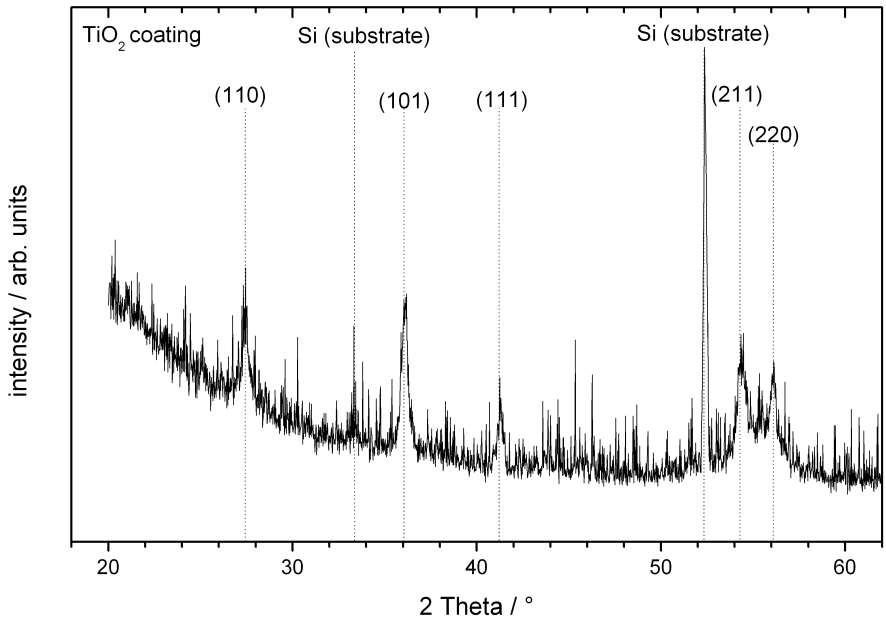

Figure 3: GI-XRD diffractogram of the TiO_2 coating.

4. LEED analysis of the Ar^+ cleaned TiO_2(110) surface

The LEED analysis was performed at a primary energy of the incident electrons of 100 eV. For the Ar^+ cleaned substrate a clear LEED diffraction pattern as presented in Figure 4 was observed, which is in accordance with LEED patterns reported for TiO_2(110) surfaces in the literature (1,2). Thus we follow no significant sputtering effect during Ar^+ cleaning that leads to a significant surface roughening and destruction of the surface crystallinity.

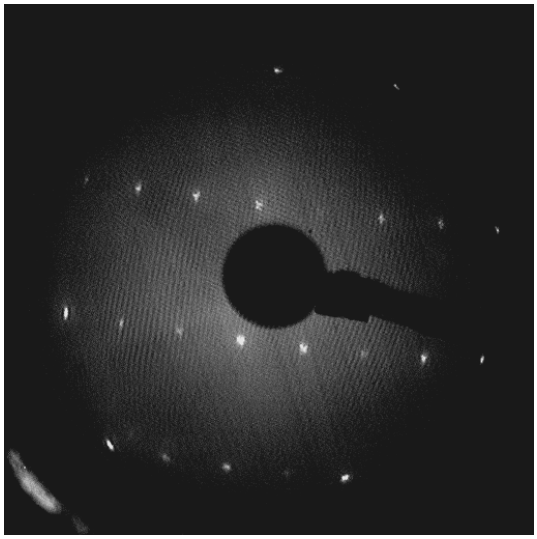

Figure 4: LEED pattern of the TiO_2(110) surface after Ar^+ cleaning at an electron energy of 100 eV.

5. UHV-AFM analysis of the Ar^+ cleaned TiO_2(110) surface

The AFM analysis (scan size 2 x 2 µm²) shows a well-defined and smooth surface without evidence for a surface destruction after Ar^+ cleaning.

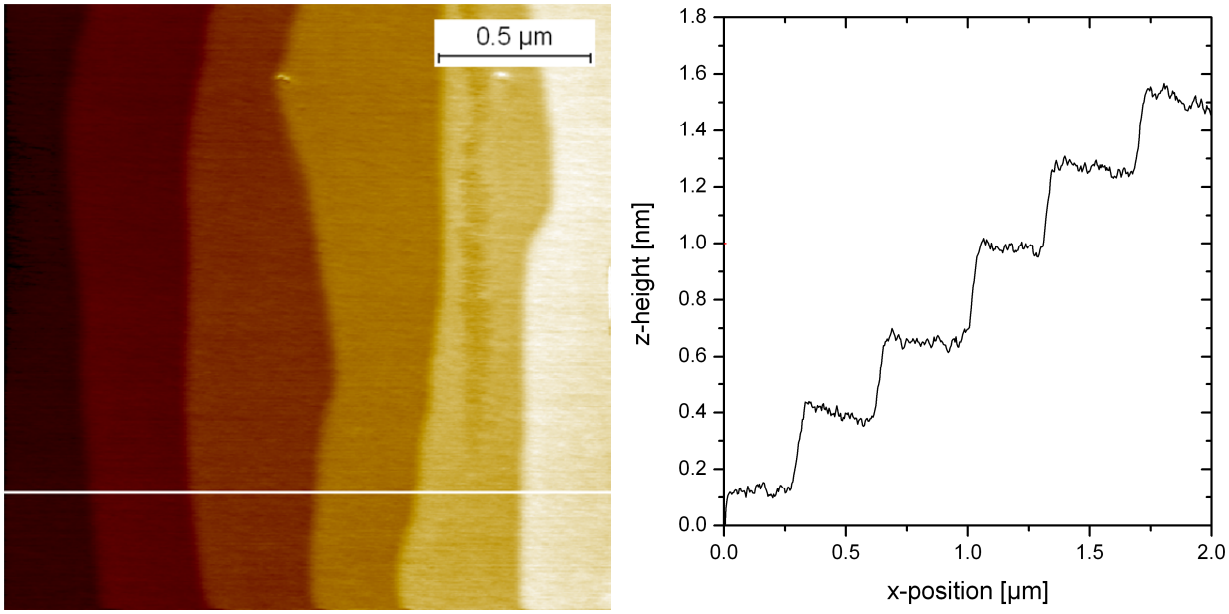

Figure 5 a, b: a) Contact mode UHV-AFM image of the Ar^+ cleaned TiO_2(110) substrate. The scan size is 2 x 2 µm. b) Cross section of the marked line.

6. XPS analysis of the TiO_2 AFM tip coating

The changes in surface chemistry of the TiO_2 AFM tip coating are not significantly differing from the single crystalline TiO_2(110) substrate. During the process of Ar^+ cleaning also Ti^{3+} defects are created which lead to a defect density comparable to the TiO_2(110) substrate.

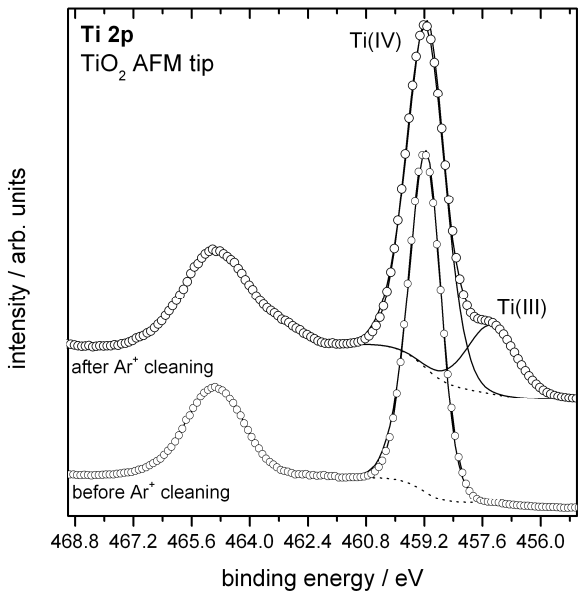

Figure 6: Ti 2p core level spectra of the TiO_2 AFM tip coating before and after Ar^+ cleaning

7. XPS O 1s spectra of the TiO_2(110) substrate TiO_2 AFM tip coating

The O 1 s spectra as presented in Figure 7 did not show significant differences between the TiO_2(110) substrate and the TiO_2 AFM tip coating in surface chemistry after Ar^+ cleaning. Apart from O^{2-} at 530.7 eV two additional oxygen species at 531.5 eV and 532.3 eV were identified, that Perron et al. assign to bride and top oxygen positions (3).

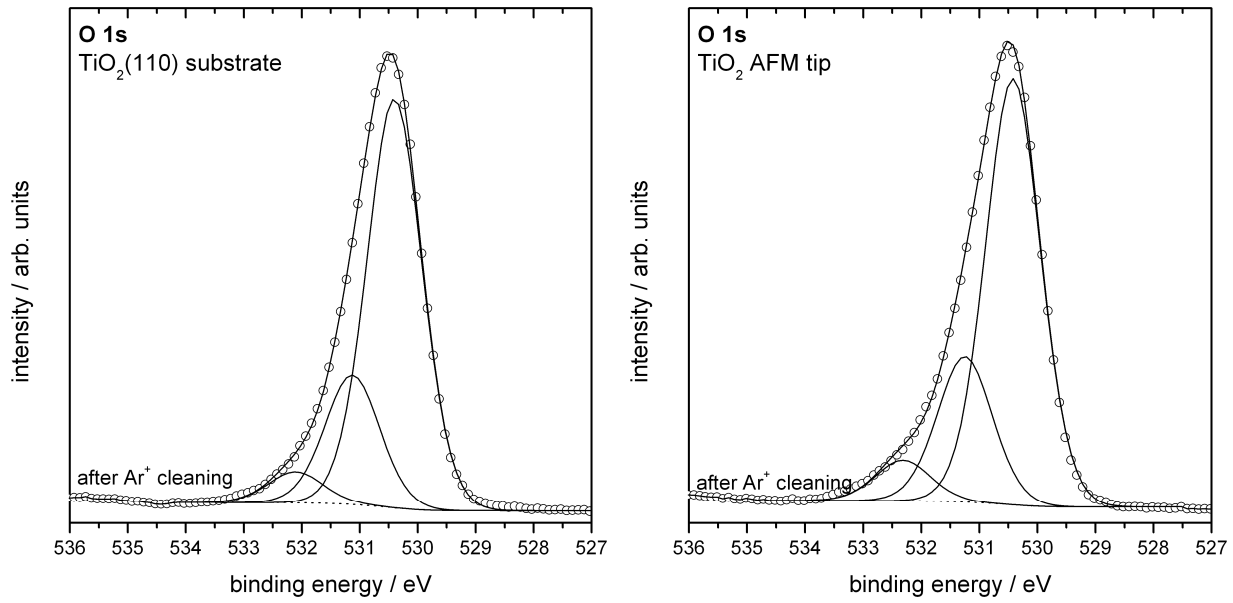

Figure 7 a, b): O 1 s core level spectra of the TiO_2(110) substrate (left) and the TiO_2 AFM tip coating before and after Ar^+ cleaning.

8. Quantification of Ti 2p and O 1s contributions and evolution of the XPS O 1s spectra of the TiO_2(110) substrate after water dosing and heating

At this point we do not discuss the ODPA covered TiO_2(110) substrate, as the oxygen contributions present in the ODPA phosphonic groups cannot be reliably distinguished from TiO_2 oxygen. In the following table the detailed O 1s and Ti 2p contributions are presented.

Table 1: Ti 2p and O 1s contributions for the TiO_2(110) substrate in at.%, all values include an error of ±2% based on the XPS data.

	Ti 2p		O 1s		
	Ti(IV)	Ti(III)	O_{top}	O_{bridge}	O^{2-}
1. after Ar^+ cleaning	23	6	4	16	51
2. after water dosing	24	5	3	14	54
3. after heating	26	3	4	12	55

Within the O 1s core level spectra no significant changes could be observed after the steps of water dosing and heating as presented in Figure 8.

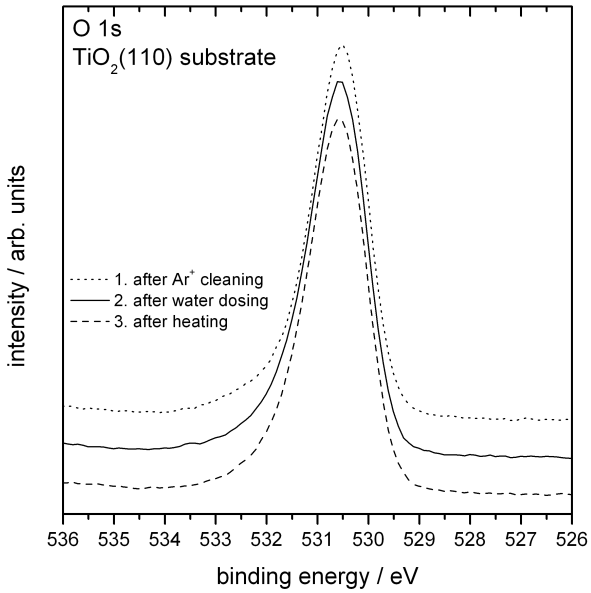

Figure 8: Evolution of the TiO_2 O 1s peak after Ar^+ cleaning, water dosing and heating.

9. Exemplary AFM force curve obtained in the contact force experiments

The AFM force-displacement curve does not show any long range forces and is close to ideal.

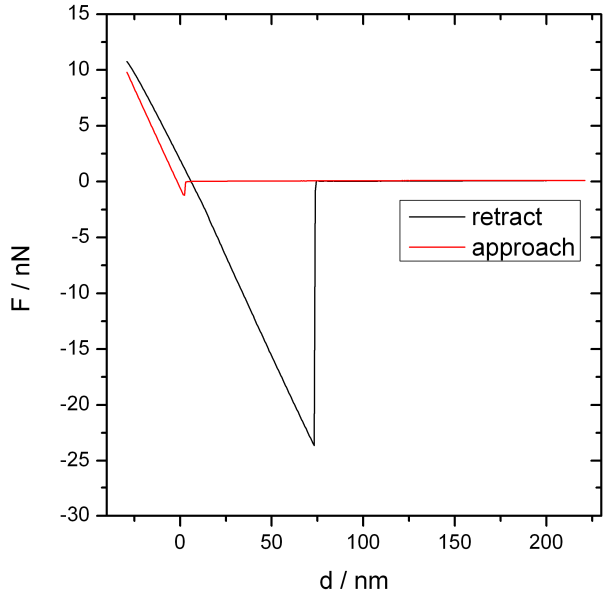

Figure 9: Exemplary AFM force curve obtained for the Ar^+ cleaned TiO_2(110) surface.

References

(1) J M Pan, B L Maschhoff, U Diebold, T E Madey, Surface Science 291 (1993) 381-94.
(2) R A Bennett, S Poulston, P Stone, M Bowker, Physical Review B 59 (1999) 10341-46.
(3) H Perron, J Vandenborre, C Domain, R Drot, J Roques, E Simoni, J J Ehrhardt, H Catalette, Surface Science 601 (2007) 518-27.

Chapter 4

4 Conclusions and Outlook

Discussing interactions at interfaces such as adhesion or chemical reactions, the chemical composition and morphology not only of the topmost surface, but also of the surface near region of the studied material is of crucial importance. Within this work interfacial reactions and interactions of two important materials were studied: *M*AlN(O) with *M* = Ti, Cr and TiO_2. Although these materials may appear to have a quite different nature, the interfacial interactions observed within this work are significantly driven by material defect structures and non-equilibrium surface states.

TiAlN(O) and CrAlN have a promising potential as hard coatings for tool steels within polymer processing such as extrusion and injection molding. For all investigated coating systems an enrichment of oxygen in the surface near region was observed which has to be considered carefully when discussing the interaction to the polymer, as this surface near region – and not the bulk composition of the material – determines the interfacial interaction. The oxidation process occurs most likely after the deposition of the coatings upon contact with the ambient atmosphere upon venting the deposition chamber, which does not allow for well controlled conditions.

This work contributed to the better understanding of the oxide formation on TiAlN(O) and CrAlN materials. For all investigated TiAlN(O) coatings a non-stoichiometric composition with an excess of anions was found, which is even increased for the surface near region due to the incorporation of oxygen into the lattice structure. A different trend has been observed for the investigated CrAlN coatings: Here the volume structure shows a depletion of anions but also an excess of anions in the surface near region. This opposite trend was even stronger for coatings deposited at long HPPMS pulse durations, as this parameter influences the grade of ionization within the plasma. In this case, a lower incorporation of anions into the volume structure of the coating was found. The investigated CrAlN coatings showed an almost stoichiometric composition of the surface near region with a marginal excess of anions. These findings show that the incorporation of additional oxygen into TiAlN(O) and CrAlN materials is favored because of thermodynamic reasons. These processes have to go along with the formation of metal vacancies that lead to the stabilization of the atomic structure. Another possible explanation is the oxidation of Ti(III) to Ti(IV). Within the bulk phase of TiAlN only Ti(III) is present which leads to a metastable

material phase, that is oxidized up to Ti(IV) in the surface near region upon contact with oxygen at high partial pressures to reach the thermodynamic equilibrium.

As the exact mechanisms of these processes are hard to analyze and describe, additional quantum mechanical simulations are a very promising approach to take a deeper insight here. The here presented experimental and theoretical work on the initial chemisorption of oxygen on TiAlN was in a very good agreement. It could be shown that the reaction is driven by Ti–O bonds and not by Al–O bonding although the formation of Al_2O_3 would be thermodynamically favored over the formation of titanium oxide. Within these experiments at low oxygen partial pressures of 10^{-8} mbar the formation of Ti(III) oxide Ti_2O_3 has been observed where no further oxidation to Ti(IV) took place. Hence, it can be concluded that high partial pressures of oxygen and/or the presence of water are necessary to create a fully oxidized surface region.

For CrAlN the bulk properties were also investigated as a function of the HPPMS parameters. Here it could be shown that the hardness of the coatings can be increased by using short HPPMS pulse-on-times during the deposition process which also leads to a denser morphology and increased barrier properties. These results are mainly discussed based on a higher ionization rate within the plasma.

In summary the better understanding of the surface oxidation reaction of CrAlN and TiAlN(O) achieved in this work may lead to new approaches for tailored bulk- and surface compositions of these materials that are exactly concerted for certain applications such as polymer processing. The issue of uncontrolled surface oxidation could be overcome by an optimized deposition process that includes an adequate aftertreatment of the coatings, e.g. by a non-depositing plasma that only triggers a desired surface chemistry.

Comparable factors of influence have to be considered discussing the interactions at TiO_2 interfaces. Within this work the deployment of atmospherically prepared TiO_2 single crystalline surfaces as a model system for more complex titanium dioxide surfaces has to be highlighted. It could be shown that such a defined system is well suited to study interactions on a fundamental level. Also the presence of adsorbates on such TiO_2 surfaces is of high importance when discussing interactions like adhesion and surface wetting. The formation of a model adsorbate film consisting of nonadecanoic acid on TiO_2(100) was studied which showed a low interaction with the surface. Mainly physisorption takes place between carboxy-functional molecules and the OH-termiated surface.

Discussing the interaction at TiO_2 surfaces, the defect density of the surface and surface near region also plays an important role. Within this work the well-established

technique of AFM force-distance spectroscopy has been applied under UHV conditions. This setup allows to investigate adhesion phenomena at surfaces under very controlled conditions without environmental influences such as the presence of water or oxygen. It could be shown that the adhesion force is significantly influenced by the defect density of the TiO_2 surface. The bombardment of TiO_2(110) surfaces with Ar^+ ions of 200 eV energy led to the formation of Ti^{3+} defects in the surface near region of the crystal. It could be shown that the surface defect density could be decreased by dosing water at $3 \cdot 10^{-8}$ mbar and further by annealing the crystal at 473 K. The defect density was correlated to the contact force that was measured by means of AFM between the TiO_2(110) substrate and an TiO_2 covered AFM tip. As a defect free substrate, a TiO_2 crystal covered with octadecylphosphonic acid was used as a reference. For all four surface states the measured contact force was correlated to the surface defect density. It could be shown that a higher Ti^{3+} defect density leads to increased interaction forces that are discussed based on Ti $3d^1$ states that have two effects: (i) a higher donor density for the formation of additional bonds and (ii) a change in the electronic structure of the valence band which has an impact on the effective Hamaker constant.

Although these investigations were performed based on a model system under very controlled conditions, this approach might lead to an increased understanding of more complex TiO_2 surfaces. TiO_2 particles under environmental conditions exhibit a way more complicated surface structure in terms of crystallinity and morphology. Here also environmental influences such as water of adsorbates are present. Based on the results obtained within this work a transfer towards experiments that are performed under ambient conditions is possible. AFM force-distance measurements in the presence of water or other adsorbate forming molecules may give a deeper insight into the interaction of – not only of TiO_2 – particles which are present in technical applications under ambient conditions.

Chapter 5

5 List of Publications and conference presentations

5.1 Publications in peer-reviewed journals

1. C. Kunze, M. Valtiner, R. Michels, K. Huber, G. Grundmeier
Self-localization of polyacrylic acid molecules on polar ZnO(0001)-Zn surfaces
Physical Chemistry Chemical Physics, 13 (2011) 12959-12967.

2. C. Kunze, B. Torun, I. Giner, G. Grundmeier
Surface chemistry and nonadecanoic acid adsorbate layers on TiO_2(100) surfaces prepared at ambient conditions
Surface Science, 606 (2012) 1527-1533.

3. C. Gnoth, C. Kunze, M. Hans, M. to Baben, J. Emmerlich, J.M. Schneider, G. Grundmeier
Surface chemistry of TiAlN and TiAlNO coatings deposited by means of high power pulsed magnetron sputtering
Journal of Physics D-Applied Physics, 46 (2013) 084003.

4. N. Bagcivan, K. Bobzin, G. Grundmeier, M. Wiesing, Ö. Özcan, C. Kunze, R. H. Brugnara
Influence of HPPMS Pulse Length and Inert Gas mixture on the Properties of (Cr,Al)N Coatings
Thin Solid Films, 549 (2013), 192-198.

5. I. Giner, M. Maxisch, C. Kunze, G. Grundmeier
Combined in-situ PM-IRRAS/QCM studies of water adsorption on plasma modified aluminum oxide/aluminum substrates
Applied Surface Science, 283 (2013), 145-153.

6. C. Kunze, R. H. Brugnara, N. Bagcivan, K. Bobzin, G. Grundmeier
Surface Chemistry of PVD (Cr,Al)N coatings deposited by means of Direct Current and High Power Pulsed Magnetron Sputtering
Surface and Interface Analysis, 45 (2013), 1884-1892.

7. C. Kunze, D. Music, M. to Baben, J.M. Schneider, G. Grundmeier
Temporal evolution of oxygen chemisorption on TiAlN
Applied Surface Science, 290 (2013), 504-508.

8. C. Kunze, I. Giner, B. Torun, G. Grundmeier
Influence of the surface chemistry on TiO_2 - TiO_2 nanocontact forces as measured by an UHV-AFM
Chemical Physics Letters, 597 (2014), 134-138.

9. B. Torun, C. Kunze, C. Zhang, T.D. Kühne, G. Grundmeier
Study of water adsorption and capillary bridge formation for SiO_2 nanoparticle layers by means of a combined in-situ FT-IR reflection spectroscopy – QCM-D set-up
Physical Chemistry Chemical Physics, 16 (2014), 7377-7384.

5.2 Selected conference contributions

5.2.1 Scientific talks

WCARP 2010, Arcachon, France
C. Kunze, M. Valtiner, G. Grundmeier:
Adhesion and Self-Location of Polyacrylic Acid Molecules on Stepped Surfaces of ZnO(0001)-Zn Single Crystals

Bunsentagung 2011, Berlin, Germany
C. Kunze, M. Valtiner, G. Grundmeier:
Adhesion and self-location of polyacrylic acid molecules on stepped surfaces of ZnO(0001)-Zn single crystals

ICMCTF 2012, San Diego, USA
C. Kunze, C. Gnoth, M. to Baben, S. Theiß, N. Bagcivan, K. Bobzin, J. M. Schneider, G. Grundmeier:
Surface Analysis of TiAlON and CrAlN Coatings Deposited by Means of HPPMS

AVS 2012, Tampa, USA
C. Kunze, B. Torun, G. Grundmeier:
Characterization of surface and adsorbate chemistry on TiO_2 particle ensembles and atmospherically prepared TiO_2 single crystalline surfaces

AVS 2013, Long Beach, USA
C. Kunze, S. Waschke, M. to Baben, D. Music, J. M. Schneider, G. Grundmeier:
Surface Chemistry and Interaction with Polymers of TiAlNO Protective Coatings Deposited by HPPMS

5.2.2 Poster presentations

Zsigmondy Kolloquium 2011, Münster, Germany
C. Kunze, M. Valtiner, G. Grundmeier:
Molecular Adhesion and Self-Location of Polyacrylic Acid Molecules on Stepped Surfaces of ZnO(0001)-Zn Single Crystals

CHoPS 2012, Friedrichshafen, Germany
C. Kunze, B. Torun, G. Grundmeier:
Characterization of surface and adsorbate chemistry on TiO_2(100) and TiO_2(110) surfaces prepared under ambient conditions

6 List of abbreviations and acronyms

A	ampere
AES	auger electron spectroscopy
AFM	atomic force microscopy
APS	appearance potential spectroscopy
AR-XPS	angle resolved XPS
DC-MS	direct current magnetron sputtering
DFT	density functional theory
EDX	energy dispersive X-ray spectroscopy
ELS	electron loss spectroscopy
eV	electron volt
GDOES	glow discharge optical emission spectroscopy
HPPMS	high power pulsed magnetron sputtering
K	Kelvin
kW	kilowatt
L	Langmuir
LEED	low energy electron diffraction
LTO	low temperature oxidation
MD	molecular dynamics
ML	monolayer
µm	micrometer
NDCA	nonadecanoic acid
nm	nanometer
nN	Nanonewton
ODPA	octadecylphosphonic acid
Pa	Pascal
pN	Piconewton
PVD	physical vapor deposition
SAM	self assembled monolayer
sccm	standard cubic centimeter
SPM	scanning probe microscopy
STM	scanning tunneling microscopy
TPD	temperature-programmed desorption
UPS	UV photoelectron spectroscopy
UHV	ulta high vacuum
V	volt
XPS	X-ray photoelectron spectroscopy
XRD	X-rax diffraction

7 Bibliography

[1] G. Ertl, H. Knozinger, F. Schuth, J. Weitkamp: Handbook of heterogeneous catalysis, *METODOLOGÍA DOCENTE*.

[2] G. Grundmeier, W. Schmidt, M. Stratmann: Corrosion protection by organic coatings: electrochemical mechanism and novel methods of investigation, *Electrochim. Acta* (2000), *45*, 2515.

[3] L. Carrette, K. Friedrich, U. Stimming: Fuel cells–fundamentals and applications, *Fuel cells* (2001), *1*, 5.

[4] A. J. Kinloch, *Adhesion and adhesives: science and technology*, Springer, 1987.

[5] Y. Nishi, R. Doering, *Handbook of semiconductor manufacturing technology*, CRC Press, 2000.

[6] R. A. Freitas, *Nanomedicine, volume I: basic capabilities*, Landes Bioscience Georgetown, TX, 1999.

[7] C. Mee, E. Daniel, *Magnetic storage handbook*, McGraw-Hill, Inc., 1996.

[8] W. D. Münz: Titanium aluminum nitride films: A new alternative to TiN coatings, *Journal of Vacuum Science & Technology A* (1986), *4*, 2717.

[9] D. McIntyre, J. E. Greene, G. Håkansson, J. E. Sundgren, W. D. Münz: Oxidation of metastable single-phase polycrystalline Ti0.5Al0.5N films: Kinetics and mechanisms, *J. Appl. Phys.* (1990), *67*, 1542.

[10] D. Music, D. Lange, L. Raumann, M. t. Baben, F. von Fragstein, J. M. Schneider: Polypropylene–MAlN (M = Ti, Cr) interface interactions, *Surf. Sci.* (2012), *606*, 986.

[11] K. Kawata, H. Sugimura, O. Takai: Characterization of multilayer films of Ti,Al,O,C,N system prepared by pulsed d.c. plasma-enhanced chemical vapor deposition, *Thin Solid Films* (2001), *390*, 64.

[12] K. Bobzin, R. Nickel, N. Bagcivan, F. D. Manz: PVD—Coatings in Injection Molding Machines for Processing Optical Polymers, *Plasma Processes and Polymers* (2007), *4*, S144.

[13] W. Michaeli, K. Bobzin, S. Hessner, A. Neuss, F. Manz: PVD-coated Plastication Screws, *Kunststoffe* (2006), *8*, 66.

[14] I. Petrov, P. B. Barna, L. Hultman, J. E. Greene: Microstructural evolution during film growth, *Journal of Vacuum Science & Technology A* (2003), *21*, S117.

[15] K. Sarakinos, J. Alami, S. Konstantinidis: High power pulsed magnetron sputtering: A review on scientific and engineering state of the art, *Surf. Coat. Technol.* (2010), *204*, 1661.

[16] D. Lundin, K. Sarakinos: An introduction to thin film processing using high-power impulse magnetron sputtering, *J. Mater. Res.* (2012), *27*, 780.

[17] J. Alami, P. O. Å. Persson, D. Music, J. T. Gudmundsson, J. Bohlmark, U. Helmersson: Ion-assisted physical vapor deposition for enhanced film properties on nonflat surfaces, *Journal of Vacuum Science & Technology A* (2005), *23*, 278.

[18] A. P. Ehiasarian, R. New, W. D. Münz, L. Hultman, U. Helmersson, V. Kouznetsov: Influence of high power densities on the composition of pulsed magnetron plasmas, *Vacuum* (2002), *65*, 147.

[19] A. P. Ehiasarian, W. D. Münz, L. Hultman, U. Helmersson, I. Petrov: High power pulsed magnetron sputtered CrNx films, *Surf. Coat. Technol.* (2003), *163-164*, 267.

[20] N. Bagcivan, K. Bobzin, S. Theiss: (Cr1-xAlx)N: A comparison of direct current, middle frequency pulsed and high power pulsed magnetron sputtering for injection molding components, *Thin Solid Films* (2013), *528*, 180.

[21] N. Bagcivan, K. Bobzin, S. Theiss: Comparison of (Cr0.75Al0.25)N Coatings Deposited by Conventional and High Power Pulsed Magnetron Sputtering, *Contributions to Plasma Physics* (2012), *52*, 601.

[22] N. Bagcivan, K. Bobzin, G. Grundmeier, M. Wiesing, O. Ozcan, C. Kunze, R. H. Brugnara: Influence of HPPMS pulse length and inert gas mixture on the properties of (Cr,Al)N coatings, *Thin Solid Films* (2013), *549*, 192.

[23] C. Gnoth, C. Kunze, M. Hans, M. T. Baben, J. Emmerlich, J. M. Schneider, G. Grundmeier: Surface chemistry of TiAlN and TiAlNO coatings deposited by means of high power pulsed magnetron sputtering, *Journal of Physics D-Applied Physics* (2013), *46*.

[24] C. Kunze, R. H. Brugnara, N. Bagcivan, K. Bobzin, G. Grundmeier: Surface chemistry of PVD (Cr,Al)N coatings deposited by means of direct current and high power pulsed magnetron sputtering, *Surf. Interface Anal.* (2013), *45*, 1884.

[25] A. L. Linsebigler, G. Q. Lu, J. T. Yates: PHOTOCATALYSIS ON TIO2 SURFACES - PRINCIPLES, MECHANISMS, AND SELECTED RESULTS, *Chem. Rev.* (1995), *95*, 735.

[26] K. C. Popat, L. Leoni, C. A. Grimes, T. A. Desai: Influence of engineered titania nanotubular surfaces on bone cells, *Biomaterials* (2007), *28*, 3188.

[27] B. Oregan, M. Gratzel: A LOW-COST, HIGH-EFFICIENCY SOLAR-CELL BASED ON DYE-SENSITIZED COLLOIDAL TIO2 FILMS, *Nature* (1991), *353*, 737.

[28] J. H. Braun: Titanium dioxide - A review, *Journal of Coatings Technology* (1997), *69*, 59.

[29] A. Weir, P. Westerhoff, L. Fabricius, K. Hristovski, N. von Goetz: Titanium Dioxide Nanoparticles in Food and Personal Care Products, *Environmental Science & Technology* (2012), *46*, 2242.

[30] U. Diebold: The surface science of titanium dioxide, *Surf. Sci. Rep.* (2003), *48*, 53.

[31] T. Radhakrishnan: The optical properties of titanium dioxide, *Proceedings of the Indian Academy of Sciences - Section A* (1952), *35*, 117.

[32] M. Gratzel, F. P. Rotzinger: THE INFLUENCE OF THE CRYSTAL-LATTICE STRUCTURE ON THE CONDUCTION-BAND ENERGY OF OXIDES OF TITANIUM(IV), *Chem. Phys. Lett.* (1985), *118*, 474.

[33] U. Diebold, J. Lehman, T. Mahmoud, M. Kuhn, G. Leonardelli, W. Hebenstreit, M. Schmid, P. Varga: Intrinsic defects on a TiO2(110)(1 × 1) surface and their reaction with oxygen: A scanning tunneling microscopy study, *Surf. Sci.* (1998), *411*, 137.

[34] M. A. Henderson: Structural sensitivity in the dissociation of water on TiO2 single-crystal surfaces, *Langmuir* (1996), *12*, 5093.

[35] R. A. Bennett, P. Stone, N. J. Price, M. Bowker: Two Reconstructions of TiO2(110): Surface Rearrangement and Reactivity Studied Using Elevated Temperature Scanning Tunneling Microscopy, *Phys. Rev. Lett.* (1999), *82*, 3831.

[36] A. Linsebigler, G. Lu, J. T. Yates Jr: CO chemisorption on TiO2(110): Oxygen vacancy site influence on CO adsorption, *The Journal of Chemical Physics* (1995), *103*, 9438.

[37] M. A. Henderson: The influence of oxide surface structure on adsorbate chemistry: desorption of water from the smooth, the microfaceted and the ion sputtered surfaces of TiO2(100), *Surf. Sci.* (1994), *319*, 315.

[38] C. Zhang, P. J. D. Lindan: Multilayer water adsorption on rutile TiO2(110): A first-principles study, *J. Chem. Phys.* (2003), *118*, 4620.

[39] E. M. J. Johansson, S. Plogmaker, L. E. Walle, R. Schölin, A. Borg, A. Sandell, H. Rensmo: Comparing surface binding of the maleic anhydride anchor group on single crystalline anatase Tio 2 (101), (100), and (001) surfaces, *Journal of Physical Chemistry C* (2010), *114*, 15015.

[40] R. Tero, T. Ujihara, T. Urisu: Lipid bilayer membrane with atomic step structure: Supported bilayer on a step-and-terrace TiO2(100) surface, *Langmuir* (2008), *24*, 11567.

[41] J. B. Sambur, C. M. Averill, C. Bradley, J. Schuttlefield, S. H. Lee, J. R. Reynolds, K. S. Schanze, B. A. Parkinson: Interfacial morphology and photoelectrochemistry of conjugated polyelectrolytes adsorbed on single crystal TiO 2, *Langmuir* (2011), *27*, 11906.

[42] R. Nakamura, N. Ohashi, A. Imanishi, T. Osawa, Y. Matsumoto, H. Koinuma, Y. Nakato: Crystal-face dependences of surface band edges and hole reactivity, revealed by

preparation of essentially atomically smooth and stable (110) and (100) n-TiO2 (rutile) surfaces, *Journal of Physical Chemistry B* (2005), *109*, 1648.

[43] Y. Yamamoto, K. Nakajima, T. Ohsawa, Y. Matsumoto, H. Konuma: Preparation of atomically smooth TiO_2 single crystal surfaces and their photochemical property, *Japanese Journal of Applied Physics Part 2-Letters & Express Letters* (2005), *44*, L511.

[44] A. Imanishi, T. Okamura, N. Ohashi, R. Nakamura, Y. Nakato: Mechanism of water photooxidation reaction at atomically flat TiO_2 (rutile) (110) and (100) surfaces: Dependence on solution pH, *Journal of the American Chemical Society* (2007), *129*, 11569.

[45] C. Kunze, B. Torun, I. Giner, G. Grundmeier: Surface chemistry and nonadecanoic acid adsorbate layers on TiO2(100) surfaces prepared at ambient conditions, *Surf. Sci.* (2012), *606*, 1527.

[46] S. Salameh, J. Schneider, J. Laube, A. Alessandrini, P. Facci, J. W. Seo, L. C. Ciacchi, L. Mädler: Adhesion Mechanisms of the Contact Interface of TiO2 Nanoparticles in Films and Aggregates, *Langmuir* (2012), *28*, 11457.

[47] H. Weller: QUANTIZED SEMICONDUCTOR PARTICLES - A NOVEL STATE OF MATTER FOR MATERIALS SCIENCE, *Advanced Materials* (1993), *5*, 88.

[48] N. G. Park, J. van de Lagemaat, A. J. Frank: Comparison of dye-sensitized rutile- and anatase-based TiO2 solar cells, *Journal of Physical Chemistry B* (2000), *104*, 8989.

[49] P. A. Kralchevsky, K. Nagayama: CAPILLARY FORCES BETWEEN COLLOIDAL PARTICLES, *Langmuir* (1994), *10*, 23.

[50] X. D. Xiao, L. M. Qian: Investigation of humidity-dependent capillary force, *Langmuir* (2000), *16*, 8153.

[51] M. Farshchi-Tabrizi, M. Kappl, Y. J. Cheng, J. Gutmann, H. J. Butt: On the adhesion between fine particles and nanocontacts: An atomic force microscope study, *Langmuir* (2006), *22*, 2171.

[52] R. Wang, N. Sakai, A. Fujishima, T. Watanabe, K. Hashimoto: Studies of surface wettability conversion on TiO_2 single-crystal surfaces, *Journal of Physical Chemistry B* (1999), *103*, 2188.

[53] R. Tadepalli, C. V. Thompson: Formation of Cu-Cu interfaces with ideal adhesive strengths via room temperature pressure bonding in ultrahigh vacuum, *Applied Physics Letters* (2007), *90*.

[54] K. Meine, K. Kloß, T. Schneider, D. Spaltmann: The influence of surface roughness on the adhesion force, *Surf. Interface Anal.* (2004), *36*, 694.

[55] J. N. Israelachvili, *Intermolecular and Surface Forces*, Elsevier Science, 2010.

[56] S. Chretien, H. Metiu: Electronic Structure of Partially Reduced Rutile TiO2(110) Surface: Where Are the Unpaired Electrons Located?, *Journal of Physical Chemistry C* (2011), *115*, 4696.

[57] J. Mahanty, B. W. Ninham, *Dispersion forces*, Academic Press, 1976.

[58] P. Thissen, M. Valtiner, G. Grundmeier: Stability of Phosphonic Acid Self-Assembled Monolayers on Amorphous and Single-Crystalline Aluminum Oxide Surfaces in Aqueous Solution, *Langmuir* (2010), *26*, 156.

[59] S.-Y. Liu, F.-H. Wang, Y.-S. Zhou, J.-X. Shang: Ab initio study of oxygen adsorption on the Ti(0001) surface, *J. Phys.: Condens. Matter* (2007), *19*, 226004.

[60] J. L. Gland: Molecular and atomic adsorption of oxygen on the Pt(111) and Pt(S)-12(111) × (111) surfaces, *Surf. Sci.* (1980), *93*, 487.

[61] H. Steininger, S. Lehwald, H. Ibach: Adsorption of oxygen on Pt(111), *Surf. Sci.* (1982), *123*, 1.

[62] R. B. Getman, W. F. Schneider, A. D. Smeltz, W. N. Delgass, F. H. Ribeiro: Oxygen-Coverage Effects on Molecular Dissociations at a Pt Metal Surface, *Phys. Rev. Lett.* (2009), *102*.

[63] B. T. Jonker, J. F. Morar, R. L. Park: Surface states and oxygen chemisorption on Ti(0001), *Physical Review B* (1981), *24*, 2951.

[64] N. D. Shinn, T. E. Madey: Oxygen chemisorption on Cr(110): I. Dissociative adsorption, *Surf. Sci.* (1986), *173*, 379.
[65] Y. Sakisaka, H. Kato, M. Onchi: Oxygen chemisorption and initial oxidation of Cr(110), *Surf. Sci.* (1982), *120*, 150.
[66] J. S. Foord, R. M. Lambert: Oxygen chemisorption and corrosion on Cr(100) and Cr(110) single crystal surfaces, *Surf. Sci.* (1985), *161*, 513.
[67] P. O. Gartland: Adsorption of oxygen on clean single crystal faces of aluminium, *Surf. Sci.* (1977), *62*, 183.
[68] H. Brune, J. Wintterlin, R. J. Behm, G. Ertl: Surface migration of ''hot'' adatoms in the course of dissociative chemisorption of oxygen on Al(111), *Phys. Rev. Lett.* (1992), *68*, 624.
[69] S. A. Flodström, C. W. B. Martinsson, R. Z. Bachrach, S. B. M. Hagström, R. S. Bauer: Ordered Oxygen Overlayer Associated with Chemisorption State on Al(111), *Phys. Rev. Lett.* (1978), *40*, 907.
[70] N. Cabrera, N. F. Mott: Theory of the oxidation of metals, *Rep. Prog. Phys.* (1949), *12*, 163.
[71] A. Atkinson: Transport processes during the growth of oxide films at elevated temperature, *Reviews of Modern Physics* (1985), *57*, 437.
[72] F. P. Fehlner, N. F. Mott: Low-temperature oxidation, *Oxid. Met.* (1970), *2*, 59.
[73] D. D. Eley, P. R. Wilkinson: Adsorption and Oxide Formation on Aluminium Films, *Proceedings of the Royal Society of London. Series A. Mathematical and Physical Sciences* (1960), *254*, 327.
[74] C. Kunze, D. Music, M. T. Baben, J. M. Schneider, G. Grundmeier: Temporal evolution of oxygen chemisorption on TiAlN, *Appl. Surf. Sci.* (2014), *290*, 504.
[75] K. P. Shaha, H. Ruess, S. Rotert, M. T. Baben, D. Music, J. M. Schneider: Nonmetal sublattice population induced defect structure in transition metal aluminum oxynitrides, *Appl. Phys. Lett.* (2013), *103*.
[76] D. Music, J. M. Schneider: Ab initio study of Ti0.5Al0.5N(001)-residual and environmental gas interactions, *New Journal of Physics* (2013), *15*.
[77] J. Zimmermann, M. W. Finnis, L. C. Ciacchi: Vacancy segregation in the initial oxidation stages of the TiN(100) surface, *The Journal of Chemical Physics* (2009), *130*.
[78] S. Piscanec, L. Colombi Ciacchi, E. Vesselli, G. Comelli, O. Sbaizero, S. Meriani, A. De Vita: Bioactivity of TiN-coated titanium implants, *Acta Mater.* (2004), *52*, 1237.
[79] A. Tempez, A. Bensaoula, A. Schultz: Characterization of TiAlN thin film annealed under O2 by in situ time of flight direct recoil spectroscopy/mass spectroscopy of recoiled ions and ex situ x-ray photoelectron spectroscopy, *Journal of Vacuum Science & Technology A* (2002), *20*, 1320.
[80] J. F. Watts, J. Wolstenholme, *An Introduction to Surface Analysis by XPS and AES*, Wiley, 2003.
[81] M. P. Seah, W. A. Dench: Quantitative electron spectroscopy of surfaces: A standard data base for electron inelastic mean free paths in solids, *Surface and Interface Analysis* (1979), *1*, 2.
[82] D. Briggs, P. Seah, *Practical Surface Analysis: Auger and X-ray photoelectron spectroscopy*, Wiley, 1990.
[83] G. Binning, H. Rohrer, C. Gerber, E. Weibel, in *Scanning Tunneling Microscopy*, Springer, 1993, pp. 31.
[84] G. Binnig, C. F. Quate, C. Gerber: Atomic force microscope, *Phys. Rev. Lett.* (1986), *56*, 930.
[85] H. J. Butt, B. Cappella, M. Kappl: Force measurements with the atomic force microscope: Technique, interpretation and applications, *Surf. Sci. Rep.* (2005), *59*, 1.
[86] R. García, R. Pérez: Dynamic atomic force microscopy methods, *Surf. Sci. Rep.* (2002), *47*, 197.
[87] *Biological applications of atomic force microscopy, Vol. 266*, 1994.

[88] L. Zitzler, S. Herminghaus, F. Mugele: Capillary forces in tapping mode atomic force microscopy, *Physical Review B* (2002), *66*, 155436.

[89] L. Gross, F. Mohn, N. Moll, P. Liljeroth, G. Meyer: The Chemical Structure of a Molecule Resolved by Atomic Force Microscopy, *Science* (2009), *325*, 1110.

[90] F. J. Giessibl, S. Hembacher, H. Bielefeldt, J. Mannhart: Subatomic Features on the Silicon (111)-(7×7) Surface Observed by Atomic Force Microscopy, *Science* (2000), *289*, 422.

[91] Y. Sugimoto, P. Pou, M. Abe, P. Jelinek, R. Perez, S. Morita, O. Custance: Chemical identification of individual surface atoms by atomic force microscopy, *Nature* (2007), *446*, 64.

[92] B. Cappella, G. Dietler: Force-distance curves by atomic force microscopy, *Surf. Sci. Rep.* (1999), *34*, 1.

[93] T. Hugel, M. Seitz: The study of molecular interactions by AFM force spectroscopy, *Macromol. Rapid Commun.* (2001), *22*, 989.

[94] B. Ozkaya, S. Grosse-Kreul, C. Corbella, A. von Keudell, G. Grundmeier: Combined In Situ XPS and UHV-Chemical Force Microscopy (CFM) Studies of the Plasma Induced Surface Oxidation of Polypropylene, *Plasma Processes and Polymers* (2014), *11*, 256.

[95] J. E. Jones: On the Determination of Molecular Fields. II. From the Equation of State of a Gas, *Proceedings of the Royal Society of London. Series A* (1924), *106*, 463.

[96] J. L. Hutter, J. Bechhoefer: CALIBRATION OF ATOMIC-FORCE MICROSCOPE TIPS, *Rev. Sci. Instrum.* (1993), *64*, 1868.

[97] C. Kunze, I. Giner, B. Torun, G. Grundmeier: Influence of the surface chemistry on TiO2 – TiO2 nanocontact forces as measured by an UHV–AFM, *Chem. Phys. Lett.* (2014), *597*, 134.